DISSERTATIONES
CHIMICAE
UNIVERSITATIS
TARTUENSIS
243

FREDDY KUKK

Electrochemical Characterization of Structurally and Chemically Modified Solid Oxide Cells Operated in Electrolysis Mode

DISSERTATIONES CHIMICAE UNIVERSITATIS TARTUENSIS

243

DISSERTATIONES CHIMICAE UNIVERSITATIS TARTUENSIS

243

FREDDY KUKK

Electrochemical Characterization of Structurally and Chemically Modified Solid Oxide Cells Operated in Electrolysis Mode

UNIVERSITY OF TARTU
Press
1632

Institute of Chemistry, Faculty of Science and Technology, University of Tartu, Estonia

Dissertation has been accepted for the commencement of the degree of *Doctor philosophiae* in Chemistry on April 8, 2026, by the Council of Institute of Chemistry, Faculty of Science and Technology, University of Tartu.

Supervisors: Professor Gunnar Nurk, Ph.D.
Institute of Chemistry, University of Tartu, Estonia

Professor Enn Lust, Ph.D.
Institute of Chemistry, University of Tartu, Estonia

Sergii Pylypko, Ph.D.
Elcogen AS

Martin Skov Skjøth-Rasmussen, Ph.D.
Elcogen AS

Opponent: Professor Anke Hagen, Ph.D.
Technical University of Denmark, Denmark

Commencement: May 21, 2026 at 14:15 Ravila 14A-1020,
Tartu (Chemicum) and Microsoft Teams (*online*)

This work was supported by Estonian Research Council grants PRG551, PUT1581, IUT20-13 and TEM-TA81, by Estonian Ministry of Education and Research (TK210), by the project "Increasing the knowledge intensity of Ida-Viru entrepreneurship" (ÕÜF2) co-founded by the European Union, by the EU through the European Regional Development Fund Project TK141 "Advanced materials and high-technology devices for energy recuperation systems", by the European Union's Horizon 2020 research and innovation program under grant agreement No. 862482 (ARENHA project).

ISSN 1406-0299 (print) ISSN 2806-2159 (pdf)
ISBN 978-9908-57-191-1 (print) ISBN 978-9908-57-192-8 (pdf)

University of Tartu Press
www.tyk.ee

TABLE OF CONTENTS

1. LIST OF ORIGINAL PUBLICATIONS

I. F. Kukk, P. Möller, R. Kanarbik, G. Nurk, Study of Long-Term Stability of Ni-$Zr_{0.92}Y_{0.08}O_{2-\delta}$ | $Zr_{0.92}Y_{0.08}O_{2-\delta}$ | $Ce_{0.9}Gd_{0.1}O_{2-\delta}$ | $Pr_{0.6}Sr_{0.4}CoO_{3-\delta}$ at SOFC and SOEC Mode. Energies, 14 (2021) 824. DOI: 10.3390/en14040824

II. F. Kukk, S. Pylypko, E. Lust, G. Nurk, Influence of Active Layer Thickness of Reversible Solid Oxide Cells on the Electrochemical Performance of Water Electrolysis. ECS Trans. 103 (2021) 511. DOI: 10.1149/10301.0511ecst

III. F. Kukk, S. Pylypko, E. Lust, G. Nurk, Influence of Hydrogen Electrode Active Layer Thickness on Electrochemical Performance of Solid Oxide Cell Operating in Electrolysis Mode. J. Electrochem. Soc. 170 (2023) 094501. DOI: 10.1149/1945-7111/acf20b

IV. F. Kukk, S. Pylypko, M. S. Skjøth-Rasmussen, E. Lust, G. Nurk, Influence of Chemical Modifications with Fe, Co, and GDC on the Electrochemical Performance of the Ni-8YSZ Hydrogen Electrode in Solid Oxide Electrolysis Cells. J. Electrochem. Soc. **172** (2025) 110515. DOI: 10.1149/1945-7111/ae1417.

Author's contribution:

Paper I: Performed sample assembly and electrochemical characterization, SEM characterization, sample preparation for ToF-SIMS characterization, and analysis of all data.

Paper II: Performed the synthesis of single cells in the industrial setting, some physical and all electrochemical characterization of single cells, and analysis of data. Mainly responsible for the preparation of the manuscript.

Paper III: Performed the synthesis of single cells in the industrial setting, some physical and all electrochemical characterization of single cells, and analysis of data. Mainly responsible for the preparation of the manuscript.

Paper IV: Performed the synthesis of single cells in the industrial setting, some physical and all electrochemical characterization of single cells, and analysis of data. Mainly responsible for the preparation of the manuscript.

2. ABBREVIATIONS AND SYMBOLS

SOC	solid oxide cell
SoA	state of the art
V	cell voltage
V_0	voltage amplitude
I	current
I_0	current amplitude
j	current density
j_0	exchange current density
j_L	diffusion limited current density
$E_{tn,water}$	thermoneutral voltage for water electrolysis
$E_{tn,steam}$	thermoneutral voltage for water vapor electrolysis
OCV	open circuit voltage
T	absolute temperature
ΔH_f	enthalpy change of formation
ΔS_f	entropy change of formation
ΔH_{evap}	enthalpy change of evaporation
ΔG_f	Gibbs energy change of formation
ΔG_r^0	standard Gibbs energy change of reaction
ΔG_r	Gibbs energy change of reaction
R	universal gas constant
K	equilibrium constant
Q	reaction quotient
p^0	Standard pressure
p	partial pressure
$p_{H_2O,eq}$	partial pressure of water at equilibrium conditions
$p_{H_2,eq}$	partial pressure of hydrogen at equilibrium conditions
$p_{O_2,eq}$	partial pressure of oxygen at equilibrium conditions
p_{H_2O}	partial pressure of water
p_{H_2}	partial pressure of hydrogen
p_{O_2}	partial pressure of oxygen
z	number of electrons in a reaction
F	Faraday constant
E	potential
E^0	standard potential
σ	conductivity
σ_0	pre-factor for uncorrelated hopping of an ion
k_B	Boltzmann constant
E_a	activation energy
$E_{a\ tot}$	total activation energy
η	overpotential
η_{tot}	total overpotential

η_{act}	activation overpotential
η_{ohm}	ohmic overpotential
η_{conc}	concentration overpotential
α	symmetry factor
f	constant equal to $F/\mathrm{R}T$
D	diffusion coefficient
δ	thickness of diffusion layer
ω	angular frequency
t	time
φ	phase difference
Z	complex impedance
Z'	real part of impedance
Z''	imaginary part of impedance
CPE	constant phase element
$\mathrm{CPE}_{\mathrm{high}}$	high-frequency constant phase element
$\mathrm{CPE}_{\mathrm{mid}}$	mid-frequency constant phase element
$\mathrm{CPE}_{\mathrm{low}}$	low-frequency constant phase element
$\mathrm{P}_{\mathrm{high}}$	high-frequency process
$\mathrm{P}_{\mathrm{mid}}$	mid-frequency process
$\mathrm{P}_{\mathrm{mid\_1}}$	mid-frequency process 1
$\mathrm{P}_{\mathrm{mid\_2}}$	mid-frequency process 2
$\mathrm{P}_{\mathrm{low}}$	low-frequency process
T_{CPE}	CPE coefficient
ϕ	CPE exponent
C	capacitance
L	inductance
R	resistance
R_s	series resistance
R_p	polarization resistance
R_{high}	high-frequency polarization resistance
R_{mid}	mid-frequency polarization resistance
R_{low}	low-frequency polarization resistance
Z_C''	impedance of a capacitor
Z_L''	impedance of an inductor
$\omega_{Z_{max}''}$	characteristic angular frequency
τ	time constant
(RC)	circuit element consisting of a resistor and capacitor connected in parallel
ToF-SIMS	time-of-flight secondary ion mass spectrometer
ESA	electrostatic sector analyzer
HR-SEM	high resolution scanning electron microscope
LSC	$La_xSr_{1-x}CoO_{3-\delta}$
GDC	$Ce_xGd_{1-x}O_{2-\delta}$
8YSZ	$Zr_{0.92}Y_{0.08}O_{2-\delta}$

3YSZ	$Zr_{0.97}Y_{0.03}O_{2-\delta}$
YSZ	$Zr_xY_{1-x}O_{2-\delta}$
Ni-YSZ	cermet of Ni and $Zr_xY_{1-x}O_{2-\delta}$
Ni-8YSZ	cermet of Ni and $Zr_{0.92}Y_{0.08}O_{2-\delta}$
Ni-3YSZ	cermet of Ni and $Zr_{0.97}Y_{0.03}O_{2-\delta}$
Ni-GDC	cermet of Ni and $Ce_xGd_{1-x}O_{2-\delta}$
Ni-ScSZ	cermet of Ni and $Zr_xSc_{1-x}O_{2-\delta}$
LSCF	$La_xSr_{1-x}Co_yFe_{1-y}O_{3-\delta}$
LSM	$La_xSr_{1-x}MnO_{3-\delta}$
PSC	$Pr_xSr_{1-x}CoO_{3-\delta}$
TPB	three phase boundary
HEAL	hydrogen electrode active layer
CNLS	complex non-linear least squares analysis method
FCM	Fuel Cell Materials

3. INTRODUCTION

Hydrogen and the development of a green hydrogen economy are foreseen to play a central role in decreasing global CO_2 emissions and decreasing our reliance on fossil fuels [1]. Part of this role is seen to be a promising path to decarbonizing a significant part of the chemicals industry by substituting captive use of hydrogen derived from fossil fuels. Ammonia production accounted for 2% of total global energy consumption and 1.3% of global CO_2 emissions, owing to the need for ammonia-based fertilizers. Production of iron and steel, which uses coal for iron ore reduction processes, has been found to produce 8% of global CO_2 emissions [2,3]. Green hydrogen presents a potential emission-free alternative to the methane-derived hydrogen in ammonia production [4] and as a reducing agent for iron and steel production [5].

The solid oxide cell (SOC) technology is a promising tool to both use and produce hydrogen in the energy and chemicals sectors. In principle, SOC technology is highly efficient, theoretically able to convert hydrogen technology or hydrocarbons into electrical energy at >70% efficiency in fuel cell mode [6] and able to electrolyze water at >94% electrical efficiency at stack level (calculated based on the lower heating value) [7]. The high operating temperature of the SOC decreases the internal resistance of the cell and results in lower electrical losses. Moreover, the materials used in the SOC are less costly than the materials used in alternative technologies when compared to electrolysis systems. The ability to both generate and utilize hydrogen as a chemical energy carrier, i.e., to store and regenerate energy in a single system, can also be used to increase the efficiency of large-scale industrial production facilities [8,9].

The state-of-the-art (SoA) reversible SOC architecture is based upon the SoA solid oxide fuel cell (SOFC) configuration. Studies handling long-term operation in electrolysis mode have found different degradation processes than those found in long term fuel cell operation conditions [10,11]. This suggests that the SoA SOC can be improved to increase performance and durability in electrolysis mode as well as in reversible mode. Studies investigating the performance of the SOC find that the electrochemical processes at the hydrogen electrode have the greatest impact [12,13,14]. Thus, the hydrogen electrode active layer (HEAL) is a major contributor to the performance of the SOC [15]. The optimization and modification of the SoA SOC for electrolysis operation should therefore be started with the HEAL, which has the potential for the highest impact on performance and durability.

The aim of this work was to improve the electrolysis performance of a SOC device prepared in an industrial setting. As a first step, the SOCs were characterized over long-term degradation tests in fuel cell and electrolysis operation modes. After analysis of long-term tests the contribution of the hydrogen electrode active layer (HEAL) on the electrolysis performance of the SOC was investigated in short-term electrochemical experiments. In the second stage, SOC with HEAL thicknesses of 0–20 µm were manufactured and characterized. Further investigations were carried out in the third stage with chemical modifications to the HEAL, where either Co, Fe or gadolinia doped ceria (GDC) was introduced during the hydrogen electrode manufacturing step. Changes to the industrial manufacturing process and to the overall cell microstructure were kept to a minimum. SOC electrochemical performance analysis was carried out using the cyclic voltammetry (CV) and electrochemical impedance spectroscopy (EIS) methods. Detailed analysis of the effects of the modifications was conducted by fitting the experimental EIS spectra with theoretical equivalent circuit models. Systematic mapping of impedance component values obtained using the non-linear least squares (CNLS) fitting method enabled to associate limiting processes in the SOC impedance spectra with some physical (limiting) processes occurring in the electrode. By changing SOC operating conditions affecting the HEAL (H_2/H_2O ratio, temperature), these current limiting processes could be used to characterize the HEAL and highlight the differences that the modifications induced.

4. LITERATURE OVERVIEW

4.1 Solid Oxide Cell Technology

The solid oxide cell is a high temperature electrochemical device, usually operated at temperatures between 600 and 850 °C. This technology can be used as a fuel cell to convert the chemical energy of fuel gas directly into electrical energy without combustion or as an electrolysis cell, to split steam or CO_2 into either H_2 and O_2 or CO and O_2, respectively.

Due to the high operating temperature and direct energy conversion, SOC technology is one of the most efficient electrochemical methods in use [16].

4.1.1 Thermodynamics of a Solid Oxide Cell

The working principle of the solid oxide cell is usually conveyed via its simplest feed gases – hydrogen and oxygen (including air). During fuel cell operation, oxygen is reduced at the oxygen electrode according to equation (2.1) while hydrogen is oxidized at the hydrogen electrode according to equation (2.2). The total reaction in the SOC can thus be presented as equation (2.3).

$$\mathrm{O_2 + 4e^- \leftrightarrow 2O^{2-}} \tag{2.1}$$

$$\mathrm{H_2 + O^{2-} \leftrightarrow H_2O + 2e^-} \tag{2.2}$$

$$\mathrm{H_2 + \frac{1}{2}O_2 \leftrightarrow H_2O} \tag{2.3}$$

The maximum work that can be used in a SOC device can be calculated using the reaction Gibbs energy. The standard reaction Gibbs energy at reaction equilibrium is presented as an equation (2.4), where R is the universal gas constant, T is absolute temperature, and K is the equilibrium constant. As in practice, the SOC is operated at ambient pressure, the standard pressure p^0 = 1 bar and thus K can be expressed with the equation (2.5). Thus, the reaction Gibbs energy is expressed with the equation (2.6), where Q is the reaction quotient, which is the ratio of the activities of the products to the activities of the reactants. As the SOC uses gases during operation, the activities are approximated by partial pressures of the gases, similar to the calculation of equation (2.5) [17].

$$\Delta G_r^0 = -\mathrm{R}T \ln (K) \tag{2.4}$$

$$K = \frac{p_{H_2O,eq}}{p_{H_2,eq}\,p_{O_2,eq}^{0.5}} \tag{2.5}$$

$$\Delta G_r = \Delta G_r^0 + \mathrm{R}T \ln Q \tag{2.6}$$

The reaction Gibbs energy can be used to calculate the cell potential at equilibrium and at certain gas compositions. The relationship between the standard reaction Gibbs energy and standard cell voltage is expressed with equation (2.7), where F is the Faraday constant and z is the number of electrons participating in the reaction, $z = 2$ in the case of equation (2.3) [17]. This relation can be further used with equation (2.6) to present the Nernst equation (2.8), which can be used to calculate the cell potential at any feed gas composition and therefore express the available electrical work.

$$\Delta G_r^0 = -zFE^0 \tag{2.7}$$

$$E = E^0 - \frac{\mathrm{R}T}{2F}\ln\left(\frac{p_{\mathrm{H_2O}}}{p_{\mathrm{H_2}}p_{\mathrm{O_2}}^{0.5}}\right) \tag{2.8}$$

The conductivity of the SOC system can be presented as a modified Arrhenius expression with equations (2.9) and (2.10) [18,19], where σ is the conductivity, E_a is the activation energy, T is temperature, and k_B is the Boltzmann constant. These equations can be used to calculate the activation energy E_a for a rate limiting step from electrochemical data measured at different temperatures.

$$\sigma = \sigma_0 e^{-\frac{E_a}{k_B T}} \tag{2.9}$$

$$\ln\sigma = \ln\sigma_0 + \frac{E_a}{k_B}\frac{1}{T} \tag{2.10}$$

4.1.2 Solid Oxide Cell Voltage

In practice, the SOC is operated irreversibly at an overpotential η calculated from the equilibrium cell voltage described by equation (2.8). The total polarization of the SOC is the sum of three types of overpotentials: the activation polarization (also known as charge transfer polarization), ohmic polarization, and the concentration polarization, and is expressed as equation (2.11). [20,21,22]

$$\eta_{tot} = \eta_{act} + \eta_{ohm} + \eta_{conc} \tag{2.11}$$

The activation polarization η_{act} expresses the electrical energy needed to overcome the activation energy barrier of an electrochemical reaction. This overpotential is defined as the Butler-Volmer equation (2.12), where j is current density, j_0 is the exchange current density, α is the symmetry factor, f refers to a constant equal to $F/\mathrm{R}T$, where F is the Faraday constant, R is the universal gas constant, and T is temperature, and finally, η is the overpotential. [17,20,21,22]

$$j = j_0 e^{-\alpha f \eta_{act}} e^{(1-\alpha) f \eta_{act}} \tag{2.12}$$

When current is drawn from the SOC system, it is limited by the internal resistance of the cell, most of which is due to the limited ionic conductivity of the electrolyte. This overpotential is defined by Ohm’s law as in equation (2.13), where R represents the internal resistance of the cell [20,21,22].

$$j = \frac{\eta_{ohm}}{R} \tag{2.13}$$

While the working SOC is constantly supplied with a flow of feed gases, the porous nature of the SOC electrodes often provides some resistance to the flow of reactants and counterflow of products to and from the reaction sites located near the electrolyte. This usually contributes to a decrease in reactant partial pressure at the reaction sites and thus contributes to an overpotential by itself. If enough electrical current is drawn, then the SOC system reaches a point where the current is totally limited by the diffusion of reactants to the reaction sites and the diffusion limited current density j_L is reached. The diffusion limited current density can be calculated by applying Fick's law in equation (2.14), where D is the diffusion coefficient of the reactants, p is the partial pressure of the reactants in gas phase, and δ is the thickness of the diffusion layer. The concentration polarization is defined using j_L as equation (2.15) [20,21,22]

$$j_L = \frac{zFpD}{\delta} \tag{2.14}$$

$$\eta_{conc} = -\frac{\mathrm{R}T}{zF}\ln\left(1 - \frac{j}{j_L}\right) \tag{2.15}$$

Over a voltage vs current density polarization curve for a SOC, different polarization mechanisms could be dominant. At low current densities, the activation polarization is usually dominating but at high current densities, when j is approaching j_L, the concentration polarization becomes the main component of the cell overpotential.

While the cyclic voltammetry method is excellent for estimating the performance of the full SOC and for initial analysis of the current limiting processes, the individual polarization processes need to be separated to assess the impact of each process on the final cell performance. The electrochemical impedance spectroscopy (EIS) is a powerful characterization method that is capable of deconvoluting and describing the current limiting processes if their characteristic parameters are different enough in magnitude.

4.2 Electrochemical Impedance Spectroscopy

The EIS method involves introducing small alternating perturbations to the voltage or current applied on the electrochemical cell at different frequencies and measuring the response, which is often out of phase with the input. The perturbations are usually applied in a sinusoidal fashion such as equation (2.16), with the response coming as equation (2.17) [23]. In these equations V_0 is the voltage amplitude, I_0 is the current amplitude, t is time, ω is the angular frequency of the sinusoidal perturbation, and φ is the phase difference (sometimes called phase shift).

$$v(t) = V_0 \sin(\omega t) \tag{2.16}$$

$$i(t) = I_0 \sin(\omega t + \varphi) \tag{2.17}$$

The transfer function of this system is a complex number (parameter) at the frequency domain called impedance and is defined in equation (2.18) [23]. Impedance represents the total resistance to the current flow in an electrical circuit consisting of resistor elements, capacitor elements, and inductor elements. The real part of the impedance (*Z'*) in equation (2.18) represents the ohmic resistance and the imaginary part (*Z''*) represents the reactance.

$$Z(\omega) = \frac{V_0}{I_0} e^{j\varphi} = |Z|(\cos\varphi + j\sin\varphi) = Z' + jZ'' \tag{2.18}$$

$$Z' = R \tag{2.19}$$

$$Z_{\mathrm{C}}'' = \frac{1}{\omega C} \tag{2.20}$$

$$Z_{\mathrm{L}}'' = \omega L \tag{2.21}$$

The impedance provided by the resistor, capacitor and inductor element components are represented by equations (2.19), (2.20), and (2.21), respectively, where *R* is resistance, *C* is capacitance, and *L* is inductance. Thus, the impedance response of an electrochemical cell to an alternating current can be separated into resistance and reactance parts. An electrochemical cell is usually modelled with an equivalent circuit that consists of a resistor in series connection and one or more (RC) segments of a resistor, and a capacitor connected in parallel. The equation of a resistor and a capacitor in parallel is presented as an equation (2.22). If the parallel (RC) circuit impedance function over a range of frequencies is plotted on a diagram with the x-axis representing *Z'* and the y-axis representing *Z''* (called a Nyquist plot), this impedance will form a semicircle. At a single characteristic frequency, where the reactance and resistance are equal, the imaginary part of the impedance is at a maximum. This characteristic frequency is given in eq. (2.23), where $\tau = RC$ is the characteristic time constant of the system.

$$Z(\omega) = \frac{1}{\frac{1}{R} + j\omega C} = \frac{R}{1 + j\omega RC} = \frac{R}{1 + (\omega RC)^2} - j\frac{\omega R^2 C}{1 + (\omega RC)^2} \tag{2.22}$$

$$\omega_{Z_{max}''} = \frac{1}{\tau} = \frac{1}{RC} \tag{2.23}$$

In solid oxide cell systems, the reactance usually does not act as a perfect capacitor, creating a distribution of characteristic frequencies and resulting in a depressed semi-circle on the Nyquist plot. This behavior is probably due to the microscopically uneven interfaces between the SOFC layers and between the electrode and gas phases that arise from its porous microstructure. Instead of a single time constant, such impedance responses can have a distribution of time constants. This behavior can be fitted with a constant phase element (CPE), which is expressed in equation (2.24) [24,25,26], where T_{CPE} is a CPE constant characterizing the capacitance and ϕ is a CPE exponent, which describes deviation from an ideal capacitive impedance response.

$$Z_{CPE} = \frac{1}{T_{CPE}(j\omega)^{\phi}} \tag{2.24}$$

In the usual experimental setting, the impedance response of an electrochemical cell can have a complicated shape and an impedance specter consisting of more than a single semi-circle. Fitting can be achieved by calculating data to an experimental specter with the complex non-linear least squares regression method. The impedance responses represent different rate limiting steps over the specter of frequencies used to collect the impedance data and as such can be used to analyze different aspects of the electrochemical cell. Deconvoluting the separate semi-circles can pose a challenge. As a rule-of-thumb, semi-circles of an impedance specter can be reliably separated if their characteristic time constants are about 2 orders of magnitude apart.

4.2.1 Impedance Analysis of SOC Devices

The impedance response of a hydrogen electrode supported solid oxide cell is investigated in several publications [12,27,28,29,30]. The impedance response is usually fitted using 5–6 equivalent circuit elements, which correspond to different current limiting processes. These processes, however, have similar characteristic frequencies in the impedance response and may overlap greatly, making proper deconvolution of the impedance data challenging. The impedance spectra measured in this work usually shows 2 to 3 distinguishable semi-circles or depressed semi-circles, which were named as high-frequency impedance process (P_{high}), middle-frequency impedance process (P_{mid}), and low-frequency impedance process (P_{low}).

P_{high} is ascribed to the semi-circle with the characteristic frequency at 1–5 kHz. According to literature, this process describes the charge transfer processes at the reaction sites in the hydrogen electrode, specifically the hydrogen oxidation (in fuel cell mode) or water splitting reactions (in electrolysis mode) [12,27,28].

P_{mid} is ascribed to the semi-circle found in the range of 100–1000 Hz. In the literature [12,27,31], this semi-circle is usually used to describe the oxygen exchange processes on the mixed ionic-electronic conducting (MIEC) oxygen electrode surface. Some studies, however, have identified a hydrogen concentration dependent semi-circle with a characteristic frequency in the 10–500 Hz range and have used it to describe the mass transportation limited processes in the hydrogen electrode [28,29,32].

P_{low} is ascribed to the semi-circle found in the range of 1–10 Hz. This semi-circle is typically used to describe current limiting processes that are related to gas diffusion in the support layer and a process called gas conversion impedance [27,31,32,33]. Some studies have noted that the low-frequency impedance in their system is not significantly affected by temperature changes and thus they have proposed water adsorption and desorption processes at the YSZ and oxidized Ni surface to be related to this impedance process [34,35].

4.3 Time-of-Flight Secondary Ion Mass Spectrometry

The Time-of-Flight Secondary Ion Mass Spectrometry (ToF-SIMS) method is a powerful method for determining the atomic composition of a sample. This method uses a beam of ions to induce sputtering of break-away ions from the sample, called secondary ions, which are then collected into a time-of-flight mass spectrometer.

The generation of secondary ions occurs with the collision between the primary ions in the ion beam and the sample surface atoms. The kinetic energy of the primary ion is transferred to the sample atoms, initiating a cascade of collisions between the atoms of the solid, culminating in the sputtering of some of the atoms or atom clusters from the surface of the sample. Released from the matrix of the sample bulk, some of these sputtered particles may then disassociate into ions, which can be analyzed [36].

The sputtered ions are gathered and accelerated with an electric field through a time-of-flight mass analyzer and into an ion counter. Due to the constant kinetic energy of the primary ions, the initial velocities of the secondary ions vary only by their weight. The acceleration given to the ions from the collecting electric field separates the ions by their mass-to-charge ratios. The time-of-flight analyzer helps expand that separation by increasing the distance of travel, increasing the signal resolution when the ions finally reach the ion counter. Sputtered ions with identical masses can still have different kinetic energies after gathering due to different speed vectors after sputtering. This is counteracted in the ToF-SIMS system with hemispherical electrostatic sector analyzers (ESA), which create a longer flight path for ions with slightly higher energy, helping to concentrate ions with similar mass-to-charge ratios and further increasing signal resolution.

4.4 State of the Art Solid Oxide Cell Composition

The solid oxide cell is a multilayer solid state ceramic device. The heart of the solid oxide cell is the dense oxide-ion conducting electrolyte, which separates the oxygen chamber and hydrogen chamber. To facilitate and accelerate oxidation and reduction reactions on each side of the electrolyte, it is equipped with mixed conducting electrodes. The SoA SOC is usually designed with a very thin electrolyte to minimize the internal resistance of the cell. In such designs, mechanical strength is provided by one of the electrodes. The supporting electrode may consist of multiple layers, where the inner electrolyte adjacent layer, called the active or functional layer, is optimized for electrochemical reactions and the outer support layer is optimized for greater gas diffusivity and mechanical strength. Chemical barrier layers may be employed in cases where risk of chemical reactions between layer materials is present. It is common to have a barrier layer between the oxygen electrode and the electrolyte to inhibit the formation of isolating layers. Finally, porous contact layers are added to the electrodes to ensure good electronic contact with the current collecting plates. A sample microstructure of the SoA SOC featured in this work is shown in Figure 1 as a SEM micrograph.

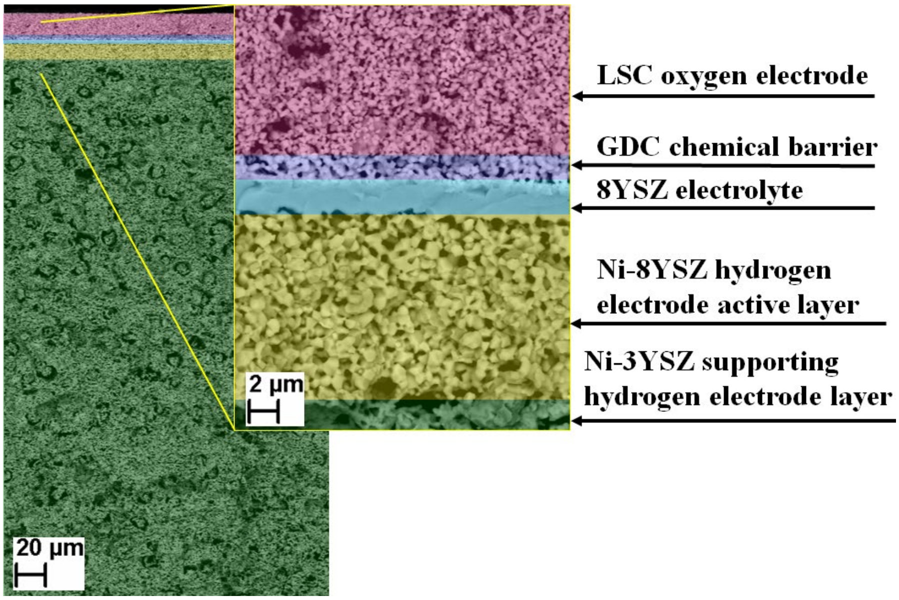

Figure 1. A SEM micrograph of a cross-section of SOC with the layers colour-coded for ease of understanding.

4.4.1 Electrolyte for the Solid Oxide Cell

Oxygen ion conductivity was first observed in a solid solution of 15 wt% Y_2O_3 in ZrO_2 by Nernst in the 1890s [20,37]. Yttria stabilized zirconia (YSZ) is not the only compound that exhibits oxide ion conductivity, but it is one of the more robust materials, showing no electronic conductivity, being made of relatively abundant components and being relatively easy to produce [20]. For these reasons, the 8 mol% YSZ is still the material of choice in the state-of-the-art SOC [38].

At high temperature zirconia has a fluorite structure, which has cations in a face-centered cubic structure with the anions occupying the tetrahedral sites. This leaves relatively open octahedral interstitial sites in the crystal structure, allowing the ion diffusion. The addition of divalent or trivalent, called aliovalent, cations such as Ca^{2+} or Y^{3+} increases the ionic conductivity of zirconia by creating defects in the crystal structure as the requirement to maintain electroneutrality creates oxide ion vacancies in the structure. This reaction is described using the Kröger-Vink notation in equation (2.25). These oxide ion vacancies and the interstitial sites provide substantial oxide ion conductivity of the material. The aliovalent additives also help to stabilize the fluorite structure at lower temperatures, increasing the robustness of the material during manufacturing and operation.

$$\mathrm{Y_2O_3} + \mathrm{O_O^x} + 2\mathrm{Zr_{Zr}^x} \leftrightarrow 2\mathrm{Y'_{Zr}} + \mathrm{V_O^{\cdot\cdot}} + 2\mathrm{ZrO_2} \tag{2.25}$$

Another family of fluorite structured materials of great interest are doped cerium oxides. In general, ceria-based materials have higher ionic conductivity than the conventional YSZ materials and have good chemical and mechanical compatibility with common electrodes [39,40,41]. The main drawback for ceria-based materials is the ability of Ce^{4+} to reduce to Ce^{3+} at low oxygen partial pressures and at high temperatures. The mixture of Ce^{4+} and Ce^{3+} in the electrolyte material allows significant electronic conductivity through the electrolyte, which might lead to partial short-circuiting within the SOC with a purely ceria-based electrolyte, and a decrease in performance [39].

4.4.2 Oxygen Electrode

The oxygen electrode in the SOC is expected to have high electrical conductivity, high catalytic activity for oxygen reduction, good oxide ion conductivity, and mechanical compatibility with other cell components. Some of the most promising material groups developed for the purpose of acting as an oxygen electrode are perovskites. Depending on the host lattice as well as chemical nature and concentration of dopants, temperature and oxygen partial pressure, the electron-hole conductivity of perovskites can range from 10 to 1000 S/cm and the oxide ion conductivity from 10^{-5} to 1 S/cm [22].

Perovskites have an ABX_3 stoichiometry, where A and B are cations, and X represents the anion. The conductivity of perovskite materials can be enhanced by doping the A or B sites with aliovalent cations, which can create point defects (oxide ion vacancies, polarons, etc.) in the material structure through charge compensation that can act as charge carriers. For example, in doping the $La_{1-x}Sr_xCoO_{3-\delta}$, a probable compensation mechanism with oxygen vacancies is illustrated with scheme (2.26) and compensation with electron holes with (2.27). Thus, such A site doping can not only change the cation sublattice but also the oxygen sublattice, often leading to a balance between electronic and ionic charge compensation and resulting in development of the mixed ionic-electronic conductivity.

$$2\mathrm{SrO} + 2\mathrm{La_{La}^x} + \mathrm{O_O^x} \leftrightarrow 2\mathrm{Sr'_{La}} + \mathrm{La_2O_3} + \mathrm{V_O^{\cdot\cdot}} \tag{2.26}$$

$$2\mathrm{SrO} + 2\mathrm{La_{La}^x} + \frac{1}{2}\mathrm{O_2} \leftrightarrow 2\mathrm{Sr'_{La}} + \mathrm{La_2O_3} + 2\mathrm{h^{\cdot}} \tag{2.27}$$

The classical material for the oxygen electrode is the $La_{1-x}Sr_xMnO_{3-\delta}$ (LSM), though in state-of-the-art cell structures the A-site deficient $(La_{1-x}Sr_x)_{0.95}CoO_{3-\delta}$ (LSC) or $(La_{1-x}Sr_x)_{0.95}Co_{1-y}Fe_yO_{3-\delta}$ (LSCF) are used. While LSM has good stability and compatibility with the 8YSZ electrolyte material, oxide ion conductivity is lacking. The LSC and LSCF are much more active electrode materials but incompatible with the ZrO_2 based electrolytes. Lanthanum and strontium from the LSC and LSCF structures can migrate into the zirconia and react to form $La_2Zr_2O_7$ and $SrZrO_3$ phases, which have poor ionic conductivity [40]. For this reason, a chemical barrier layer is applied between the electrolyte and the oxygen electrode. GDC is the main material of choice for this application due to its high oxide ion conductivity and greater chemical stability with most materials used for oxygen electrodes [20,40].

4.4.3 Hydrogen Electrode for the Solid Oxide Cell

As the reaction site for hydrogen and water conversion (depending on the operation mode), the hydrogen electrode is required to be stable in wide range of oxygen partial pressures, to have good electronic conductivity, gas permeability, catalytic activity for hydrogen oxidation reactions and water splitting reactions and have good chemical and mechanical compatibility with the electrolyte. A key part of the hydrogen electrode is the reaction sites, where the oxide ion conducting phase, electron conducting phase and reagent providing gas phase meet, called the three-phase boundary (TPB).

Nickel is chemically stable under reducing conditions, highly active for the hydrogen evolution reaction and tolerant to the conditions at high steam partial pressures. As a drawback Ni has a significant thermal expansion mismatch with zirconia, causing possible delamination during rapid heating and cooling, and the metal has high surface mobility in humid environments which may lead to loss of the electron conductive network through Ni grain growth, especially at electrolysis operating conditions [42].

To decrease the above-mentioned effects, composites of metals and ceramics, cermets, have been developed. In cermet electrodes, the ceramic part usually forms the backbone of the microstructure, and the metal part acts as the catalyst. The SoA SOC hydrogen electrodes are usually either Ni-YSZ, Ni-ScSZ or Ni-GDC cermets. The YSZ or GDC helps the cermet form and maintain good adhesion to the ceramic electrolyte and provides the rigid structure, inhibiting Ni aggregation and grain growth. YSZ and GDC backbones also provide oxide ion conductivity, enabling the extension of reaction sites further into the electrode volume and thus increasing the length of TPB. The metal network part acts as the main catalyzing agent and as an electron conductor to the current collector.

Depending on the design of the SOC device, the hydrogen electrode may be multilayered. The SoA SOC is usually made as either electrolyte supported or electrode supported cells, depending on which layer is supposed to provide the bulk of the mechanical strength for the cell. If the hydrogen electrode is the supporting layer, then it is common for the SOC to have a 0.3–1 mm thick electrode. In such cases, it is important to control and optimize the pore and particle size in the layer and even create a multilayered design. The thick supporting electrode layer is usually engineered to have larger particles and larger pores to minimize the diffusion resistance to the feed gas flow, while the thin hydrogen electrode active layer (HEAL) has smaller pores and particles to maximize TPB density.

Nickel is not the only catalyst of interest proposed for the hydrogen electrode. Theoretical studies for water electrolysis on metal and metal alloy catalysts, published by Cho et. al. [43] and Gu and Nikolla [44], predict an increase in performance for Ni-Fe and Ni-Co alloy catalysts over a pure Ni catalyst for electrolysis mode. Experimental studies alloying Ni with Fe in the hydrogen electrode have shown suppressed Ni coarsening, increased redox stability, and improved SOC performance in fuel cell operation conditions [45,46,47]. Similar studies with Ni and Co alloys suggest increased SOC activity and greater redox stability in both fuel cell and electrolysis operation modes [45,48,49,50].

GDC is also often used as a backbone ceramic material in SoA SOC devices as it is also known to be catalytically active towards the hydrogen evolution reaction. An extra benefit in reducing conditions is its ability to become a mixed ionic-electronic conductor, potentially extending the reaction zone from the TPB further across the ceria surface [51,52]. These benefits could also be realized by modifying the YSZ materials with GDC. As an example, Grimes et al. [53] reported decreased overall polarization resistance of a button type cell where GDC was infiltrated into a Ni-YSZ matrix.

5. EXPERIMENTAL

5.1 Structure and Composition of Samples

This work analyzes the results of 2 long-term experiments and 8 short-term button type cell experiments. The long-term and short-term experiments used SOC with different sizes and architectures, although they had similarly manufactured half-cells. The half-cell is a sub-assembly, which consisted of a NiO contact layer (~5 µm), a NiO/3YSZ diffusion layer (supporting structure, ~380 µm), a NiO/8YSZ hydrogen electrode active layer (HEAL, ~12 µm) and an 8YSZ electrolyte (~3 µm). The long-term tests were conducted on rectangular solid oxide cells made from commercially produced half-cells with the barrier and oxygen electrode layers prepared in the lab (not industrial). The barrier layer was made from a commercial GDC paste (ESL) that was screen-printed on top of the half-cell and sintered at 1300 °C for 30 hours. The oxygen electrode was made from $Pr_{0.6}Sr_{0.4}CoO_{3-\delta}$ (PSC), which was produced by the glycine nitrate process method and mixed into a paste as described in previous paper [54]. The PSC paste was screen printed in a 3.5x4 cm rectangular shape, and this defined the active area of the SOC. Finally, a $La_xSr_{1-x}CoO_{3-\delta}$ (LSC) contact layer was applied to the oxygen electrode to ensure good contact with the current collector. A SEM image of the cell cross-section is provided in Figure 2.

The NiO/3YSZ diffusion layer acted as the supporting layer, which provided mechanical strength to the SOC. Additionally, the diffusion layer provided the HEAL access to feed gas through large pores and provided electronic conductivity between the active layer and the current collector.

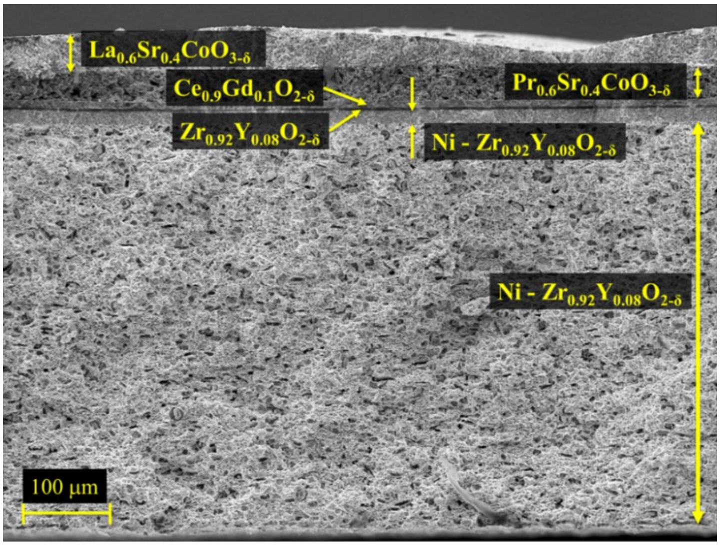

Figure 2. SEM image of a cross section of the SOFC after the experiment.

The state-of-the-art solid oxide cells used in the button cell tests were produced in Elcogen AS using industrial methods and modified through changing the active electrode production parameters. A reference SOC is shown in Figure 1, and it consisted of 5 functional layers and 2 contact layers. The layers were a NiO contact layer (~5 µm), a NiO/3YSZ diffusion layer (~380 µm), a NiO/8YSZ hydrogen electrode active layer (HEAL), an 8YSZ electrolyte (~3 µm), a $Gd_xCe_{1-x}O_{2-\delta}$ (GDC) barrier layer (~2 µm), $La_xSr_{1-x}CoO_{3-\delta}$ (LSC) oxygen electrode layer (~15 µm) and an LSC oxygen electrode contact layer (~8 µm).

To investigate the effect of the HEAL thickness on the performance of the SOC, 5 different samples were prepared. The thicknesses of these samples were 0, 7, 12, 16 and 20 µm. Cross-sections of these cells are presented in Figure 3.

The investigation of chemical changes of the HEAL was carried out with another 3 button type cell samples, where the change was introduced during manufacturing by modifying the ceramic powder used to screen-print the active layer. The HEALs of the cells consisted of $Ni_{0.9}Fe_{0.1}$-8YSZ, $Ni_{0.9}Co_{0.1}$-8YSZ, and Ni-$(8YSZ)_{0.9}(GDC)_{0.1}$. Table 1 shows how the modified cells are referred to in this work.

Table 1. Tested cells and their HEAL composition.

HEAL COMPOSITION	SHORT NAME OF THE TEST CELL
Ni-8YSZ	Reference
Ni-$(8YSZ)_{0.9}(GDC)_{0.1}$	YSZ-GDC
$Ni_{0.9}Co_{0.1}$-8YSZ	Ni-Co
$Ni_{0.9}Fe_{0.1}$-8YSZ	Ni-Fe

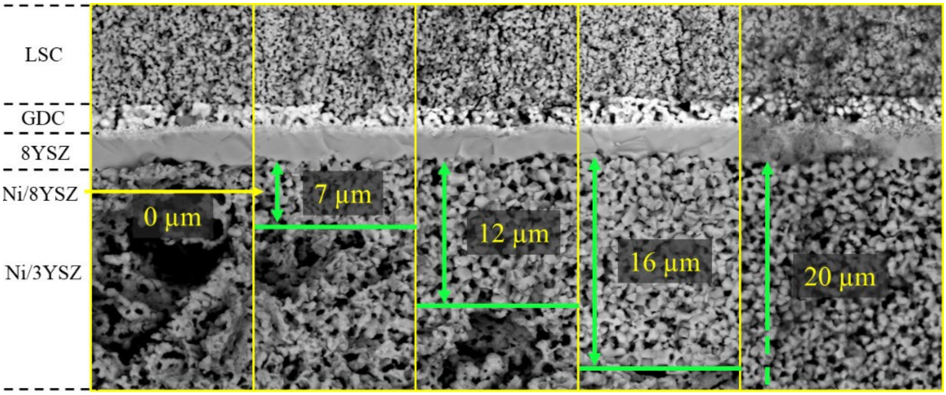

Figure 3. SEM micrographs depicting broken cross-sections of the SOCs studied in this work with the focus on the HEAL. The thicknesses of the layers are given on the micrographs.

5.2 Electrochemical Test Setup

5.2.1 Assembly of the Long-Term Test Setup

The long-term tests and short-term button cell tests were conducted in two different electrochemical test set-ups. The long-term test rig was provided by Fuel Cell Materials (FCM) and modified in-house. A single-stack furnace (Mellen), which also enabled pressure loading of the SOC assembly, together with current collectors provided by FCM, was used as the electrochemical reactor. To create electrical contact between current collector plates and electrodes, Ni ink (FCM) and Ni mesh (FCM) were used in the hydrogen electrode side and LSC ink (FCM) and silver mesh (FCM) in the oxygen electrode side. The current collector plates were sealed with a mica gasket (FCM) and glass paste (G018 354, Schott) to achieve gas tightness of the cell. A schematic of the current collector and test cell assembly is provided in Figure 4.

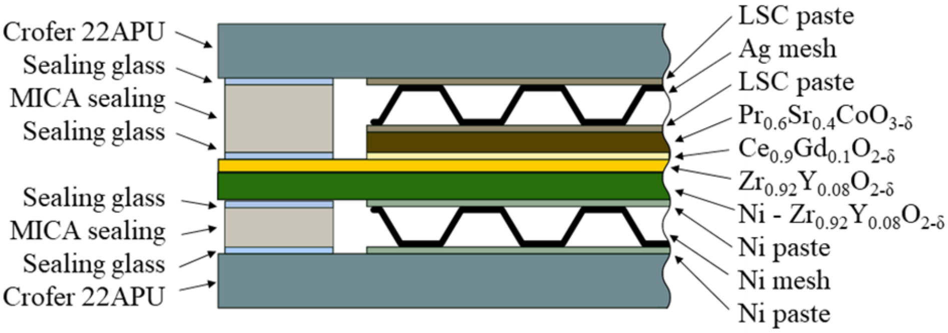

Figure 4. Schematic drawing of the membrane electrode assembly for electrochemical measurements.

Gas flow was provided to the SOC through holes in the current collector, and the gas flow conditions were controlled with Bronkhorst mass flow controllers. The feed gas to the hydrogen chamber and air to the oxygen chamber were provided in opposite directions. A bottle of $^{18}O_2$ oxygen isotope was also connected through a mass flow controller to the air chamber for use at the end of the test. The feed gas line for the hydrogen chamber in the electrolysis test was equipped with a membrane humidifier (FC100, Perma Pure LLC) that was fed with de-ionized water heated using a Julabo Corio-CD water bath circulator. The amount of steam the membrane could provide to the feed gas was controlled by the temperature of the water circulated through the water bath.

To condition the test rig, the assembly was heated to 850 °C at a rate of 3 °C/min and kept there for 1 hour before cooling to 800 °C to start the fuel electrode reduction. The reduction was conducted by introducing a gas mixture of 5%

hydrogen in nitrogen into the hydrogen electrode room. The concentration of hydrogen was gradually increased to 100% over a period of 4 hours.

The long-term tests were performed in fuel cell mode and electrolysis mode. The gas flow rate in the long-term fuel cell test was 50 ml/min to induce a reactant gradient along the electrode area while the gas flow in the oxygen chamber was 250 ml/min. For the electrolysis test the hydrogen chamber was fed a mixture of 20% hydrogen and 80% nitrogen through a humidifier at 80 °C, enriching the hydrogen gas with around 46% steam. The composition of feed gas in the hydrogen chamber was 46% water, 10.8% hydrogen, and 43.2% nitrogen with the total gas flow being 185 ml/min. The gas flow in the oxygen chamber was 250 ml/min like the fuel cell test.

The long-term fuel cell test data were collected with a BK Precision 8500 Programmable DC Electronic load connected with a PC. The electronic load was also used to record current density data at 0.8, 0.9, and 1 V to construct j vs E curves during the test in fuel cell mode. Power for the electrolysis test was supplied by an AIM-TTi QPX1200SP power supply connected with a PC. EIS data was also collected during the electrolysis test, and these were collected using the Solartron Analytical 1400 and 1470E CellTest system.

After the long-term test, the 5×5 cm SOCs were removed from the test rig and broken into pieces to analyze the cell cross-sections at 36 different positions over the surface of approximately equal distance from another. These cross-sections were characterized using the ToF-SIMS and HR-SEM methods. The PHI TRIFT V nanoTOF time-of-flight secondary ion mass spectrometer (Physical Electronics, Inc. (PHI)) was used to scan in both positive and negative ion regimes within a raster of 100x100 µm or 50x50 µm (Ga^+, 30keV). The microstructural characterization was done using the Zeiss EVO MA 15 HR-SEM.

5.2.2 Assembly of the Short-Term Button Cell Test Setup

The button cell tests were conducted in a Norecs Probostat test rig, heated in a Carbolite tube furnace. A schematic diagram of the Probostat configuration is shown in Figure 5. The feed gas was provided with Bronkhorst mass flow controllers, and the humidity was provided either with a Nafion tube humidifier (FC100, Perma Pure), connected to a water bath circulator (Corio-CD, Julabo) or with an evaporator unit (HovaCAL, IAS). Gas tightness between the hydrogen and air chambers was achieved with a gold sealing ring by heating the reactor, at a rate of 1 ˚C/min, up to 1015 °C for 1h before cooling to operating temperature. The contacts were made of a platinum mesh on the hydrogen electrode and a gold mesh on the oxygen electrode, which were spring-loaded onto the button cell.

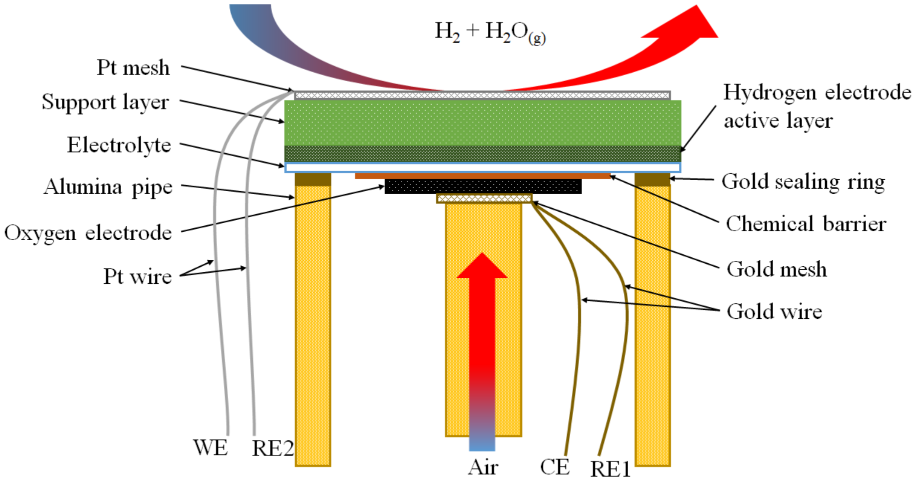

Figure 5. Scheme of the test cell configuration within the testing rig. The components are mentioned in the diagram.

The cells were conditioned by slowly reducing the hydrogen electrode over at least 2 hours at 800 °C in a 5% H_2, 95% N_2 gas mixture. Thereafter, the H_2 concentration was gradually increased to 100% over 3 hours to achieve full reduction of the electrode. Finally, steam was added to the feed gas until the required partial pressure was achieved at the electrode. The gas flow rate in the button cell tests was kept at 100 ml/min on both sides to keep a constant reactant concentration over the electrode area.

The button cells were characterized with CV and EIS methods using a multichannel test system (CellTest 1400 and 1470E, Solartron Analytical; PARSTAT MC, Ametek) or a combination of a potentiostat (1287, Solartron) and a frequency analyzer (1260, Solartron). Before testing in electrolysis mode, the button cells were tested in SOFC conditions at 700, 750 and 800 ˚C in H_2 with 3% steam concentration. Electrochemical characterization in electrolysis mode was performed at the same temperatures while feeding the cells with gas mixtures of hydrogen and 22.5%, 45%, 67.5%, and 90% steam. Electrochemical impedance spectra were collected at current densities of -0.33 A/cm^2 and -0.66 A/cm^2. EIS measurements were recorded at 20 points/decade in the frequency range of 100 kHz to 0.1 Hz. The system voltage was always varied between -0.75 V and -1.5 V to avoid intense degradation processes caused by excessive polarization.

The measured EIS data were analyzed using the Zview (Scribner Associates, Inc.) software. Using the complex non-linear least squares (CNLS) fitting method the impedance spectra were fitted to theoretical equivalent circuits consisting of an inductive element and resistor in series, following 2–4 units of a resistor and constant phase element in parallel. The theoretical equivalent circuit was developed based on empirically distinguishable semi-circles in the measured impedance spectra. The equivalent circuit used for cells with different HEAL thicknesses and an example fit are both shown in Figure 6. The chemically modified button cells were fitted with a different model, as illustrated in Figure 7, due to achieving better fitting results. The 5–200 kHz spectral region was strongly affected by the inductive effects of the used test rig. Therefore, only inductively unaffected spectral regions were used for analysis.

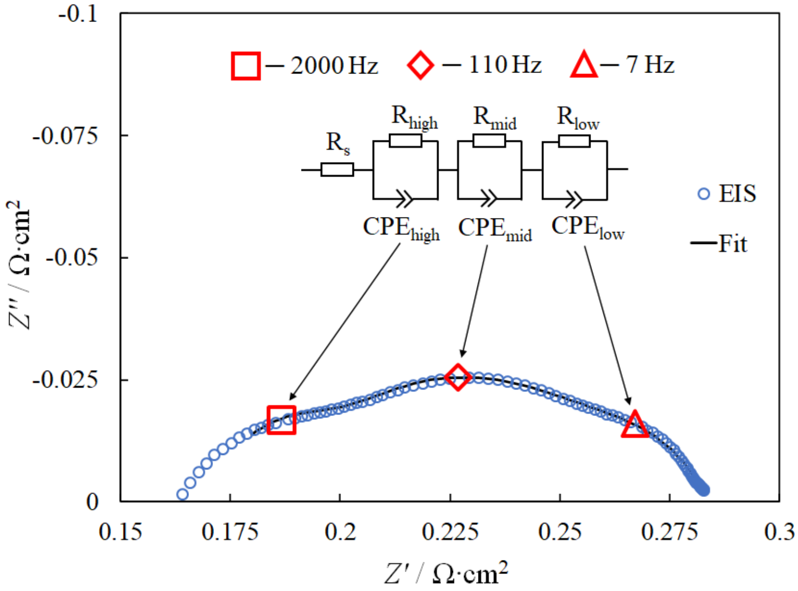

Figure 6. Nyquist plots of a Ni-YSZ|YSZ|LSC button cell measured at -330 mA, 45% H_2O and 55% H_2 gas stream at 700 °C (circles), fitting result (solid line) obtained using CNLS fitting method and the equivalent circuit used for fitting. R_s represents series resistance, R_{high}, R_{mid}, and R_{low} represent polarization resistances of high, mid-, and low frequency processes P_{high}, P_{mid} and P_{low}, respectively. CPE_{high}, CPE_{mid} and CPE_{low} are the constant phase elements describing limiting processes from high to low frequency.

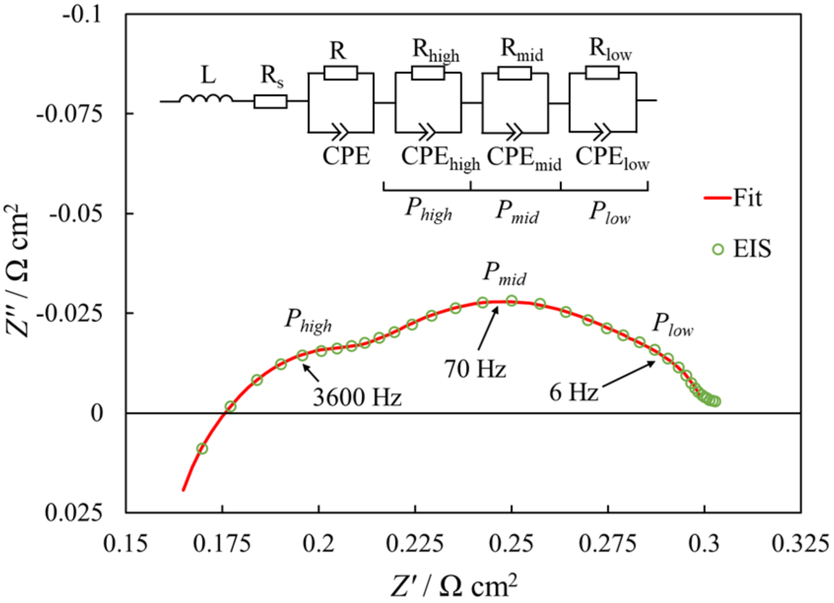

Figure 7. Nyquist plots of a Ni-YSZ|YSZ|LSC button cell measured at -330 mA/cm^2, 45% H_2O and 55% H_2 gas stream at 700 °C (circles), fitting result (solid line) obtained using CNLS fitting method and the equivalent circuit used for fitting. R_s represents high frequency series resistance, R_{high}, R_{mid}, and R_{low} represent polarization resistances of high, mid-, and low frequency processes P_{high}, P_{mid} and P_{low}, respectively. CPE_{high}, CPE_{mid} and CPE_{low} are the constant phase elements describing limiting processes from high to low frequency.

6. RESULTS AND DISCUSSION

6.1 Solid Oxide Cell Degradation During Long-Term Operation

6.1.1 Long-Term Fuel Cell Operation

The long-term fuel cell test was conducted at 0.85 V and 650 °C. The test lasted for 17820 hours. The recorded current density of the fuel cell is shown in Figure 8. The cell degraded at a high rate, around 2.4% per 1000 h, which noticeably decreased after around 10000 hours of operation to around 1.1% per 1000 h. This deactivation process has been reported by others, such as Lim et al. [55] and Tao et al. [11] although at significantly shorter time frames.

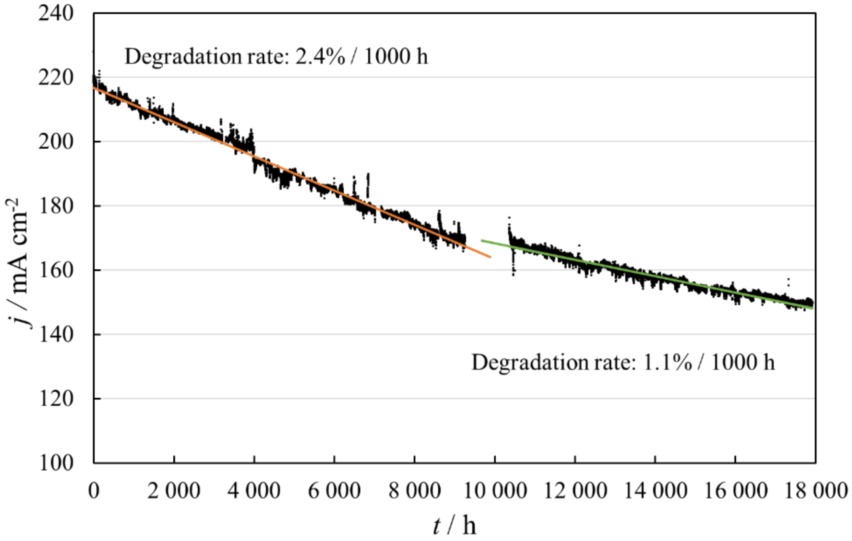

Figure 8. SOC performance evolution throughout the 17820-hour fuel cell test at 650 °C and 0.85 V operating voltage.

The fuel cell test was briefly stopped after 0, 3240, 10370, and 17820 hours of operation to collect j vs E data. The j vs E curves were constructed by recording electrical current values at OCV, 0.8, 0.9, and 1 V at temperatures 600, 650, 700 and 750 °C. The curves recorded at the beginning and at the end of the test are presented in Figure 9. The j vs E data was used to calculate activation energies at operating voltages of 1, 0.9 and 0.8 V and is presented in Table 2.

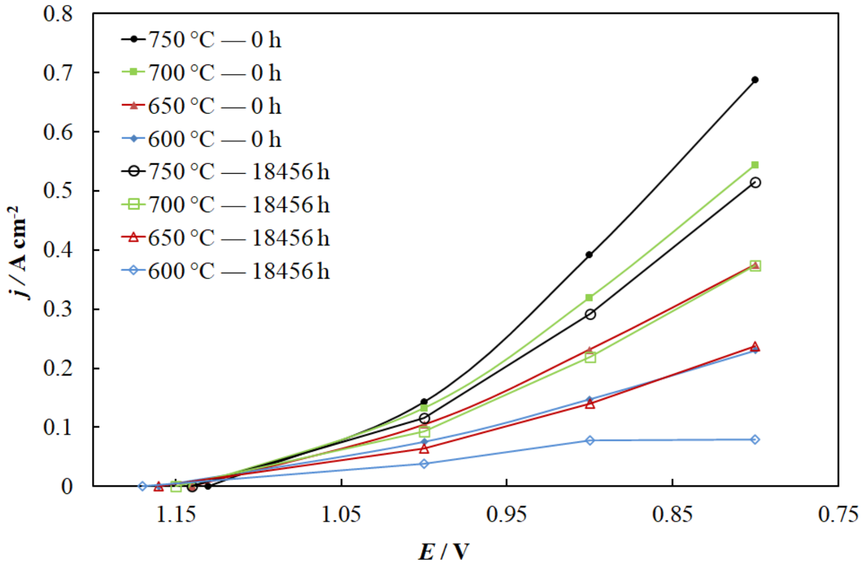

Figure 9. *j* vs *E* data collected during the long-term SOFC durability test.

Table 2. Total activation energies of the Ni-YSZ|YSZ|GDC|PSC fuel cell at different voltages throughout the test.

Operation time	$E_{a\ tot}$ at 0.8 V	$E_{a\ tot}$ at 0.9 V	$E_{a\ tot}$ at 1V
0 h	-0.57 eV	-0.50 eV	-0.34 eV
3240 h	-0.65 eV	-0.61 eV	-0.45 eV
10370 h	-0.69 eV	-0.65 eV	-0.51 eV
17820 h	-0.95 eV	-0.68 eV	-0.56 eV

Depending on at which point on the *j* vs *E* curve the activation energy is measured, one could characterize different reasons for the cell voltage loss, depending on which voltage loss mechanism is dominant [20]. When the applied potential was low, at 1 V, the change in total activation energy from the beginning to the end of the test was around 0.22 eV. At 0.9 V, the change of activation energy was 0.18 eV, and at 0.8 V the activation energy change was much higher, 0.38 eV. This suggests that the degradation of the SOC was mainly led by increasing concentration overpotential. As the mechanical structure and porosity of the cell most likely did not degrade so quickly, the degradation was probably caused by slight microstructural or chemical changes in the HEAL or the oxygen electrode. Similar experiments where a single cell was tested in contact with Crofer 22APU steel without special coating have shown comparable total degradation results [56].

6.1.2 Long-Term Electrolysis Operation

The long-term electrolysis test was conducted at 1.5 V and 800 °C and lasted for 860 hours. The electrolysis performance throughout the test is presented in Figure 10. The average degradation rate during operation was 16% per 1000 h, though performance recovered abruptly by around 3–5% after operation was interrupted to perform EIS measurements. A similar phenomenon was observed by Hjalmarsson et al. [28,57] during their long-term electrolysis test. This recovery process has been attributed to the clearing of poisonous impurities, such as silica, from TPBs.

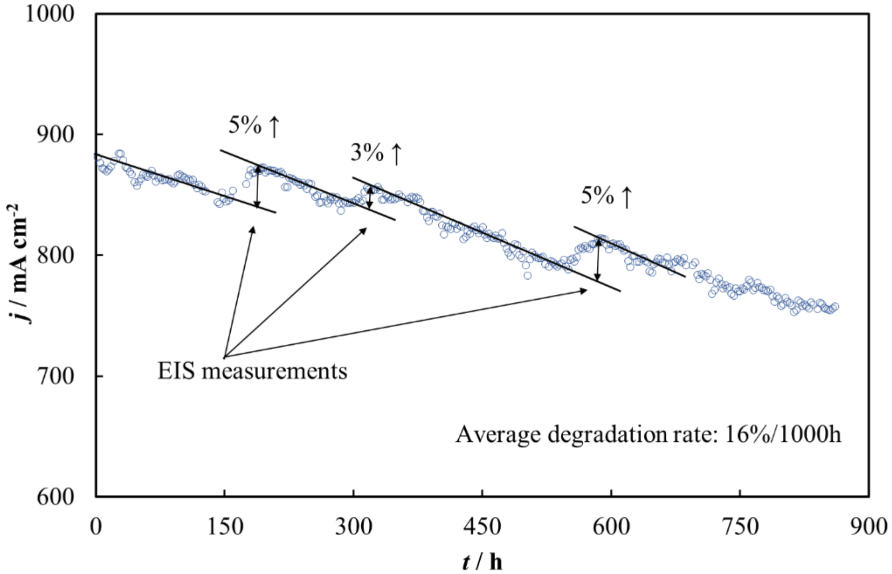

Figure 10. Dependence of current density on operating time of the Ni-YSZ|YSZ|GDC|PSC SOEC short stack measured at T = 800 °C and at E = 1.5 V. A regeneration phenomenon can be seen after electrochemical impedance spectroscopy measurements.

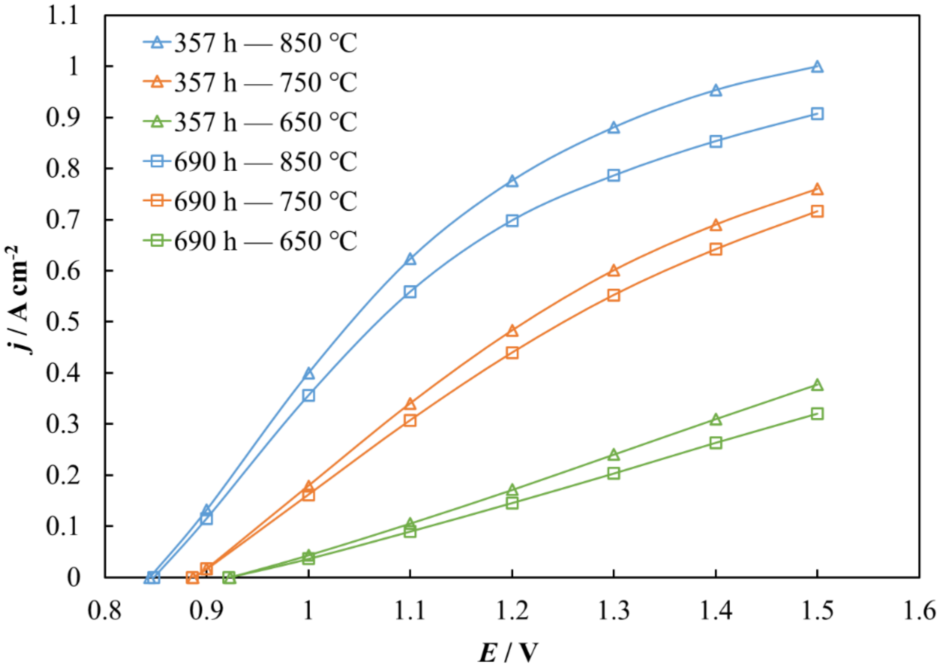

Figure 11. Current density vs. cell potential curves of the SOC short stack in the electrolysis regime at different operation times and temperatures noted in the figure.

The *j* vs *E* curves shown in Figure 11 confirm degradation during the electrolysis test. The linear shape of the *j* vs *E* curves at lower temperatures (650 °C) indicates prevalence of ohmic limitations of the system components at these conditions. At higher temperatures (750 to 850 °C) the conductivity of system components and electrochemical reaction rates were high enough to cause a situation where at operating voltages from 1.1 to 1.5 V the diffusion of water in porous hydrogen electrodes became the prevalent current limiting process, as indicated by the curved shape of the *j* vs *E* curve.

Table 3 shows calculated activation energy values to get more information on the degradation behavior. During the operation time of the electrolysis test, the total activation energy at lower voltages, 1 and 1.1 V, decreased while at higher voltages, 1.2 to 1.5 V, it increased. This behavior suggests that the degradation driving process mostly affected cell performance at higher cell voltage and current density. The measured Nyquist plots in Figure 12 show how the polarization resistance of the low frequency semi-circle, which is usually ascribed to mass transfer limitation (gas diffusion) [27], became the main component of the cell impedance at 1.3 and 1.4 V. The mid-frequency semi-circle with a characteristic frequency of 200–400 Hz, which has been connected to reactant transport processes in the hydrogen electrode active layer, also increased with increasing cell voltage.

Table 3. Activation energies of the electrolysis cell at different voltages and time.

Operation time	***Ea tot* at 1V**	***Ea tot* at 1.1V**	***Ea tot* at 1.2V**	***Ea tot* at 1.3V**	***Ea tot* at 1.4V**	***Ea tot* at 1.5V**
0 h	0.56 eV	0.42 eV	0.31 eV	0.22 eV	0.17 eV	0.14 eV
357 h	0.52 eV	0.41 eV	0.34 eV	0.27 eV	0.22 eV	0.17 eV
690 h	0.50 eV	0.40 eV	0.34 eV	0.28 eV	0.23 eV	0.18 eV

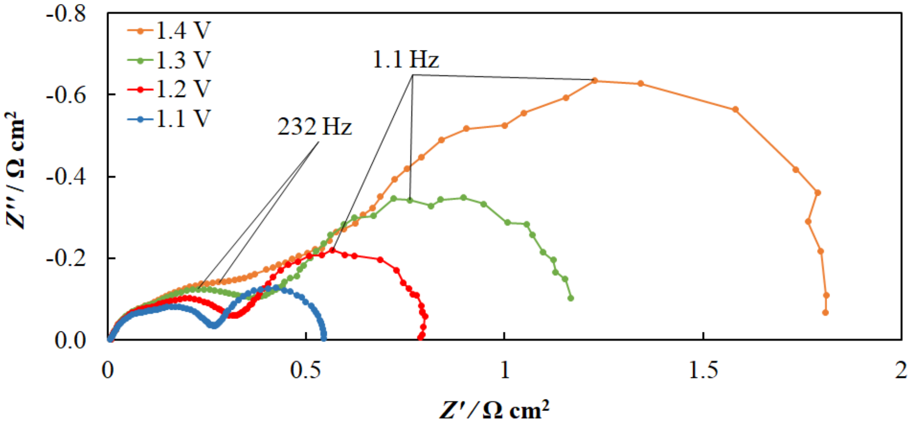

Figure 12. Effect of voltage (noted in figure) on impedance of the electrolysis cell. Nyquist plots were measured 174 h from the start of electrolysis test. T = 800 °C.

Impedance spectra in Figure 13, measured at 1.2 V over the course of the electrolysis test, shows the greatest increase of impedance from the mid-frequency limiting process. As this process is related to mass transfer in the hydrogen electrode active layer, these changes suggest that the loss of reaction sites may have been a probable degradation driving mechanism.

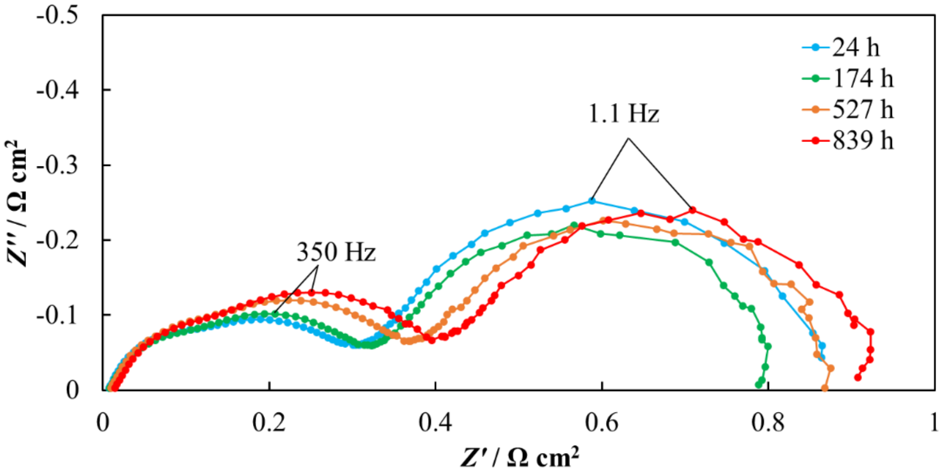

Figure 13. Dependence of polarization impedance of Ni-YSZ|YSZ|GDC|PSC short stack on time measured in electrolysis mode. T = 800 °C, E = 1.2 V. EIS measurements were carried out at 4 different operation times, which are noted in the figure.

6.1.3 Electrode Activity Analysis Using the O^{18} Tracing Method

The Solid oxide cells employed in the long-term tests were 50×50 mm surface area with an active layer of 35×40 mm. Gas flows used during the tests were modest to achieve a gradient of fuel and oxygen concentration along the cell. Thus, it was assumed that cell activity was not constant over the cell area. To map cell activity at different regions, the oxygen $^{18}O_2$ isotope was introduced under load at the end of the test. The exposure to $^{18}O_2$ was limited to avoid saturating the cell. After cooling the cell, it was broken into multiple shards, and their cross-sections were characterized at 36 places along the active area, in a 6×6 grid. Each shard cross-section was analyzed with the ToF-SIMS method to determine the ratio of ^{18}O to ^{16}O. Figure 14 shows the resulting activity map that was composed using the ToF-SIMS data and supplemented with selected SEM micrographs and grain size vs. activity measurement results. ^{18}O concentration was higher at the hydrogen inflow, opposite to the oxygen inflow. Because these areas incorporated considerably more oxygen-18 ions, it is reasonable to assume that the current of oxide ions through the membrane during operation was also larger at these regions, i.e., the fuel cell activity was also higher at hydrogen inflow areas. At areas with higher activity, there should have been a higher temperature, more humidity and, because of that, a more active Ni coarsening process [11,58,59]. HR-SEM micrographs were taken from pieces with different ^{18}O content, and the ^{18}O to ^{16}O ratio was correlated with microstructural parameters. Analysis of the micrographs using the ImageJ tool suggested the existence of a nickel coarsening phenomenon and a correlation between Ni grain size and activity (described by the ^{18}O ratio in sample) was verified. Samples of micrographs with different grain sizes and the correlation graph is presented in Figure 14.

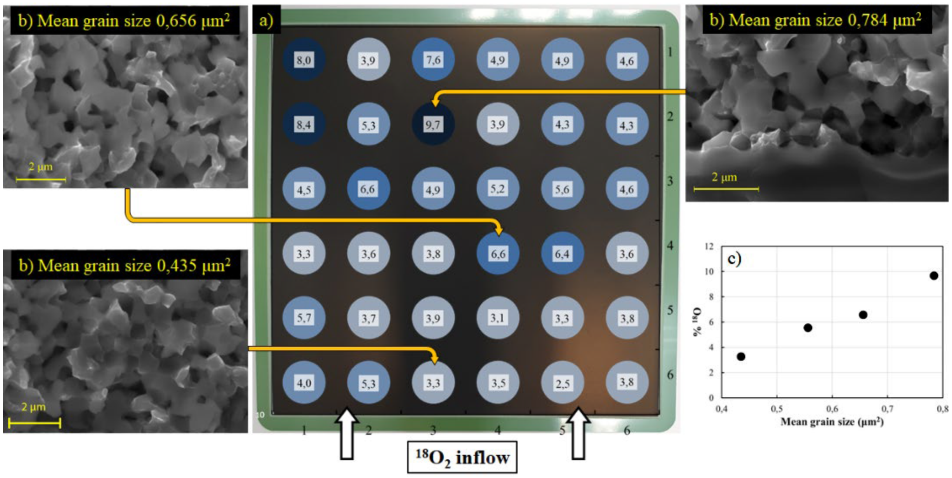

Figure 14. Multi-panel figure of data gathered from the 2-year long fuel cell test containing (a) the ^{18}O ratio map created from ToF-SIMS data from the active Ni-YSZ fuel electrode, (b) HR-SEM pictures from some sample regions with calculated mean Ni-YSZ grain sizes and (c) correlation between measured mean grain sizes and ^{18}O ratios at certain regions.

A similar ^{18}O based activity mapping was done for the SOEC test cell, which results are given in Figure 15. An important difference from the SOFC activity map was the overall lower ^{18}O content in the cell. This may be due to the higher temperature during the ^{18}O introduction. While higher temperature should facilitate faster oxygen exchange and therefore faster ^{18}O incorporation, after this step the higher temperature and the subsequent longer cooldown duration could also increase the possibility of the newly introduced oxygen isotope to diffuse out of the cell.

According to the mapping results, the most active areas of the SOEC appeared to be in the middle of the cell instead of the hydrogen and steam inlet. HR-SEM images revealed that, similar to the SOFC test results, Ni particles size in the SOEC was in correlation with increased ^{18}O concentration. In general, the Ni particles seem to be larger in the SOEC than in the SOFC mode. This can be due to the higher operating temperature, which could have increased the rate of coarsening [59].

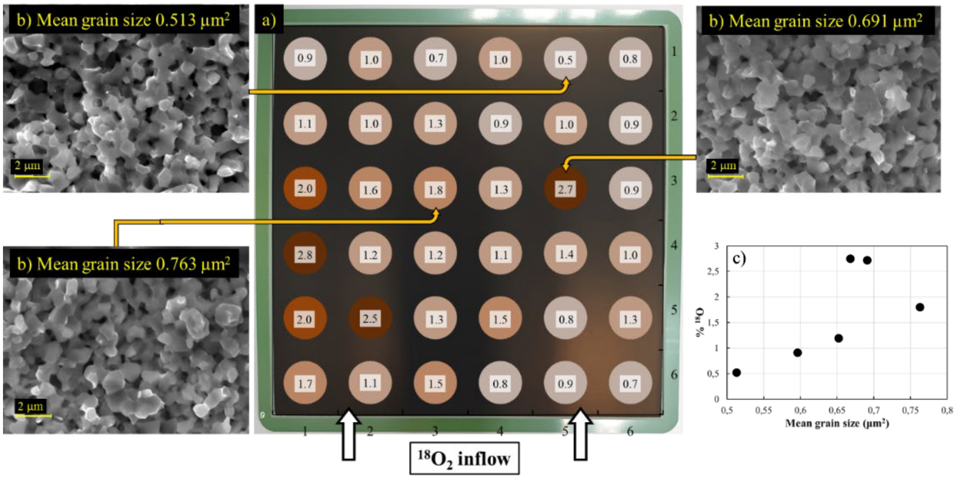

Figure 15. Multi-panel figure of data gathered from the 860 hour long electrolysis test containing (a) the ^{18}O ratio map created from ToF-SIMS data from the active Ni-YSZ fuel electrode, (b) HR-SEM pictures from near some sample regions with calculated mean Ni-YSZ grain sizes and (c) correlation between measured mean grain sizes and ^{18}O ratios at certain regions.

6.1.4 Degradation Analysis Using the ToF-SIMS Method

A reasonable assumption to the cause of deactivation of reaction sites would be poisoning effects. To analyze this, the ToF-SIMS was used to detect the concentration of chromium in the oxygen electrode and the concentration of silicon in the hydrogen electrode active layer. Chromium and silicon deposition on active sites in the oxygen and hydrogen electrodes respectively, are well known degradation mechanisms [10,59,60,61].

A significant amount of chromium was detected in the PSC oxygen electrode and the GDC barrier layer. The Cr concentration map formed with the ToF-SIMS data from the fuel cell test is given in Figure 16 and from the electrolysis test in Figure 17. Most oxygen electrode regions of the SOFC test cell contained 2–3% Cr with some areas in the middle part having less than 1% Cr. While it seems to be a plausible degradation mechanism, the map does not fully align with the ^{18}O permeation map, except for a few areas, where high ^{18}O permeation coincides with low Cr concentration.

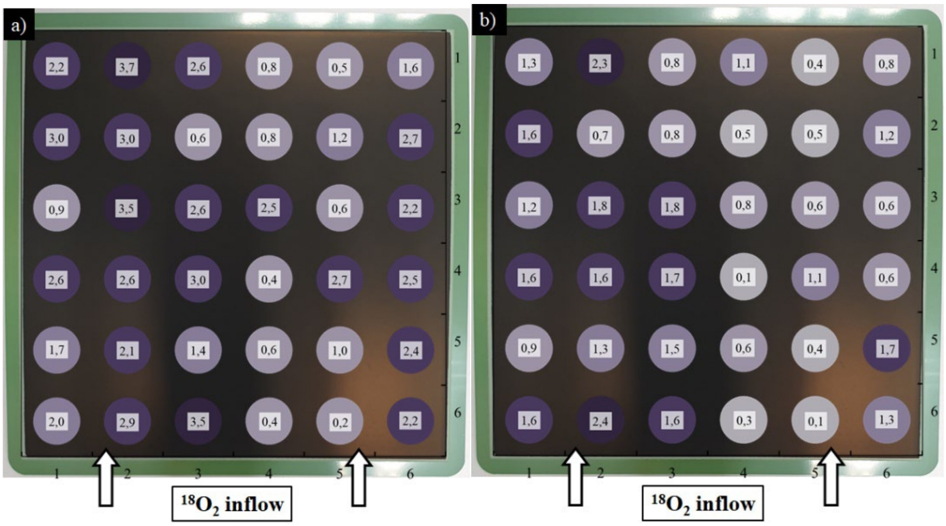

a)

	1	2	3	4	5	6
1	2,2	3,7	2,6	0,8	0,5	1,6
2	3,0	3,0	0,6	0,8	1,2	2,7
3	0,9	3,5	2,6	2,5	0,6	2,2
4	2,6	2,6	3,0	0,4	2,7	2,5
5	1,7	2,1	1,4	0,6	1,0	2,4
6	2,0	2,9	3,5	0,4	0,2	2,2

b)

	1	2	3	4	5	6
1	1,3	2,3	0,8	1,1	0,4	0,8
2	1,6	0,7	0,8	0,5	0,5	1,2
3	1,2	1,8	1,8	0,8	0,6	0,6
4	1,6	1,6	1,7	0,1	1,1	0,6
5	0,9	1,3	1,5	0,6	0,4	1,7
6	1,6	2,4	1,6	0,3	0,1	1,3

Figure 16. Chromium content in the PSC electrode (a) and in the GDC chemical barrier layer (b) of the fuel cell. The values represent the ratio of Cr counts to the total positive ion counts. The arrows denote the direction of air flow at the oxygen electrode side.

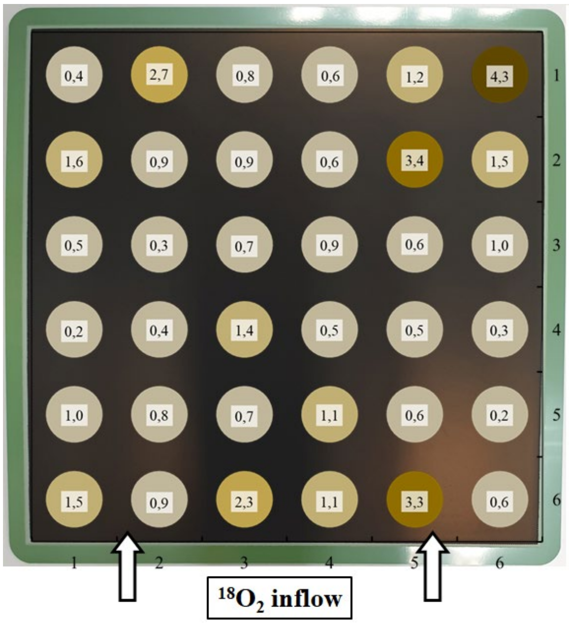

	1	2	3	4	5	6
1	0,4	2,7	0,8	0,6	1,2	4,3
2	1,6	0,9	0,9	0,6	3,4	1,5
3	0,5	0,3	0,7	0,9	0,6	1,0
4	0,2	0,4	1,4	0,5	0,5	0,3
5	1,0	0,8	0,7	1,1	0,6	0,2
6	1,5	0,9	2,3	1,1	3,3	0,6

Figure 17. Chromium content in the PSC oxygen electrode from the electrolysis test cell. The values represent the ratio of Cr counts to the total positive ion counts. The arrows denote the direction of air flow at the oxygen electrode side.

The SOEC test had a significantly lower overall Cr concentration in the oxygen electrode with most testing samples having less than 1% Cr. Miyoshi et al. [60] proposed equation (3.1) as a probable mechanism for Cr deposition in the oxygen electrode, which suggests that electrode polarization may play a role in the prevalence of this reaction i.e. in the fuel cell mode if the oxygen electrode is polarized cathodically, the formation of Cr_2O_3 is promoted. This may be one possible reason for lower Cr concentration at electrodes in SOEC operation mode, though a more significant factor may be the much shorter operation time.

$$2\mathrm{CrO_2(OH)_{2(g)}} + 6\mathrm{e^-} \leftrightarrow \mathrm{Cr_2O_3} + 2\mathrm{H_2O} + 3\mathrm{O^{2-}} \tag{3.1}$$

Due to the use of glass as the sealing agent, there was a potential for silicon poisoning in the hydrogen electrode. The hydrogen electrode active layer in the fragmented samples of the electrodes tested in the SOFC and SOEC mode were also analyzed for Si concentration using the ToF-SIMS method. The data was collected into Si concentration maps and are presented in Figure 18. The Si was mostly visible on the sides of electrodes, suggesting that the source of this contaminant may indeed have been the glass seal. Si concentration was much higher in the SOEC HEAL than in the SOFC HEAL. This phenomenon could be explained by the high steam concentration in the feed gas, leading to Si vaporization in the form of $Si(OH)_4$ according to Equation (3.2). For the Si poisoning in the fuel cell operation mode, Andersen et al. [61] provide a plausible mechanism, where SiO_2 becomes volatile SiO through reduction with hydrogen, in equation (3.3) and deposits on active sites through reacting with oxygen according to equation (3.4).

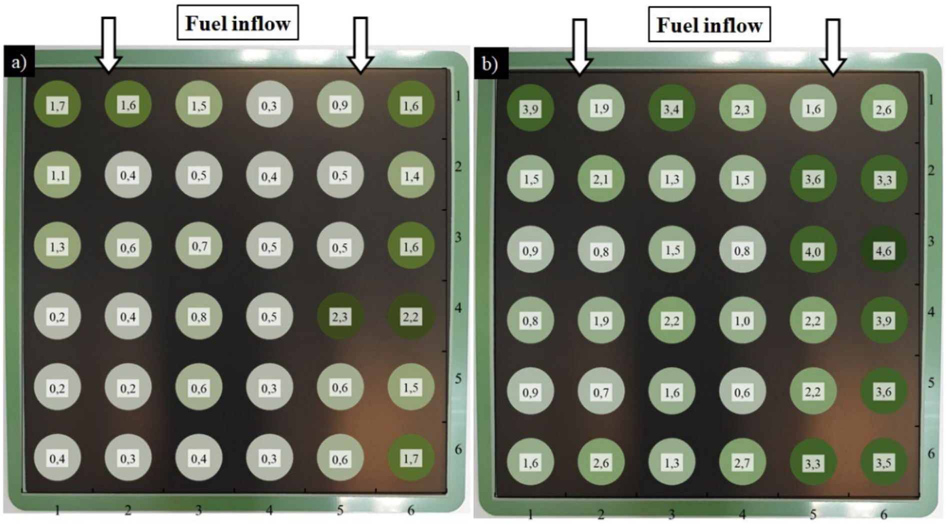

Figure 18. Si content in the Ni-YSZ layer of the fuel cell (a) and of the electrolysis cell (b). Numbers indicate the fraction of Si^+ counts from the total amount of secondary positive ions detected at the hydrogen electrode.

$$\mathrm{Si(OH)_{4(g)}} \leftrightarrow \mathrm{SiO_{2(s)}} + \mathrm{2H_2O_{(g)}} \tag{3.2}$$

$$\mathrm{H_{2(g)}} + \mathrm{SiO_{2(s)}} \leftrightarrow \mathrm{SiO_{(g)}} + \mathrm{H_2O_{(g)}} \tag{3.3}$$

$$\mathrm{SiO_{(g)}} + \frac{1}{2}\mathrm{O_{2(g)}} \leftrightarrow \mathrm{SiO_{2(s)}} \tag{3.4}$$

6.1.5 Microstructural Degradation Analysis

HR-SEM analysis of the electrolysis test SOC revealed that up to 1 μm wide microcracks had formed between the YSZ and GDC layers during electrolysis operation. Moçoteguy et al. and Knibbe et al. [10,62] suggest that at high current electrolysis conditions, oxide ion oxidation may occur within the grain boundaries of the YSZ electrolyte. The accumulating oxygen gas can form voids and create tension in the region, culminating in cracks between layers. These voids can lead to cracks in the YSZ electrolyte, delamination, or even to the total mechanical failure of the solid oxide cell. An example of the horizontal cracks found in this study can be seen in Figure 19.

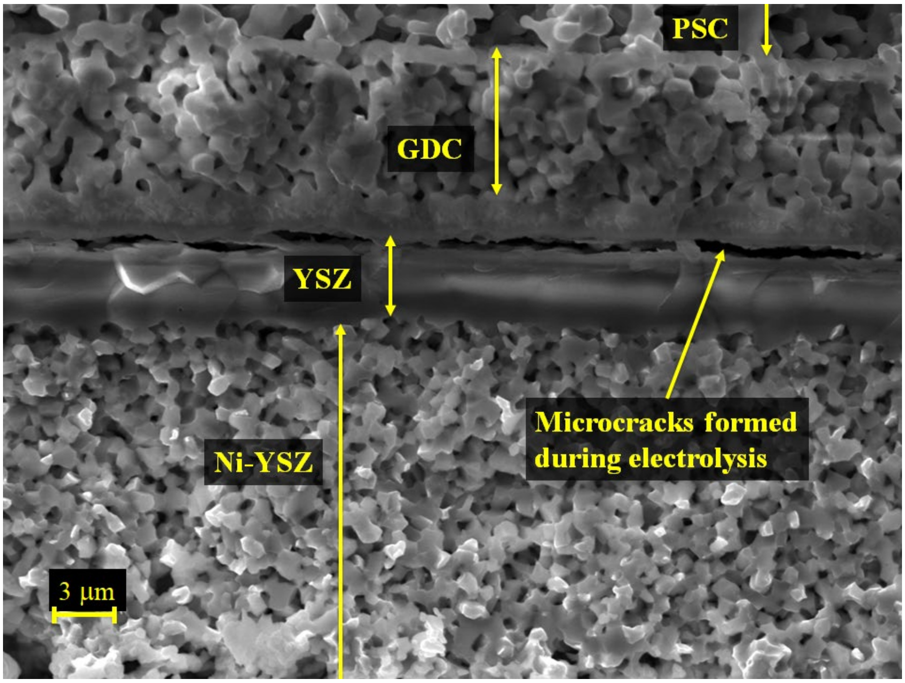

Figure 19. SEM micrograph of a cross-section of the electrolysis cell.

6.2 Influence of Hydrogen Electrode Active Layer Thickness on the Electrochemical Performance of the Solid Oxide Electrolysis Cell

6.2.1 Cyclic Voltammetry Analysis

Cyclic voltammetry data from the electrochemical tests of button type cells demonstrated that the dependence of electrolysis performance on HEAL thickness was not linear. Figure 20 shows that while having a HEAL made the SOC perform much better, the performance gain decreased severely when HEAL thickness reached 20 µm. The more steam was added to the feed gas, the greater the performance gap between the 20 µm HEAL cell and the other cells became. This suggests that the performance was limited by gas diffusion inside the HEAL.

During operation, depending on the polarization, the electrochemically active layer of the hydrogen electrode can be thinner than the physical HEAL and is located close to the electrolyte, where ohmic resistance due to ionic conductivity inside the HEAL is smallest [8]. Because the HEAL is denser and has smaller pores than the support layer, having a HEAL that is thicker than the electrochemically active area will increase concentration polarization. Thus, there is an optimal HEAL thickness that depends strongly on the operating conditions.

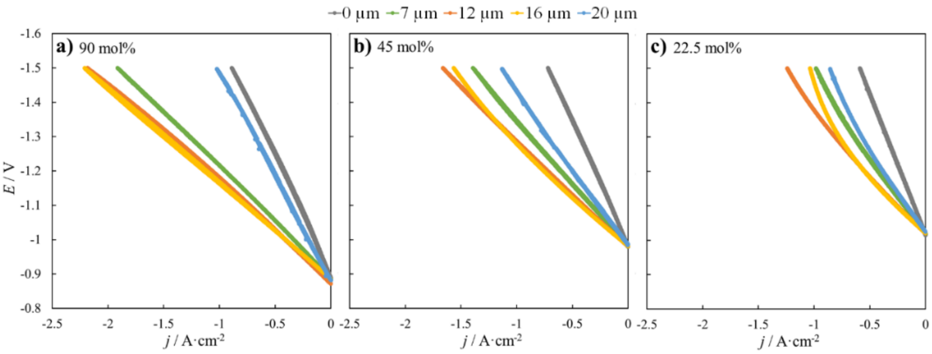

Figure 20. *j* vs *E* curves measured for experimental cells with different HEAL thicknesses at feed gas water content of 90 mol% (a) and 45 mol% (b) and 22.5 mol% (c). Temperature was 700 ˚C and active layer thicknesses are presented in figure.

The *j* vs *E* curves in Figure 21 show how the HEAL thickness affected performance change at different applied temperatures. An increase in temperature increased the ionic conductivity of the YSZ and as a result the ohmic resistance decreased. This may have increased the thickness of the electrochemically active region of the HEAL and thus improved the electrochemical performance of the thicker HEAL. This is evident in Figure 21b and 21c, where the 16 µm thick HEAL outperformed the 12 µm thick HEAL, and the performance of the cell with the 20 µm thick HEAL became much greater than that for the cell with no HEAL.

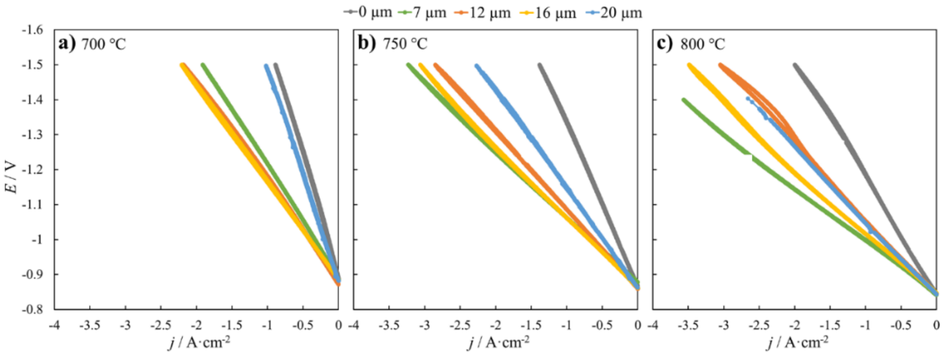

Figure 21. *j* vs *E* curves measured for the experimental cells at 700 ˚C (a), 750 °C (b) and 800 ˚C (c). Feed gas water content was 90 mol%. The HEAL thicknesses are presented in the figure.

The results in Figure 21, however, show that the increase of ionic conductivity of the YSZ material at higher temperature did not eliminate the effect of extra concentration polarization from the greater HEAL thickness. As seen in Table 4, the best performing cell in a low steam concentration environment had a HEAL thickness of 12 µm and in high steam concentration environments, the best performing cell had a HEAL thickness of 7 µm. These results suggest that the increase in operating temperature improved the water splitting reaction turnover rate enough to keep the electrochemically active HEAL region relatively thin. Thus, the best performance at 800 ˚C was achieved with the thinnest HEAL for steam concentrations of 45% and higher. The main result of this performance study was that the optimal HEAL thickness depends on the operating conditions of the tested SOC.

Table 4. Current density values at 1.45V for cells at different water content values and temperatures. Maximal current densities at certain water concentrations are marked red

Active layer thickness	Operating temperature 700 °C			750 °C			800 °C		
	Water content in feed gas, mol%								
	22.5%	45%	90%	22.5%	45%	90%	22.5%	45%	90%
	Current density, A cm^{-2}								
0 mm	0.534	0.649	0.812	0.804	1.018	1.272	1.09	1.432	1.816
7 µm	0.912	1.274	1.762	0.828	2.028	**3.008**	1.174	**2.399**	**3.825**
12 µm	**1.149**	**1.511**	2.012	**1.409**	**2.151**	2.642	**1.525**	2.289	2.797
16 µm	0.982	1.448	**2.045**	1.142	1.86	2.858	1.213	2.042	3.288
20 mm	0.811	0.848	0.936	1.105	1.614	2.109	1.316	2.119	N/A*

* The result was higher than 2.5A, which was the current limit for the potentiostat used to measure this cell.

6.2.2 Electrochemical Impedance Analysis

Figure 22 illustrates changes observed in the impedance spectra in response to changes in steam concentration in the feed gas and oxygen content in the air. Figure 22a suggests that the limiting processes, which were affected most by the steam concentration, had characteristic frequencies in the ranges of 1–50 Hz and 1–10 kHz. The literature suggests that these limiting processes could be attributed to water vapor diffusion and adsorption (1–10 Hz) and charge transfer processes at the hydrogen electrode (1–10 kHz). Figure 22a shows a decrease of low frequency impedance, when steam concentration increased from 45% to 67.5%, and a sharp increase when steam concentration increased from 67.5% to 90%. This low-frequency process had weak thermal activation and depended mostly on p_{H_2}/p_{H_2O} ratio. Königshofer et al. [30,63] noticed a similar effect, where cell impedance increased when steam concentration was increased over 80% at low current density. It has been discussed [64,65,66] that water expands the active zone or improves the conductivity of active particles.

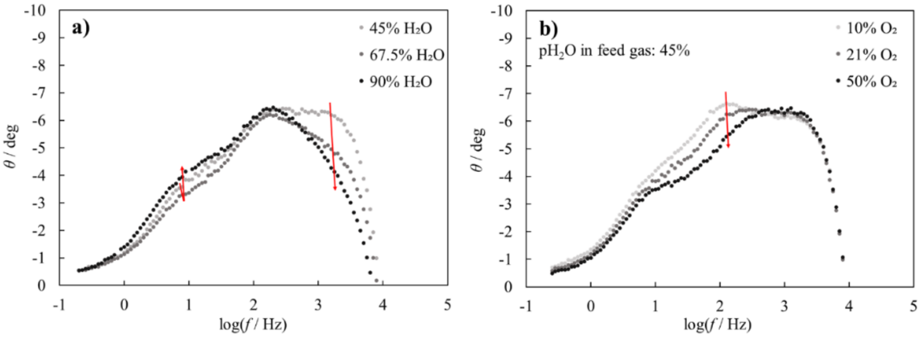

Figure 22. Bode plots recorded at different water concentrations at the hydrogen electrode (a) and at different oxygen partial pressures at the oxygen electrode (b). Temperature was 700 °C and the current density was held at -660 mA/cm^2. The HEAL was 16 μm thick.

Figure 22b shows how the cell impedance response changed with oxygen partial pressure at the oxygen electrode. It seems that the high and low frequency limiting processes were not affected by a change in p_{O_2} at the oxygen electrode, though there appeared a noticeable dependence of cell impedance on p_{O_2} in the 10–300 Hz alternating current region. According to the literature, this process could be attributed to the oxygen surface exchange processes and/or oxide ion transport processes through grain boundaries in the oxygen electrode. However, for other cells this region also featured a steam concentration dependent limiting process.

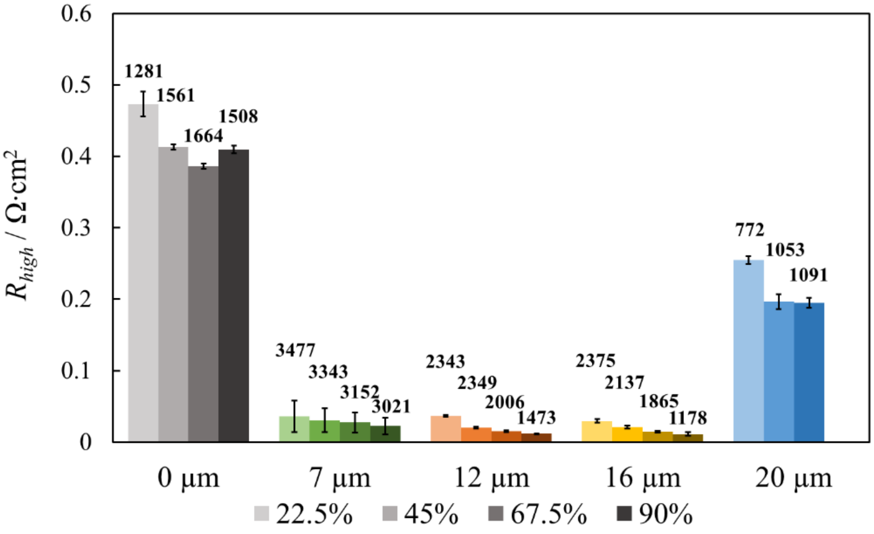

Figure 23. Impedance values of the fitted high frequency arc for each SOC at 700 °C, -330 mA/cm^2 current density and at different feed gas water content fractions (shown below the graph). The label for each value depicts the characteristic frequency of the fitted arc in hertz (Hz). Error bars represent element errors obtained during CNLS fitting. The data for the cell with the 20 µm HEAL at 700 °C and 90 mol% water content in feed gas was not usable and thus omitted from this comparison.

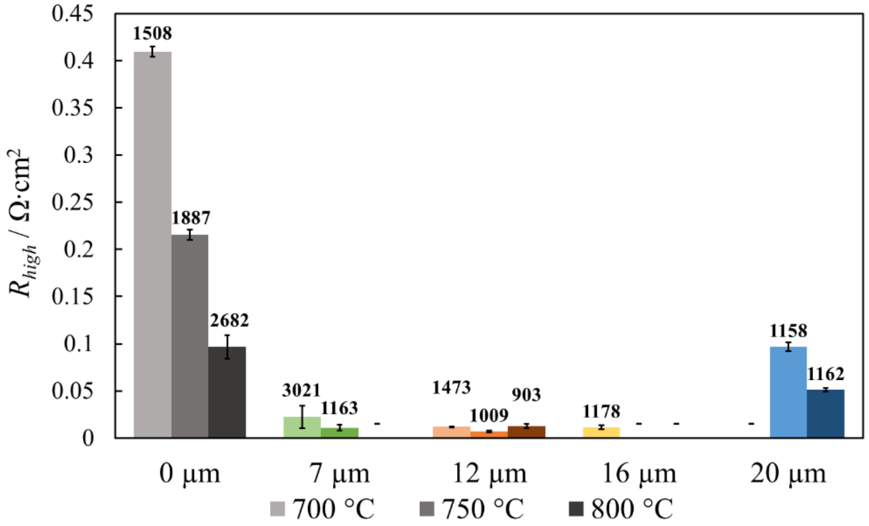

Figure 24. Calculated impedance values of the fitted high frequency arc for each SOC at 90 mol% water in feed gas, -330 mA/cm^2 current density, and at increasing operating temperature values (shown below the graph). The label for each value depicts the characteristic frequency of the fitted arc in hertz (Hz). Error bars represent fitting errors obtained during CNLS fitting.

Figure 23 visualizes the effect of feed gas (steam) concentration on the high-frequency polarization resistance R_{high} for SOC with different HEAL thicknesses. The error bar length was higher for impedance spectra, where the R_{high} and R_{mid} semi-circles were hard to separate during the fitting process. Impedance at the high frequency range was strongly affected by the thickness of the HEAL. Lowest R_{high} at 700 °C operating temperature was measured for HEAL thicknesses between 7 and 16 μm. The presence of a HEAL decreased the magnitude of the high frequency limiting process drastically by providing a high density of active reaction sites. This effect waned when the HEAL was made too thick, and the reaction sites in use were too far from the electrolyte and diffusion to the reaction sites near the electrolyte was impaired.

The high R_{high} of the SOC with no HEAL can be explained by its material composition. The HEAL was made of Ni/8YSZ, where the 8 mol% of yttria stabilized the zirconia in the cubic phase and permitted a good ionic conductivity. The support layer, meanwhile, was made from Ni/3YSZ in addition to some other microstructural changes like larger Ni particles and bigger pores as seen in Figure 3. Compared to 8 mol%, the 3 mol% yttria content in zirconia caused a partially stabilized phase, which increased the mechanical strength through structural defects but resulted in a lower oxide ion conductivity. Additionally, the coarser microstructure lead to a shorter TPB length. As a result, while the hydrogen evolution charge transfer processes were possible in the support layer, they were much more sluggish compared to the optimized HEAL.

The high-frequency process with the characteristic frequency within the 1–3 kHz range was thermally activated (with exception at 12 μm HEAL at 800 °C and 90 mol% water in feed gas, which could be explained by equivalent circuit component fitting errors). The fitting results shown in Figure 24 demonstrate that at high HEAL thicknesses (12 and 16 μm) and at high temperatures (750° to 800° C) the high frequency impedance might have almost disappeared. This fitting result may also come from the middle frequency limitation becoming dominating and overlapping in some cases, making the deconvolution of these processes challenging (high temperatures in the case of 7 μm HEAL).

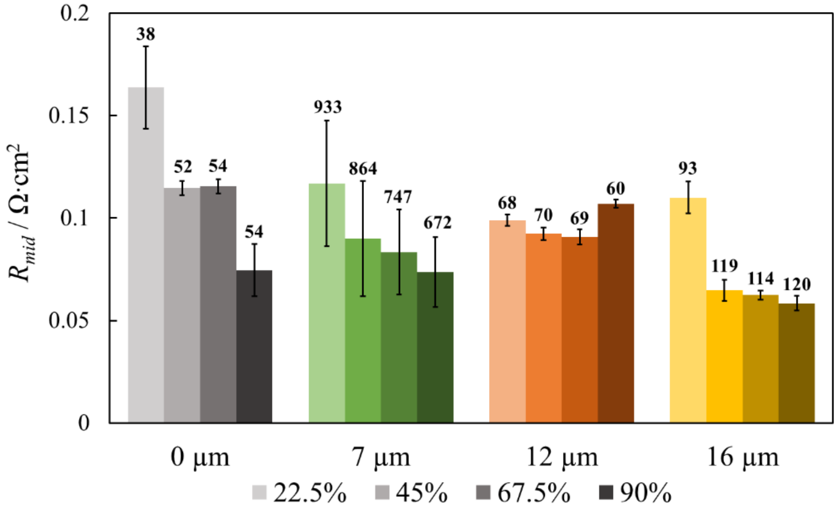

Figure 25. Impedance values of the fitted middle frequency arc for studied SOC-s at 700 °C, at -330 mA/cm^2 current density and increasing feed gas water content fractions (shown below the graph). The label for each value depicts the characteristic frequency of the fitted arc in hertz (Hz). Error bars represent element errors obtained during CNLS fitting.

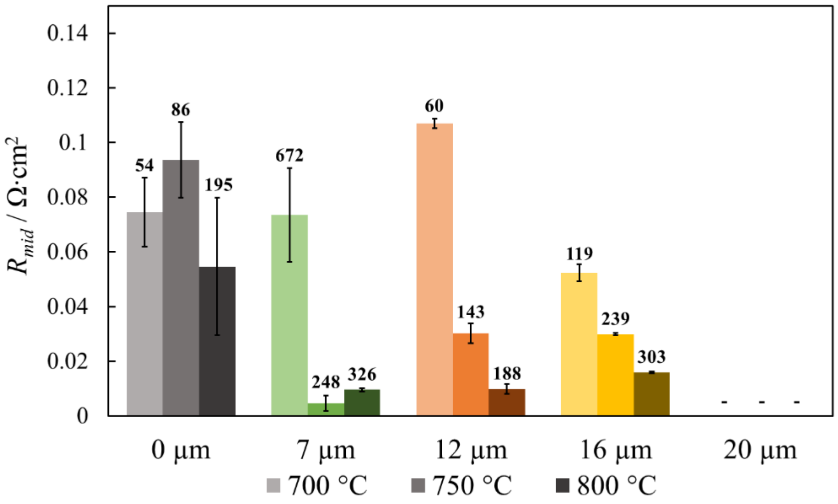

Figure 26. Calculated impedance values of the fitted middle frequency arc for each SOC at 90 mol% water in feed gas, -330 mA/cm^2 current density, and at increasing operating temperature values (shown below the graph). The label for each value depicts the characteristic frequency of the fitted arc in hertz (Hz). Error bars represent element errors obtained during CNLS fitting.

The polarization resistance values related to the mid-frequency limiting processes shown in Figure 25 are usually identified in literature as either oxygen surface exchange processes at the oxygen electrode [28,32,33] or as the gas diffusion processes at the HEAL [32,67]. Figure 22 helps to clarify the possible origin of the mid-frequency limitation by showing how the middle frequency impedance arc decreased in magnitude with the decrease of oxygen partial pressure in the oxygen electrode room and how it depended on H_2O concentration.

According to fitting results in Figure 25, the mid-frequency polarization resistance values, R_{mid}, calculated from middle frequency impedance values, showed a dependence on steam concentration in feed gas. The cell with the 20 μm HEAL did not show a distinguishable middle-frequency arc due to a highly dominant low frequency impedance. In principle, the impedance contribution of the oxygen electrode, when measured at a constant current and using a two-electrode setup, should not depend on HEAL thickness and steam concentration in the hydrogen electrode compartment. The magnitude of R_{mid} and the characteristic frequency of the mid-frequency impedance response both differed between the samples, suggesting that at least part of the impedance response, in this frequency range, was affected by HEAL properties.

Figure 25 also shows that R_{mid} of the SOC with the 7 μm HEAL had a significant dependence on steam concentration. This suggests that a HEAL thinner than 12 μm was more affected by changes in the gas diffusion process at the HEAL. The characteristic frequency of R_{mid} for the 7 μm HEAL was also significantly higher, signaling a different dominant current limiting process. Probably the mid-frequency contributions from the oxygen and hydrogen electrodes overlapped completely and the characteristic frequency was defined mainly by the process with smaller capacitance. Oxygen electrode impedance had constant value and was included in R_{mid} and the dependence of R_{mid} on steam concentration was caused by the change of polarization resistance in the hydrogen electrode. High error values of R_{mid} indicate the presence of processes with very similar time constants besides the described one.

Fitting results for EIS at varying temperature in Figure 26 suggest temperature dependence of R_{mid} values as well as characteristic time constants. The gradually changing time constants suggest that the oxygen surface exchange process at the oxygen electrode and the surface diffusion processes at the hydrogen electrode became faster. The steep change of P_{mid} characteristic frequency for the cell with the 7 μm HEAL suggests that at higher temperatures (>700 °C) the gas diffusion limitation in the HEAL lost dominance over oxygen surface exchange limitation processes at the oxygen electrode.

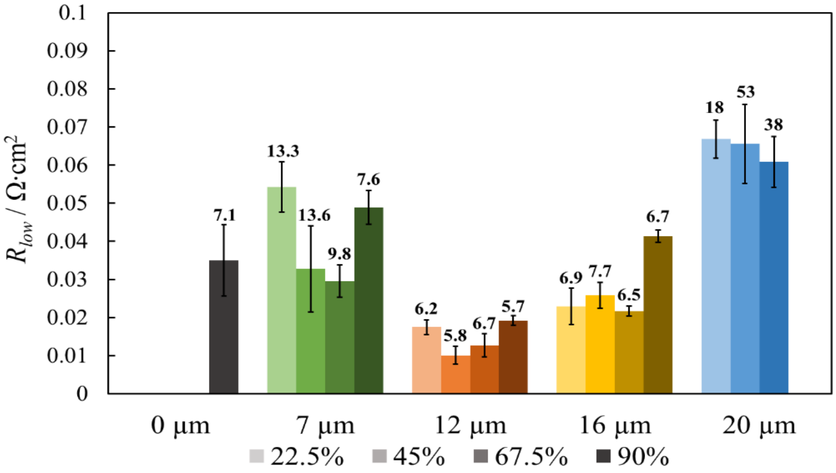

Figure 27. Impedance values of the fitted low frequency arc for each SOC at 700 °C, at -330 mA/cm^2 current density and under increasing feed gas water content fractions (Shown below the graph). The label for each value depicts the characteristic frequency of the fitted arc in hertz (Hz). Error bars represent element errors obtained during CNLS fitting. The data for the cell with the 20 µm HEAL at 700 °C and 90 mol% water content was not usable and thus omitted from this comparison.

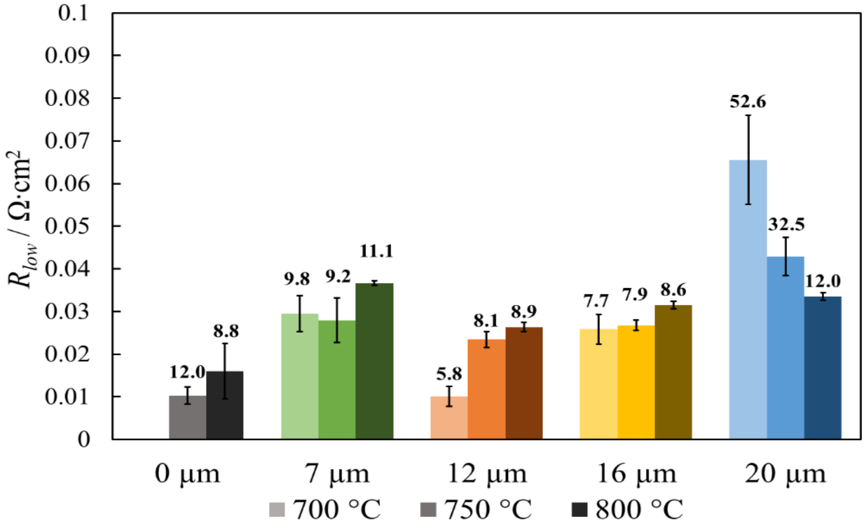

Figure 28. Impedance values of the fitted low frequency arc for each SOC at 45 mol% water in feed gas, -330 mA/cm^2 current density, and at different operating temperature values (shown below the graph). The label for each value depicts the characteristic frequency of the fitted arc in hertz (Hz). Error bars represent element errors obtained during CNLS fitting.

Low frequency polarization resistance values, R_{low}, obtained through fitting, are compared in Figures 27 and 28. The literature proposed dominant rate limiting steps in the 1–50 Hz region are either gas diffusion in the support layer [31,32,68] or H_2O adsorption/desorption in the HEAL [34,35]. The data presented here suggests no linear correlation with steam concentration and a minimum of R_{low} at around 45–67,5 mol% range, which was also illustrated in Figure 22 previously.

Figure 28 shows an increase of R_{low} with increasing temperature at 45 mol% water in feed gas, except for the cell with 20 µm thick active layer. This behavior indicates that the low frequency limiting process in the case of 7, 12 and 16 µm thick active layers was most likely H_2O adsorption as this was in good accordance with experimental results dealing with water adsorption at the YSZ [69]. Positive correlation of R_{low} with temperature in the case of 20 µm thick HEAL (Fig. 13) indicates diffusion limitation in the case of the thickest active layer. The change of R_{low} with steam concentration, where the R_{low} was at minimum around 50% H_2O concentration, also supports the concept of adsorption limitation mechanism. A change of adsorbed layer structure starting from a certain surface concentration (in the region of 50% H_2O in gas) was also demonstrated by some studies [34]. In case of the cell with the 20 µm thick HEAL, R_{low} decreased with increasing temperature due to a dominating diffusion limitation from the thick HEAL.

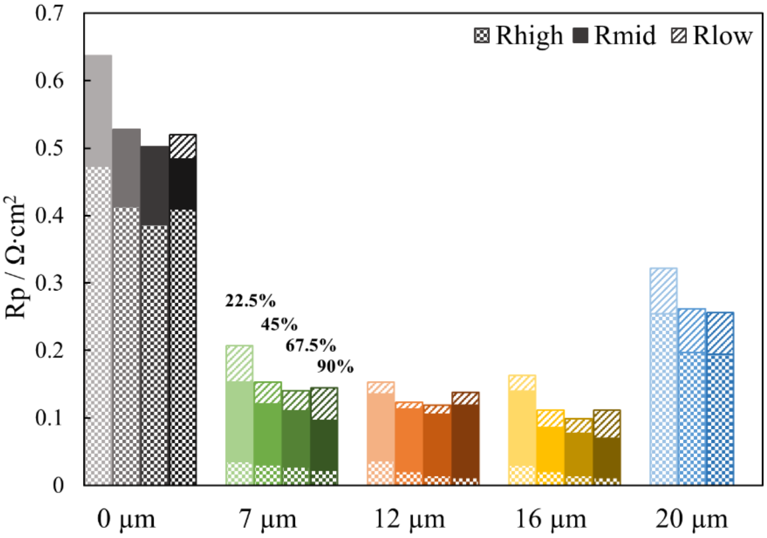

Figure 29. Polarization resistance values obtained through fitting for each SOC at 700 °C, -330 mA/cm² current density, and increasing feed gas water content fractions. The share of each dominant process in the overall polarization resistance is shown with a different filling pattern.

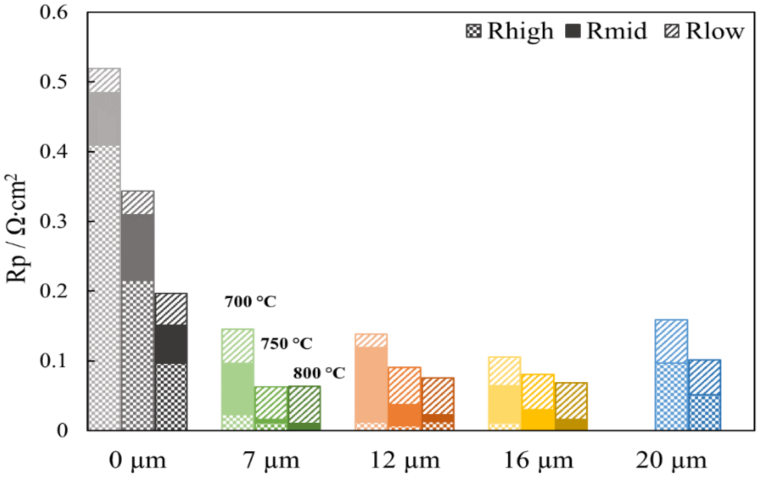

Figure 30. Polarization resistance values obtained through fitting for each SOC at 90 mol% water in feed gas, -330 mA/cm^2 current density, and increasing operating temperature values. The share of each dominant process in the overall polarization resistance is shown with a different filling pattern.

Figures 29 and 30 illustrate the total fitted polarization resistance of the studied cells with their low-, mid- and high-frequency resistance components and their change with steam concentration and with temperature, respectively. The R_p values confirm that for electrolysis conditions the optimal HEAL thickness at 700 °C, and at operating current -330 mA/cm^2, varied from 12 to 16 μm depending on steam concentration, and at higher temperatures and at 90 mol% water content the optimal HEAL thickness was 7 μm. At 700 °C, the overall polarization resistance decreased with increasing the feed gas water content up to the 67.5 mol% level, after which the sudden increase of R_{low} was enough to push the whole polarization resistance up slightly compared to the previous step. The greatest decrease in polarization resistance values occurred between 22.5 mol% and 45 mol% water content levels, which agrees with the curves in Figure 20. A similar behavior was documented by Kim et al. [70], who noted that the total charge transfer resistance of the hydrogen electrode increased significantly, when the feed gas water content was lowered below 40 mol% at 750 °C operating temperature and absolute current density reached higher than 0.5 A/cm^2. A similar phenomenon was also more recently discussed by Königshofer et al. [63].

The optimum HEAL thickness for SOC operation at 700 °C over a broad range of steam concentrations seemed to be 16 μm for the system used in this work. At higher temperatures, a thinner HEAL performed better, as demonstrated by results given in Figures 21 and 30. Limitations connected with water adsorption/ desorption in HEAL formed an important part of the total impedance, especially at higher temperatures. Performance of cells with 7, 12 and 16 μm thick HEAL at 750 °C and 800 °C could be significantly improved if limitations connected with water adsorption could be decreased.

6.3 Influence of Chemical Modifications of the Hydrogen Electrode Active Layer on the Performance of the Solid Oxide Electrolysis Cell

6.3.1 Microstructural Characterization of SOC with Chemical Codifications

Microstructural characterization of polished sample cross-sections of electrochemically tested cells was performed using the HR-SEM method. Figure 31 presents a comparison of the microstructure of the HEAL for the four tested samples. Micrographs show that some introduced modifications affected the microstructure of the HEAL slightly. Co_2O_3 and Fe_2O_3 are widely known as sintering aids for ZrO_2 [71,72]. Image analysis revealed that when compared to the reference cell, the addition of cobalt led to a nearly 27% decrease in average pore size and a 10% decrease in total porosity. The addition of GDC led to a 22% decrease in average pore size, but no significant change in total porosity. The addition of iron led to a coarser structure with around a 17% increase in average pore size, but with no significant change in total porosity.

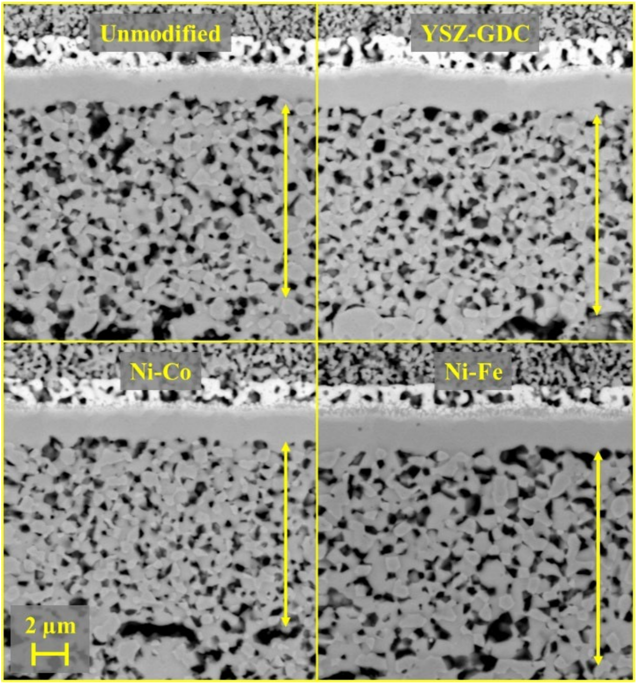

Figure 31. SEM micrographs of polished cross-sections of cells analyzed electrochemically within this work. The location of the hydrogen electrode active layer is indicated with arrows.

6.3.2 Electrochemical Characterization of SOC with Chemical Modifications

The *j* vs *E* curves at 700 °C and at different steam concentrations in feed gas, shown in Figure 32, reveal that none of the introduced materials had a positive effect on the performance of the SOEC at moderate operating temperature. Results in Figures 32 and 33 indicate that the impact of modifications depended significantly on the operating temperature and water concentration in the feed gas. Fe had a positive effect on the cell performance at 750 °C (Figure 33b), and at 800 °C, both the Fe and GDC-modified SOECs showed significantly better performance than the reference cell. However, the SOC electrodes modified with cobalt remained less active than the unmodified reference cell.

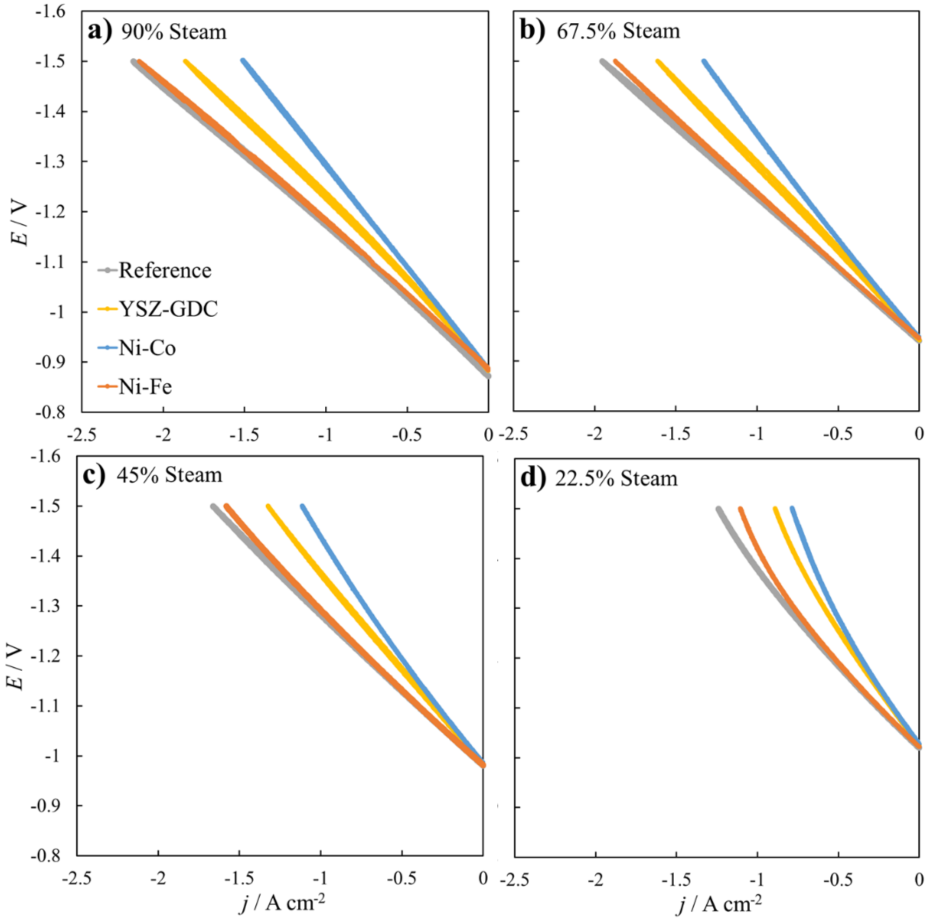

Figure 32. j-E curves of the sample cells measured at feed gas steam concentration values of 90% (a), 67.5% (b), 45% (c), and 22.5% (d).

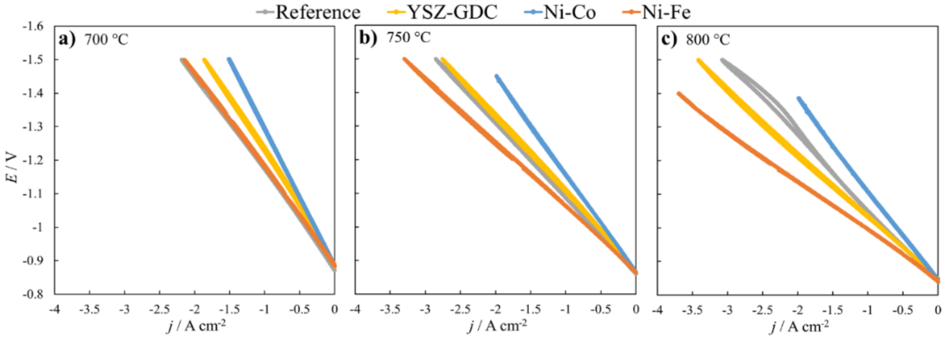

Figure 33. j-E curves of the studied cells measured at temperatures 700 °C (a), 750 °C (b), and 800 °C (c) in 90% feed gas steam concentration.

SEM results presented in Figure 31 indicate that the Ni-Fe cell had a coarser structure with an average pore size bigger than that for the reference cell, and thus Ni-Fe had shorter TPB length and less reaction sites. At 700 °C, this structural change seemed to have no notable effect as the performance of the Ni-Fe cell was similar to the reference cell aside from the performance deviation at higher voltage in Figure 32d, where the decrease in reaction sites probably became more apparent.

At higher temperatures, i.e., 750 °C and above, the Ni-Fe cell showed a remarkable increase in performance over the reference cell, probably due to a higher reactant turnover rate and lower diffusion limitation. The highest absolute current density of the Fe modified SOEC was 3.7 A/cm^2 at 800 °C, at -1.4 V, and 90% steam in feed gas, while the reference cell reached 3.1 A/cm^2 at the same conditions.

The influence of GDC on the SOEC performance depended on the temperature as well as on the concentration of water in the feed gas. As can be seen from Figures 33 and 34, the electrochemical performance of the GDC modified cell compared to the reference cell was improved at temperatures higher than 700 °C and at water concentrations higher than 45%. The increase of the YSZ-GDC cell performance at high temperature and water concentrations may have been due to enlarged electrochemically active regions close to the TPB. Monaco et al. [73] have shown that in electrolysis mode, the adsorption rate of steam on YSZ becomes very slow and the reaction pathways controlled by the steam adsorption rates on Ni are more active. The addition of GDC to YSZ could have given a mixed ionic and electronic conductive character to the HEAL and thus widened the active area for the charge transfer process.

The nonlinear shape of *j* vs *E* curves at moderate temperatures (700 °C) and low water concentrations (22.5% and 45%) indicate that partial diffusional limitation of water in the porous electrode was possible [21].

To improve our understanding on the role of dopants in electrochemical performance, the systems of interest were systematically characterized using EIS, and the obtained experimental spectra were analyzed using the CNLS fitting method.

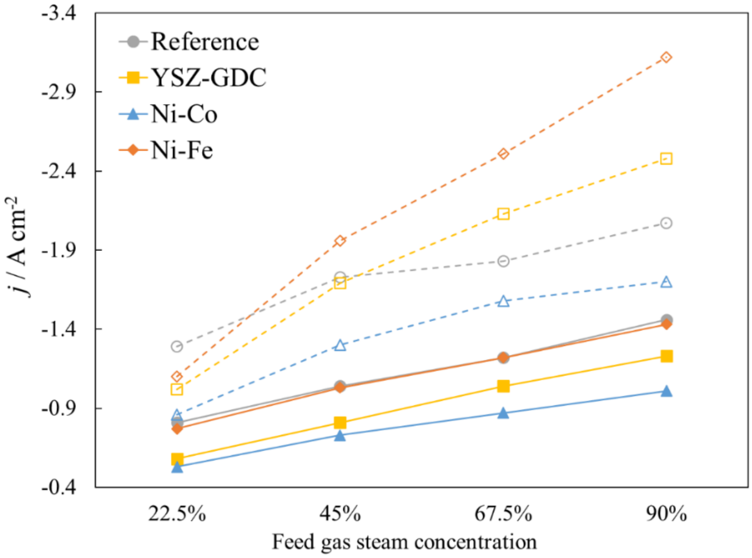

Figure 34. Current density of the SOECs at -1.3 V cell voltage, measured at different steam concentration levels and temperatures. The data measured at 800 °C is represented by unfilled points, and the data at 700 °C is represented by filled points.

6.3.3 Electrochemical Impedance Analysis of SOC with Chemical Modifications

According to the results of electrochemical characterization, the modifications of the HEAL could influence all three proposed processes. However, as can be seen in Figures 35, 36 and 37, the most significant changes to the cell impedance (at 700 °C) caused by modifications in HEAL composition, occurred in the mid- and high-frequency range. Figures 36 and 39 indicate that at 800 °C, the impact of R_{mid} on the total impedance decreased, and the greatest impedance changes caused by modifications to HEAL composition appeared mainly at the high-frequency polarization region.

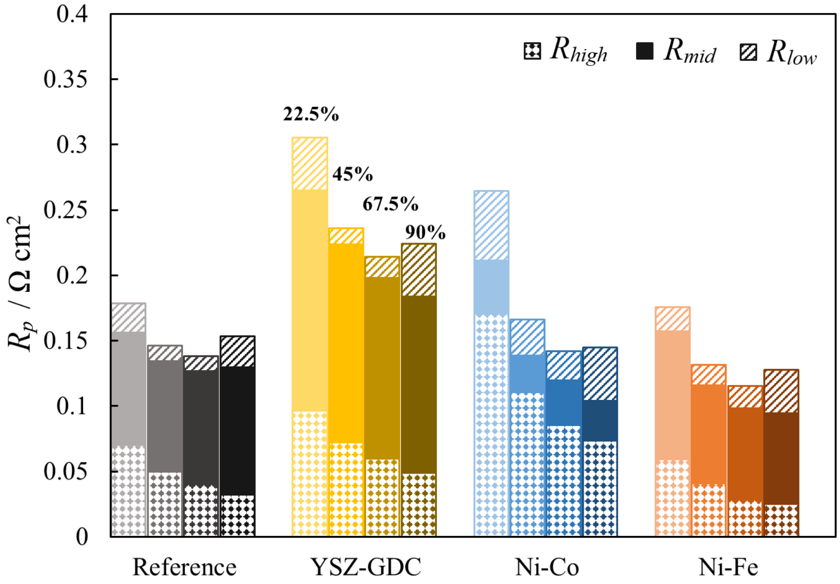

Figure 35. Stacked bar chart depicting the polarization resistance and the contribution of its components for each sample cell. Measured at 700 °C temperature, at -330 mA/cm^2 current density and at different feed gas steam concentration, as shown on the YSZ-GDC results.

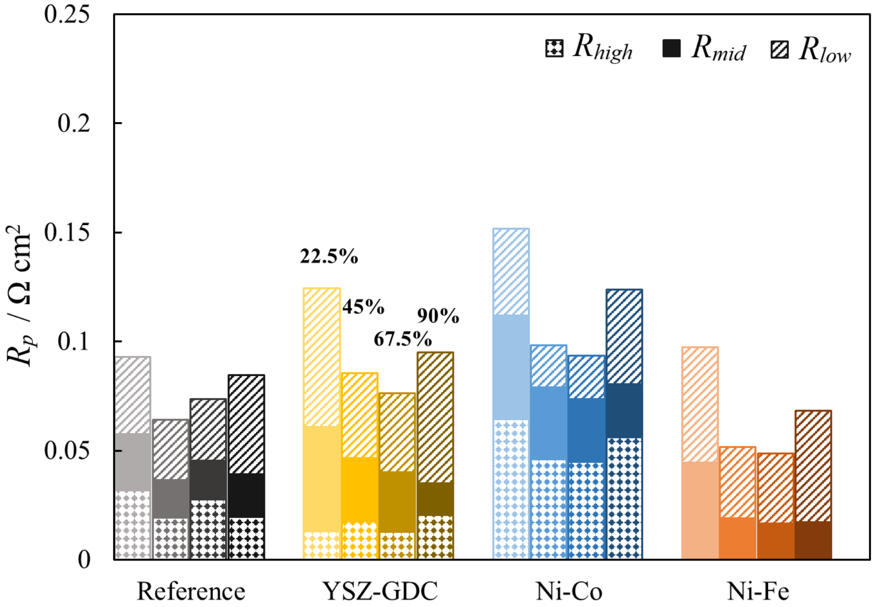

Figure 36. Stacked bar chart depicting the polarization resistance and the contribution of its components for each sample cell. Measured at 800 °C temperature, at -330 mA/cm^2 current density and at different feed gas steam concentration, as shown on the YSZ-GDC results.

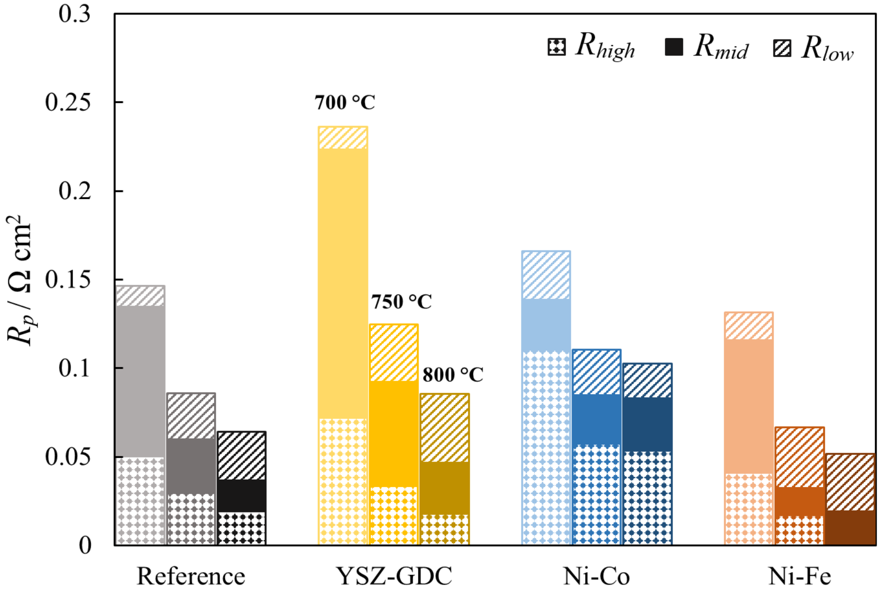

Figure 37. Stacked bar chart depicting the polarization resistance and the contribution of its components for each studied cell. Measured at feed gas steam concentration of 45%, at -330 mA/cm^2 current density and at different operating temperatures, as shown on the YSZ-GDC results.

As demonstrated in Figure 35, at 700 °C the R_{high} decreased with the increase of water concentration in the gas stream, which has also been demonstrated by Caliandro et al. [12]. At higher temperatures, around 800 °C, the dependence of R_{high} on the water concentration decreased substantially. It could be explained by a sufficiently high speed of mass transport to saturate the active centers and thus R_{high}, attributed to the charge transfer resistance, started to depend mainly on the chemical nature and number of active sites in the catalyst. At 700 °C, the lowest R_{high} values were calculated for Ni-Fe, followed by the reference sample, YSZ-GDC and Ni-Co (Fig. 5–8). With the increase of temperature from 700 °C to 800 °C, the order of electrodes ranked by R_{high} changes. The R_{high} of YSZ-GDC became smaller than that for the reference sample probably due to the increase of the active region in YSZ-GDC electrode when the GDC was reduced more thoroughly with the increase of temperature.

At 700 °C, the mid-frequency process P_{mid} changed little with increasing the steam content, suggesting that R_{mid} was not influenced by steam concentration in feed gas. With increasing temperature, the nature of P_{mid} changed. At 800 °C, R_{mid} decreased with increasing steam concentration as shown in Figure 36. The characteristic frequency of the mid-frequency process increased with increasing temperature. This alludes to the presence of two processes in the 10–1000 Hz range, one in the range of 50–80 Hz (P_{mid_1}) and another in the range of 100–300 Hz (P_{mid_2}). P_{mid_1} seemed to depend more on temperature, and if temperature was increased, it became less limiting than P_{mid_2}, while P_{mid_2} became the limiting process at temperatures above 750 °C.

At 700 °C, R_{mid_1} depended significantly on the chemical composition of the electrode as shown in Figure 35. These differences of R_{mid_1} were so high that they cannot be attributed to the changes of porosity of the materials studied in this work. Therefore, P_{mid_1} was most likely related to differences in surface diffusion caused by the chemical composition changes in the HEAL. At 800 °C, where P_{mid_2} characterized the limiting process, there was a notable but not very high influence of the steam concentration on process activity. A jump of decreasing R_{mid_2} could be seen when steam concentration increased from 22.5% to 45%. This effect was a feature of the HEAL, but there is no good agreement in discussions of the nature of this process in the literature.

The R_{low} values followed a very similar trend for all modified and reference SOCs in all steam concentrations. The low-frequency process had weak thermal activation and depended mostly on the p_{H_2}/p_{H_2O} ratio. The low frequency polarization resistance decreased when steam concentration increased from 22.5% to 45% and increased sharply when steam concentration increased from 67.5% to 90%. Königshofer et al. [30,63] noticed a similar effect, where cell impedance increased when steam concentration was increased over 80% at low current density. It has been discussed [64,65,66] that water expands the active zone or improves the conductivity of the catalytically active particles.

Particularly in the case of the Ni-Co electrode (Figure 36) and slightly in the other electrodes (Figure 35), a relationship between R_{high}, attributed to the charge transfer, and R_{low}, attributed to the adsorption of water or the capacitance of the adsorbed layer, could be seen. It appears that an increase of R_{low} at high and low water concentrations led to a slight increase of R_{high}. Comparison of R_{low} values for different electrode materials studied in this work revealed that there was no significant dependence of R_{low} on the chemical composition of electrodes except for the Ni-Co sample, which showed slightly higher R_{low} values. This behavior further supports the interpretation that most likely this R_{low} described the formation of the adsorbed layer at the YSZ as has been proposed by Primdahl et al. [34]. In the case of Ni-Co, the YSZ could be just modified to a greater extent, leading to slightly higher R_{low} values. Detailed analysis of this effect, however, is not in the scope of this study.

Figure 38 highlights that at 700 °C the low performance of YSZ-GDC was due to larger R_{mid} as well as larger R_{high} values. The microstructure of the YSZ-GDC cell in Figure 31 does not reveal a significant structural difference from the reference cell. Therefore, the changes in electrochemical performance were likely related to the chemical composition of the electrodes under study. Due to the possibility of forming mixed phases between GDC and 8YSZ at temperatures above 1200 °C [74] during cell manufacturing, the surface of the YSZ may have been partially modified to inhibit surface diffusion of active particles and to decrease O^{2-} ion conductivity at the YSZ|GDC interface [75]. This would have inhibited charge transfer processes, thus increasing R_{high} and R_{mid}. This effect, however, seemed to be mitigated at 800 °C and the benefit of mixed conductivity of GDC increased charge transfer activity, according to data in Figures 37 and 39.

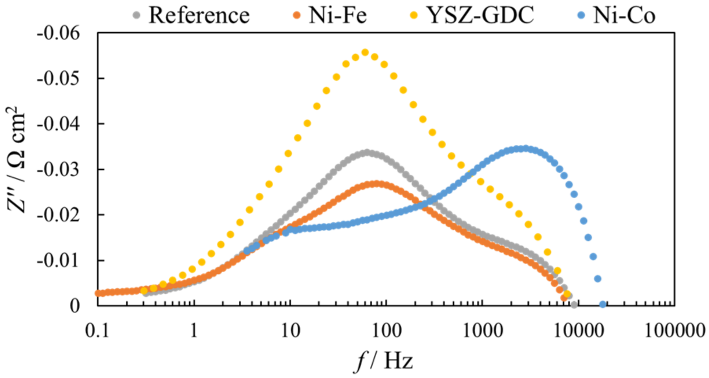

Figure 38. EIS spectra in Bode plots. Comparison of the results for different cells. Measured at 700 °C, -330 mA cm^{-2} current density and 67.5% feed gas steam concentration.

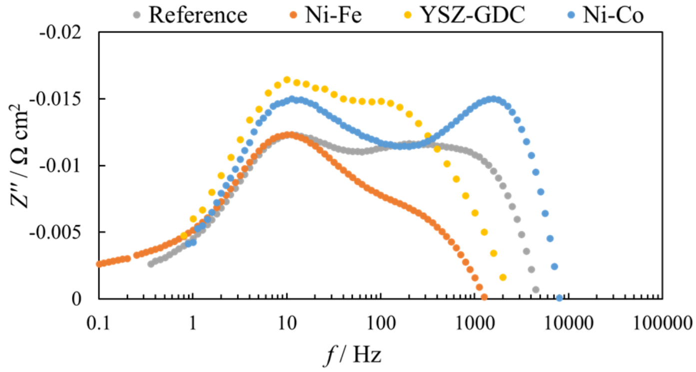

Figure 39. EIS spectra in Bode plots. Comparison of the results for different cells. Measured at 800 °C, -330 mA cm^{-2} current density and 67.5% feed gas steam concentration.

Figure 38 suggests that the slightly smaller particle and pore sizes for the Ni-Co cell (Figure 31) did not interfere with reactant diffusion at low current density (330 mA/cm^2) and that it possibly even enhanced the surface diffusion of reactants in the HEAL. The impedance data also shows that the addition of cobalt into the catalyst decreased the charge transfer activity. There are multiple reasons that may lead to an unfavorable TPB structure when cobalt is added to the Ni-YSZ material, such as the decrease of the oxide ion conductivity of YSZ at certain Co concentrations [76] or structural changes from oxidation, thermal treatment and reduction of the Ni-Co system.

The performance gain of Ni-Fe at low current density was caused by a decrease in R_{high}. At lower temperature, the addition of Fe possibly enhanced the HEAL structure and reactant transport conditions inside the HEAL. At higher temperatures, the addition of Fe increased the cell charge transfer activity, faradaic activity, and possibly surface diffusion rate as shown in Figure 37.

At 800 °C, the charge transfer processes in the Fe promoted cell became fast enough so that limiting processes in the high-frequency range did not show up in the measured impedance spectra, as seen in Figure 40, and in fitted parameter values in Figures 36 and 37. This “disappearance” may have been caused by increasing the reaction turnover rate due to the higher proposed activity of Fe or Ni_3Fe species [43] in the Ni-Fe electrode. This increase in reaction turnover rate could have diminished the impedance of P_{high} enough to be overshadowed by the inductive effect of the measurement set-up in the impedance spectra or to become indistinguishable from the P_{mid} process.

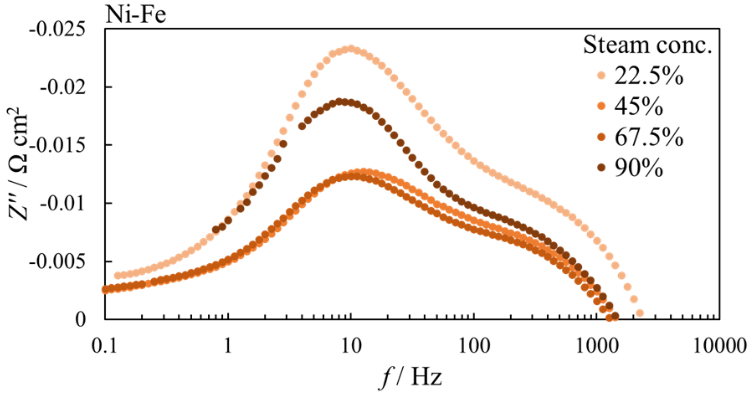

Figure 40. EIS spectra in Bode plots measured of the SOC with added Fe in the HEAL at 800 °C, -330 mA/cm² current density and different feed gas steam concentrations.

7. SUMMARY

The aim of this work was to investigate degradation mechanisms of materials in a state-of-the-art SOC after operating in both fuel cell and electrolysis modes and to improve electrolysis performance of the SOC with small modifications. State-of-the-art commercial solid oxide cell components were used to achieve comparable results, which would also be interesting for industrial applications. Testing of SOC stability was done using 50×50 mm cells between steel current collectors to characterize the structural changes over the SOC area in an environment similar to a SOC stack. Detailed electrochemical characterization was done on small 20 mm diameter button type cells, which were fully manufactured in industrial conditions and modes. These button cell studies focused on the performance characteristics of the SOC in electrolysis mode and the role of the hydrogen electrode active layer (HEAL) characteristics in the system. Small changes in the microstructure and chemical composition of the HEAL were introduced during the manufacturing processes of electrodes to characterize the effect of these changes to the electrolysis performance of the SOC.

The first part of this work describes how SOC devices with commercial half-cells and in-house developed oxygen electrodes were characterized in long-term electrochemical tests. One cell was run in fuel cell mode at 650 °C for 17820 h, while another was run in electrolysis mode at 800 °C for 860 h. The fuel cell test data showed a change in degradation behavior after 9000 hours, with a 2.4%/1000 h degradation rate in the first and 1.1%/1000 h in the latter time period. The electrolysis test degradation rate was around 16.3%/1000 h, but it regenerated to some extent after every time operation was stopped for impedance measurement.

The degraded cells were then characterized using the ToF-SIMS method to detect the concentration of ^{18}O species in the oxygen electrode, which were shortly introduced at the end of the time-stability tests. The data were used to create an activity map and correlate this to Ni grain growth over time. ToF-SIMS was also used to detect Cr species in the oxygen electrode and Si species in the hydrogen electrode. Cr concentration maps did not correlate with the activity maps, and Si concentration maps suggested that sealing glass may have been a possible poisoning source. Si deposition on the active sites in the hydrogen electrode was possibly a major part of the SOC performance degradation in both operating modes.

Lastly, SEM characterization data of the used long-term tested electrolysis cells showed the presence of significant cracks between the GDC and YSZ layers. These cracks were probably created by oxide ion oxidation near the GDC and YSZ boundary, creating gaseous O_2 within the YSZ grain boundaries and pushing the layers apart. This mechanism was probably a major reason why the SOC degraded much more quickly in the electrolysis mode than in the fuel cell mode.

In the second part of this work, the state-of-the-art commercial SOC HEAL structure was modified to investigate its role in the electrochemical performance of the cell in electrolysis mode. The SOCs were manufactured with HEALs of different thicknesses, and the resulting cells were characterized using SEM and electrochemical methods. Experimental cell performances were compared at different temperatures and feed gas compositions using cyclic voltammetry data. Impedance spectra of the experimental cells were analyzed at different feed gas (steam) concentration levels using equivalent circuit models and fitting the calculated data using the CNLS analysis method.

EIS analysis revealed that the greatest changes to the impedance of the SOC induced by increasing the HEAL thickness were observed for characteristic frequencies in regions from 1 to 10 Hz and from 1 to 10 kHz, i.e., in two separate ac frequency regions.

The results collected in this work led to the conclusion that: i) the inclusion of a HEAL in the SOEC structure dramatically increased the performance of the electrolysis cell and ii) the optimal HEAL thickness for a SOEC was dictated by the operating conditions applied for the electrolysis mode.

For operating in the electrolysis mode at 700 °C, the SOEC with the 16 μm thick HEAL seemed to be optimal due to longer TPB length, while the cell with the 12 μm thick HEAL was close due to better diffusion properties. At higher temperatures, however, the low frequency impedance processes became reaction rate limiting at high current density and therefore the SOEC with the 7 μm thick HEAL proved to be the optimal construction. The highest current density, -3.57 A/cm^2 at -1.4 V at 800 °C, was recorded for the cell containing the 7 μm thick HEAL. A very promising approach to improve the electrolysis performance of cells with optimal HEAL thickness seems to be decreasing limitations connected with the adsorption process of water in the HEAL.

In the third part of this work, solid oxide cells with HEALs modified with Fe, Co, and GDC were produced in cooperation with an industrial partner and characterized in detail. These cells were characterized using HR-SEM and electrochemical analysis methods, such as CV and EIS. When compared to the reference SOC, the modified cells showed significant differences in electrolysis performance and in performance dependence on temperature and steam concentration in feed gas.

The chemical modifications in the HEAL mainly caused changes to charge transfer activity and reactant transport processes. Changes to gas diffusion from microstructural differences became significant only at high current density. In comparison to the reference cell, both reactant transport and charge transfer processes were inhibited with the addition of GDC at low temperature, while charge transfer processes were more active at high temperature. Modification with Co inhibited charge transfer processes significantly, though at low temperature, the reactant transport was enhanced. Modifying the HEAL with Fe enhanced reactant transport processes at 700 °C, while at 800 °C, the speed of charge transfer processes was also significantly improved. Overall, the best performance was achieved with SOC enhanced with Fe, reaching a current density of -3.7 A/cm^2 when measured at -1.4 V, 800 °C operating temperature and 90% steam concentration.

8. REFERENCES

[1] M. Wappler, D. Unguder, X. Lu, H. Ohlmeyer, H. Teschke, W. Luebke, *Int. J. Hydrog. Energy* **47** (2022) 33551.

[2] IEA, Iron and Steel Technology Roadmap (2020) IEA, Paris, https://www.iea.org/reports/iron-and-steel-technology-roadmap

[3] IEA, Emissions Measurement and Data Collection for a Net Zero Steel Industry (2023) IEA, Paris, https://www.iea.org/reports/emissions-measurement-and-data-collection-for-a-net-zero-steel-industry

[4] J. Sekhar S., A. S. A. Al-Shahri, G. Glivin, T. H. T. Le, T. Mathimani, *Fuel* **358** (2024) 130307. https://doi.org/10.1016/j.ijhydene.2023.06.058

[5] M. B. Ledari, H. Khajehpour, H. Akbarnavasi, S. Edalati, *Int. J. Hydrog. Energy* **48** (2023) 36623.

[6] Y. Haseli, *Int. J. Hydrog. Energy* **43** (2018) 9015–9021. https://doi.org/10.1016/j.ijhydene.2018.03.076

[7] M. Lang, S. Raab, M. S. Lemcke, C. Bohn, M. Pysik, *Fuel Cells*, **20** (2020) 690–700. https://doi.org/10.1002/fuce.201900245

[8] M. B. Mogensen, M. Chen, H.L. Frandsen, C. Graves, J.B. Hansen, K.V. Hansen, A. Hauch, T. Jacobsen, S.H. Jensen, T.L. Skafte, and X. Sun, *Clean Energy*, **3** (2019) 175–201. https://doi.org/10.1093/ce/zkz023

[9] Giulio Vialetto, Marco Noro, Paolo Colbertaldo, and Masoud Rokni, *Int. J. Hydrog. Energy* **44** (2019) 9608–9620. https://doi.org/10.1016/j.ijhydene.2018.08.145

[10] P. Mocoteguy, A. Brisse, *Int. J. Hydrogen Energy* **38** (2013) 15887–15902. https://doi.org/10.1016/j.ijhydene.2013.09.045

[11] Tao, Y.K.; Ebbesen, S.D.; Mogensen, M.B. Degradation of solid oxide cells during co-electrolysis of steam and carbon dioxide at high current densities, *J. Power Sources* **328** (2016) 452–462. https://doi.org/10.1016/j.jpowsour.2016.08.055

[12] P. Caliandro, A. Nakajo, S. Diethelm, J. Van Herle, *J. Power Sources* **436** (2019) 226838. https://doi.org/10.1016/j.jpowsour.2019.226838

[13] H. Sumi, H. Shimada, Y. Yamaguchi, T. Yamaguchi, Y. Fujishiro, *Electrochim. Acta* **339** (2020) 135913. https://doi.org/10.1016/j.electacta.2020.135913

[14] D. Papurello, D. Menichini, A. Lanzini, *Electrochim. Acta* **258** (2017) 98–109. https://doi.org/10.1016/j.electacta.2017.10.052

[15] X. Chen, J. Lin, L. Sun, T. Liu, J. Wu, Z. Sheng, Y. Wang, *Electrochim. Acta* **298** (2019) 112–120. https://doi.org/10.1016/j.electacta.2018.12.078

[16] M. B. Mogensen *Thermodynamics of high temperature H_2O and CO_2 electrolysis* (2020). https://figshare.com/articles/online_resource/Thermodynamics_of_high_temperature_H2O_and_CO2_electrolysis/12652322

[17] P. Atkins, J. de Paula, J. Keeler, *Atkins' Physical Chemistry*, 12th ed. (2023) Oxford University Press.

[18] K. Noori, B. A. Olsen, A. Rodin, *Phys. Rev. Res.* **6** (2024) 023322. https://doi.org/10.1103/PhysRevResearch.6.023322

[19] T. Famprikis, P. Canepa, J. A. Dawson, M. S. Islam, C. Masquelier, *Nat. Mater.* **18** (2019) 1278–1291. https://doi.org/10.1038/s41563-019-0431-3

[20] S. C. Singhal, K. Kendal, *High Temperature Solid Oxide Fuel Cells: Fundamentals, Design, and Applications* (2003) Elsevier B.V.

[21] N. Q. Minh, T. Takahashi, *Science and Technology of Ceramic Fuel Cells* (1995) Elsevier Science B.V.

[22] W. Sitte, R. Merkle, *High-Temperature Electrolysis: From Fundamentals to Application* (2023) IOP Publishing.

[23] A. Ch. Lazanas, M. I. Prodromidis, *ACS Meas. Sci. Au*, **3** (2023) 162–193. https://doi.org/10.1021/acsmeasuresciau.2c00070

[24] E. Barsoukov, J. R. Macdonald, *Impedance Spectroscopy: Theory, Experiment, and Applications, 2nd ed.* (2005) Wiley-Interscience.

[25] T. Pajkossy, *J. Electroanal. Chem.* **364** (1994) 111–125. https://doi.org/10.1016/0022-0728(93)02949-I

[26] J.-B. Jorcin, M. E. Orazem, N. Pebere, B. Tribollet, *Electrochim. Acta* **51** (2006) 1473-1479. https://doi.org/10.1016/j.electacta.2005.02.128

[27] A. Leonide, Y. Apel, E. Ivers-Tiffée, *ECS Trans.* **19** (2009) 81. https://doi.org/10.1149/1.3247567

[28] P. Hjalmarsson, X. F. Sun, Y. L. Liu, M. Chen, *J. Power Sources* **262** (2014) 316–322. https://doi.org/10.1016/j.jpowsour.2014.03.133

[29] S. Dierickx, T. Mundloch, A. Weber, E. Ivers-Tiffée, *J. Power Sources* **415** (2019) 69-82. https://doi.org/10.1016/j.jpowsour.2019.01.043

[30] B. Königshofer, M. Höber, N. H. Menzler, H. Schröttner, C. Hochenauer, V. Subotić, *Int. J. Hydrog. Energy* **48** (2023) 3740. https://doi.org/10.1016/j.ijhydene.2022.10.265

[31] Q. Fang, L. Blum, and N. H. Menzler, *J. Electrochem. Soc.* **162** (2015) F907–F912. https://doi.org/10.1149/2.0941508jes

[32] Y. Yang, X. Tong, A. Hauch, X. Sun, Z. Yang, S. Peng, M. Chen, *Chem. Eng. J.* **417** (2021) 129260 https://doi.org/10.1016/j.cej.2021.129260

[33] M. Rao, S. H. Jensen, X. Sun, A. Hagen, *Fuel Cells*, **19**, (2019) 445–457 https://doi.org/10.1002/fuce.201800166

[34] S. Primdahl, M. Mogensen, *J. Electrochem. Soc.* **144** (1997) 3409. https://doi.org/10.1149/1.1838026

[35] W. Pan, K. Chen, N. Ai, Z. Lü, S. P. Jiang, *J. Electrochem. Soc.* **163** (2016) F106–F114. https://doi.org/10.1149/2.0801602jes

[36] J. Vickerman, D. Briggs, *ToF-SIMS: Materials Analysis by Mass Spectrometry 2nd Ed.* (2013) IM Publications and Surface Spectra Limited.

[37] W. Nernst, *Z. Electrochem.* **6** (1899) 41.

[38] A. Hauch, R. Küngas, P. Blennow, A. B. Hansen, J. B. Hansen, B. V. Mathiesen, M. B. Mogensen, *Science* **370** (2020) eaba6118. https://doi.org/10.1126/science.aba6118

[39] H. Inaba, H. Tagawa, *Solid State Ion.* **83** (1996) 1–16. https://doi.org/10.1016/0167-2738(95)00229-4

[40] H. Yokokawa, *Annu. Rev. Mater. Res.* **33** (2003) 581–610. https://doi.org/10.1146/annurev.matsci.33.022802.093856

[41] M. A. Laguna-Bercero, *J. Power Sources* **203** (2012) 4–16. https://doi.org/10.1016/j.jpowsour.2011.12.019

[42] M. M. Murphy, J. Van Herle, A. J. McEvoy, K. Ravindranathan Thampi, *J. Electrochem. Soc.* **141** (1994) L94. https://doi.org/10.1149/1.2055107

[43] A. Cho, J. Ko, B. K. Kim, J. W. Han, *ACS Catal.* **9** (2019) 967. https://doi.org/10.1021/acscatal.8b02679

[44] X. K. Gu, E. Nikolla, *J. Phys. Chem. C* **119** (2015) 26980. https://doi.org/10.1021/acs.jpcc.5b07814

[45] Y. Ishibashi, K. Matsumoto, S. Futamura, Y. Tachikawa, J. Matsuda, S. M. Lyth, Y. Shiratori, S. Taniguchi, K. Sasaki, *J. Electrochem. Soc.* **167** (2020) 124517. https://doi.org/10.1149/1945-7111/abac87

[46] T. Ishihara, N. Jirathiwathanakul, H. Zhong, *Energy Environ. Sci.* **3** (2010) 665. https://doi.org/10.1039/B915927D

[47] T. Ishihara, H. Zhong, *Scripta Materialia* **65** (2011) 108. https://doi.org/10.1016/j.scriptamat.2010.08.022

[48] R. Nishida, P. Puengjinda, H. Nishino, K. Kakinuma, M. E. Brito, M. Watanabe, H. Uchida, *RSC Adv.* **4** (2014) 16260. https://doi.org/10.1039/C3RA47089J

[49] K. Matsumoto, Y. Tachikawa, S. M. Lyth, J. Matsuda, K. Sasaki, *Int. J. Hydrog. Energy* **47** (2022) 29441. https://doi.org/10.1016/j.ijhydene.2022.06.268

[50] P. Blaszczak, M. Zając, A. Ducka, K. Matlak, B. Wolanin, S. F. Wang, A. Mandziak, B. Bochentyn, P. Jasiński, *J. Hydrog. Energy* **47** (2022) 35017. https://doi.org/10.1016/j.ijhydene.2022.08.057

[51] W. C. Chueh, Y. Hao, W. C. Jung, S. M. Haile, *Nature Materials* **11** (2012) 155. https://doi.org/10.1038/nmat3184

[52] A. Nenning, C. Bischof, J. Fleig, M. Bram, A. K. Opitz, *Energies* **13** (2020) 987. https://doi.org/10.3390/en13040987

[53] J. Grimes, J. Hong, S. A. Barnett, *J. Power Sources* **551** (2022) 232189. https://doi.org/10.1016/j.jpowsour.2022.232189

[54] E. Lust, R. Küngas, I. Kivi, H. Kurig, P. Möller, E. Andreson, K. Lust, K. Tamm, A. Samussenko, G. Nurk, *Electrochim. Acta* **55** (2010) 7669–7678. https://doi.org/10.1016/j.electacta.2009.11.007

[55] H.-T. Lim, S. C. Hwang, Y. M. Park, I. S. Lee, *Solid State Ion.* **225** (2012) 124–130. https://doi.org/10.1016/j.ssi.2012.03.023

[56] L. Blum, U. Packbier, I. C. Vinke, L. G. J. de Haart, *Fuel Cells* **13** (2013) 646–653. https://doi.org/10.1002/fuce.201200151

[57] P. Hjalmarsson, X. Sun, Y. L. Liu, M. Chen, *J. Power Sources* **223** (2013) 349–357. https://doi.org/10.1016/j.jpowsour.2012.08.063

[58] M. S. Khan, W. Wahyudi, S. B. Lee, R. H. Song, J.W. Lee, T. H. Lim, S. J. Park, *Int. J. Hydrogen Energy* **40** (2015) 11968–11975. https://doi.org/10.1016/j.ijhydene.2015.04.145

[59] M. S. Khan, S. B. Lee, R. H. Song, J. W. Lee, T. H. Lim, S. J. Park, *Ceram. Int.* **42** (2016) 35–48. https://doi.org/10.1016/j.ceramint.2015.09.006

[60] K. Miyoshi, H. Iwai, M. Kishimoto, M. Saito, H. Yoshida, *J. Power Sources* **326** (2016) 331–340. https://doi.org/10.1016/j.jpowsour.2016.06.110

[61] T. Andersen, K. V. Hansen, M. Mogensen, I. Chorkendorff, *Solid State Ion.* **190** (2011) 60–66. https://doi.org/10.1016/j.ssi.2011.02.024

[62] R. Knibbe, M. L. Traulsen, A. Hauch, S. D. Ebbesen, M. Mogensen, *J. Electrochem. Soc.* **157** (2010) B1209. https://doi.org/10.1149/1.3447752

[63] B. Königshofer, P. Boškoski, G. Nusev, M. Koroschetz, M. Hochfellner, M. Schwaiger, Đ. Juričić, C. Hochenauer, V. Subotić, *Applied Energy* **283** (2021) 116372. https://doi.org/10.1016/j.apenergy.2020.116372

[64] M. Vogler, A. Bieberle-Hütter, L. J. Gauckler, J. Warnatz, W. G. Bessler, *J. Electrochem. Soc.* **156** (2009) B663. https://doi.org/10.1149/1.3095477

[65] A. Bieberle, L. P. Meier, L. J. Gauckler, *J. Electrochem. Soc.* **148** (2001) A646. https://doi.org/10.1149/1.1372219

[66] S. Koomson, C.-G. Lee, *J. Electroanal. Chem.* **882** (2021) 115020. https://doi.org/10.1016/j.jelechem.2021.115020

[67] A. Nechache, A. Mansuy, M. Petitjean, J. Mougin, F. Mauvy, B. A. Boukamp, M. Cassira, A. Ringuedé, *Electrochim. Acta* **210** (2016) 596–605. http://doi.org/10.1016/j.electacta.2016.05.014

[68] Y. Yan, Q. Fang, L. Blum, W. Lehnert, *Electrochim. Acta* **258** (2017) 1254–1261. https://doi.org/10.1016/j.electacta.2017.11.180

[69] E. Köck, M. Kogler, B. Klötzer, M. F. Noisternig, S. Penner, *ACS Appl. Mater. Interfaces* **8** (2016) 16428–16443. https://doi.org/10.1021/acsami.6b03566

[70] S. D. Kim, D. W. Seo, A. K. Dorai, S. K. Woo, *Int. J. Hydrogen Energy* **38** (2013) 6569–6576. https://doi.org/10.1016/j.ijhydene.2013.03.115

[71] F. Guo, P. Xiao, *J. Eur. Cer. Soc.* **32**, (2012) 4157. https://doi.org/10.1016/j.jeurceramsoc.2012.07.035

[72] T. Onda, H. Yamauchi, M. Hayakawa, *Material Science Forum*, **449–452** (2004) 265–268. https://doi.org/10.4028/www.scientific.net/MSF.449-452.265

[73] F. Monaco, E. Effori, M. Hubert, E. Siebert, G. Geneste, B. Morel, E. Djurado, D. Montinaro, J. Laurencin, *Electrochim. Acta* **389** (2021) 138765. https://doi.org/10.1016/j.electacta.2021.138765

[74] A. Tsoga, A. Naoumidis, A. Gupta, D. Stöver, 1999, *Materials Science Forum* **308–311** (1999) 794–799. https://doi.org/10.4028/www.scientific.net/MSF.308-311.794

[75] C. H. Lee, G. M. Choi, *Solid State Ion.* **135** (2000) 653. https://doi.org/10.1016/S0167-2738(00)00427-6

[76] G. C. T. Silva, E. N. S. Muccillo, *Solid State Ion.* **180** (2009) 835. https://doi.org/10.1016/j.ssi.2009.02.003

9. SUMMARY IN ESTONIAN

Elektrolüüsirežiimis töötavate struktuurselt ja keemiliselt modifitseeritud tahkeoksiidelementide elektrokeemiline karakteriseerimine

Selle töö eesmärk oli uurida tipptasemel tahkeoksiidelemendi materjalide degradatsioonimehhanisme pärast pikaajalist tööd nii kütuselemendi kui ka elektrolüüsi režiimis ning parendada tahkeoksiidse elemendi elektrolüüsitöö efektiivsust läbi väikeste materiaalsete muudatuste. Võrreldavate tulemuste saavutamiseks, mis oleksid huvitavad ka tööstuslikus rakenduses, kasutati tipptasemel kaubanduslikke tahkeoksiidelementide komponente. Tahkeoksiidelementide pikaajalist stabiilsust testiti 50×50 mm elementidel terasest voolukollektorite vahel, mis lubas karakteriseerida tahkeoksiidelemendi struktuurimuutusi virnaga sarnases keskkonnas. Detailne elektrokeemiline karakteriseerimine teostati väikestel 20 mm läbimõõduga nööprakkudel, mis olid täielikult toodetud tööstuslikes tingimustes. Need nööprakkude uuringud keskendusid tahkeoksiidelemendi omadustele elektrolüüsi režiimis ja vesinikelektroodi aktiivkihi rollile tahkeoksiidelemendi süsteemis. Vesinikelektroodide tootmise käigus tehti vesinikelektroodi aktiivkihi mikrostruktuuris ja keemilises koostises väikeseid muudatusi, et karakteriseerida nende muutuste mõju tahkeoksiidelemendi elektrolüüsi efektiivsusele.

Käesoleva töö esimeses osas kirjeldatakse, kuidas pikaajalistes elektrokeemilistes testides karakteriseeriti kaubanduslike poolelementide ja laboris väljatöötatud hapnikelektroodidega tahkeoksiidelemente. Üks element töötas 17820 tundi kütuseelemendi režiimis temperatuuril 650 °C, teine töötas 860 tundi elektrolüüsi režiimis temperatuuril 800 °C. Kütuseelemendi katseandmed viitasid degradatsiooni kulgemise muutusele 9000 tundi pärast algust, kusjuures degradatsioonikiirus oli esimesel ajavahemikul 2,4%/1000 h ja teisel ajavahemikul 1,1%/1000 h. Elektrolüüsikatse degradatsioonikiirus oli umbes 16,3%/1000 h, kuid see taastus mõningal määral pärast igat impedantsi mõõtmist, kus elektrolüüsitöö peatati.

Seejärel karakteriseeriti degradeerunud rakke ToF-SIMS meetodi abil, et tuvastada ^{18}O kontsentratsiooni hapnikelektroodis, mis tutvustati ajalise stabiilsuskatse lõpus. ToF-SIMS andmeid kasutati aktiivsuskaardi loomiseks ja selle korreleerimiseks Ni osakeste kasvuga aja jooksul. ToF-SIMS meetodit kasutati ka Cr tuvastamiseks hapnikelektroodis ja Si tuvastamiseks vesinikelektroodis. Cr kontsentratsioonikaardid ei korreleerunud aktiivsuskaartidega ja Si kontsentratsioonikaardid viitasid sellele, et tihenduseks kasutatud klaas võis olla võimalik vesinikelektroodi mürgituse allikas. Si sadestumine vesinikelektroodi aktiivtsentritele võis olla suur osa tahkeoksiidelemendi degradatsioonist mõlemas töörežiimis.

Skanneeriva elektronmikroskoobi karakteriseerimistulemused pikaajalise katse läbinud elektrolüüsirakkudest näitasid GDC ja YSZ kihtide vahel märkimisväärseid pragusid. Need praod tekkisid tõenäoliselt oksiidioonide oksüdeerumise tagajärjel GDC ja YSZ piirpinna lähedal, tekitades YSZ terade vahel gaasilist hapnikku, mis võis lükata eelmainitud kihid lahku. See mehhanism oli tõenäoliselt peamine põhjus, miks tahkeoksiidelement degradeerus elektrolüüsirežiimis palju kiiremini kui kütuseelemendi režiimis.

Käesoleva töö teises osas modifitseeriti tipptasemel kaubanduslikku tahkeoksiidelemendi vesinkielektroodi aktiivkihi struktuuri, et uurida selle mõju elemendi elektrokeemilisele efektiivsusele elektrolüüsi režiimis. Tahkeoksiidelemente valmistati erineva paksusega vesinikelektroodi aktiivkihtidega ja saadud rakke karakteriseeriti elektronmikroskoobi ja elektrokeemiliste meetodite abil. Eksperimentaalsete elementide jõudlust võrreldi erinevatel temperatuuridel ja toitegaasi koostistel, kasutades tsüklilise voltammeetria meetodit. Eksperimentaalsete rakkude impedantsspektreid mõõdeti erinevatel toitegaasi (auru) kontsentratsioonitasemetel, kasutades ekvivalentseid vooluringi mudeleid ja sobitades arvutatud andmeid kompleks mittelineaarse vähimruutude analüüsi meetodi abil.

Impedantsanalüüs näitas, et vesinikelektroodi aktiivkihi paksuse suurendamisega tulenevad muutused tahkeoksiidelemendi impedantsspektri karakteersetes sagedustes olid suurimad piirkondades 1 kuni 10 Hz ja 1 kuni 10 kHz, st kahes erinevas vahelduvvoolu sageduspiirkonnas.

Käesolevas töös kogutud tulemused viisid järeldustele, et: i) vesinikelektroodi aktiivkihi lisamine tahkeoksiid elektrolüüsielemendi struktuuri suurendas oluliselt elektrolüüsi efektiivsust ja ii) tahkeoksiid elektrolüüsielemendi optimaalse vesinikelektroodi aktiivkihi paksuse dikteerisid elektrolüüsirežiimis rakendatud töötingimused.

Elektrolüüsirežiimis 700 °C juures töötamiseks tundus 16 μm paksusega vesinikelektroodi aktiivkihiga tahkeoksiidelement olevat optimaalne pikema kolmefaasi piirpinna pikkuse tõttu, samas 12 μm paksuse vesinikelektroodi aktiivkihiga element oli paremate difusiooniomaduste tõttu sellele lähedase efektiivsusega. Kõrgematel temperatuuridel muutusid aga madalsageduslikud impedantsprotsessid suure voolutiheduse juures reaktsioonikiirust piiravaks ja seetõttu osutus optimaalseks 7 μm paksuse vesinikelektroodi aktiivkihiga tahkeoksiidelement. Kõrgeim voolutihedus, -3,57 A/cm^2 -1,4 V pinge juures temperatuuril 800 °C, saavutati 7 μm paksuse vesinikelektroodi aktiivkihiga elemendi puhul. Väga paljutõotav lähenemisviis optimaalse vesinikelektroodi aktiivkihi paksusega elementide elektrolüüsi efektiivsuse parendamiseks näib olevat vee adsorptsiooniprotsessiga seotud voolupiirangute vähendamine aktiivkihis.

Käesoleva töö kolmandas osas toodeti koostöös tööstuspartneriga Fe, Co ja GDC-ga modifitseeritud vesinikelektroodi aktiivkihtidega tahkeoksiidelemendid ning neid karakteriseeriti detailselt. Neid rakke karakteriseeriti skanneeriva elektronmikroskoobiga ja elektrokeemiliste analüüsimeetodite, näiteks tsüklilise voltamperomeetria ja elektrokeemilise impedantsspektroskoopia abil. Võrreldes võrdlusrakuga näitasid modifitseeritud tahkeoksiidelemendid olulisi erinevusi elektrolüüsi efektiivsuses ja efektiivsuse sõltuvustes temperatuurist ja auru kontsentratsioonist toitegaasis.

Vesinikelektroodi aktiivkihi keemilised modifikatsioonid põhjustasid peamiselt muudatusi laenguülekande aktiivsuses ja reagentide transpordiprotsessides.

Mikrostruktuurilistest erinevustest tingitud gaasi difusiooniomaduste muutused olid olulised ainult kõrge voolutiheduse juures. Võrreldes võrdlusrakuga inhibeeriti GDC lisamisega madalal temperatuuril nii reagendi transpordi kui ka laenguülekande protsesse, samas kui laenguülekande protsessid olid aktiivsemad kõrgel temperatuuril. Co lisamine inhibeeris laenguülekande protsesse oluliselt, kuigi madalal temperatuuril reagendi transport paranes. Vesinikelektroodi aktiivkihi modifitseerimine Fe-ga parendas reagendi transpordiprotsesse temperatuuril 700 °C, samas kui 800 °C juures paranes oluliselt ka laenguülekande protsesside kiirus. Üldiselt saavutati parim elektrolüüsi efektiivsus Fe-ga rikastatud tahkeoksiidelemendiga, saavutades voolutiheduse -3,7 A/cm^2, -1,4 V pinge juures, 800 °C töötemperatuuril ja 90% auru kontsentratsioonil.

10. ACKNOWLEDGEMENTS

First and foremost, I would like to express my sincere gratitude to Professor Gunnar Nurk and Professor Enn Lust for their guidance and support throughout my academic journey. I deeply appreciate the time they dedicated to discussions, their encouragement to design my own experiments and their patience throughout my writing process.

I am also grateful to my supervisors at Elcogen – Sergii Pylypko, Martin Skov Skjøth-Rasmussen, and Juhan Subbi – for their invaluable guidance during both my PhD studies and professional work. Their insights and expertise helped me understand the critical role of processing in determining the quality and performance of solid oxide cells.

My sincere thanks go to Dr. Ove Korjus for his support and guidance in testing and analysis, and to Laur Kristjan Salvan for his moral support. I am thankful to Rait Kanarbik for keeping the laboratory operational. I also appreciate Priit Möller for helping me with the ToF-SIMS analysis and Marian Külaviir for assisting me with HR-SEM operation. I am also grateful to Valdek Mikli from TalTech for his assistance in acquiring high-resolution SEM images of my test samples.

Finally, I am profoundly grateful to my dear wife Kaie for her support, patience, and encouragement throughout this work. I am equally thankful to my mother and father for their constant support, belief in me, and for always cheering me on throughout my academic career.

This work was supported by Estonian Research Council grants PRG551, PUT1581, IUT20-13 and TEM-TA81, by Estonian Ministry of Education and Research (TK210), by the project “Increasing the knowledge intensity of Ida-Viru entrepreneurship” (ÕÜF2) co-founded by the European Union, by the EU through the European Regional Development Fund Project TK141 “Advanced materials and high-technology devices for energy recuperation systems”, by the European Union's Horizon 2020 research and innovation program under grant agreement No. 862482 (ARENHA project).

11. PUBLICATIONS

CURRICULUM VITAE

Name: Freddy Kukk
Date of birth: 18. November 1991
Citizenship: Estonia
Contact: Institute of Chemistry, University of Tartu, Ravila 14a, 50411, Tartu, Estonia
E-mail: freddy.kukk@outlook.com

Education:

2019–…	University of Tartu, Institute of Chemistry, Ph.D. student
2015–2017	Tallinn Technical University, School of Engineering, M.Sc.
2011–2014	University of Tartu, Institute of Chemistry, B.Sc.

Professional employment:

2019–…	Elcogen AS, Research and Development Engineer
2012–2015	University of Tartu, Institute of Chemistry, Chemist

Scientific Publications:

1. F. Kukk, P. Möller, R. Kanarbik, G. Nurk, Study of Long-Term Stability of Ni-Zr0.92Y0.08O2-δ|Zr0.92Y0.08O2-δ|Ce0.9Gd0.1O2-δ|Pr0.6Sr0.4CoO3-δ at SOFC and SOEC Mode, *Energies*, **14** (2021) 824.
2. F. Kukk, S. Pylypko, E. Lust, G. Nurk, Influence of Hydrogen Electrode Active Layer Thickness on Electrochemical Performance of Solid Oxide Cell Operating in Electrolysis Mode, *J. Electrochem. Soc.*, **170** (2023) 094501.
3. F. Kukk, S. Pylypko, M. S. Skjøth-Rasmussen, E. Lust, G. Nurk, Influence of Chemical Modifications with Fe, Co, and GDC on the Electrochemical Performance of the Ni-8YSZ Hydrogen Electrode in Solid Oxide Electrolysis Cells, *J. Electrochem. Soc.* **172** (2025) 110515.
4. F. Kukk, S. Pylypko, E. Lust, G. Nurk, Influence of Active Layer Thickness of Reversible Solid Oxide Cells on the Electrochemical Performance of Water Electrolysis, *ECS Trans.*, **103** (2021) 511−518.

ELULOOKIRJELDUS

Nimi: Freddy Kukk
Sünniaeg: 18. November 1991
Kodakondsus: Eesti
Kontakt: Tartu Ülikool, Keemia Instituut, Ravila 14a, 50411, Tartu, Eesti
E-post: freddy.kukk@outlook.com

Haridus:

2019–…	Tartu Ülikool, Keemia Instituut, doktoriõpe
2015–2017	Tallinna Tehnikaülikool, Inseneriteaduskond, M.Sc.
2011–2014	Tartu Ülikool, Keemia Instituut, B.Sc.

Töökogemus:

2019–…	Elcogen AS, Arendusinsener
2012–2015	Tartu Ülikool, Keemia Instituut, Keemik

Teaduspublikatsioonid:

1. F. Kukk, P. Möller, R. Kanarbik, G. Nurk, Study of Long-Term Stability of Ni-Zr0.92Y0.08O2-δ|Zr0.92Y0.08O2-δ|Ce0.9Gd0.1O2-δ|Pr0.6Sr0.4CoO3-δ at SOFC and SOEC Mode, *Energies*, **14** (2021) 824.
2. F. Kukk, S. Pylypko, E. Lust, G. Nurk, Influence of Hydrogen Electrode Active Layer Thickness on Electrochemical Performance of Solid Oxide Cell Operating in Electrolysis Mode, *J. Electrochem. Soc*., **170** (2023) 094501.
3. F. Kukk, S. Pylypko, M. S. Skjøth-Rasmussen, E. Lust, G. Nurk, Influence of Chemical Modifications with Fe, Co, and GDC on the Electrochemical Performance of the Ni-8YSZ Hydrogen Electrode in Solid Oxide Electrolysis Cells, *J. Electrochem. Soc*. **172** (2025) 110515.
4. F. Kukk, S. Pylypko, E. Lust, G. Nurk, Influence of Active Layer Thickness of Reversible Solid Oxide Cells on the Electrochemical Performance of Water Electrolysis, *ECS Trans.*, **103** (2021) 511−518.

DISSERTATIONES CHIMICAE UNIVERSITATIS TARTUENSIS

1. **Toomas Tamm.** Quantum-chemical simulation of solvent effects. Tartu, 1993, 110 p.
2. **Peeter Burk.** Theoretical study of gas-phase acid-base equilibria. Tartu, 1994, 96 p.
3. **Victor Lobanov.** Quantitative structure-property relationships in large descriptor spaces. Tartu, 1995, 135 p.
4. **Vahur Mäemets.** The ^{17}O and ^{1}H nuclear magnetic resonance study of H_2O in individual solvents and its charged clusters in aqueous solutions of electrolytes. Tartu, 1997, 140 p.
5. **Andrus Metsala.** Microcanonical rate constant in nonequilibrium distribution of vibrational energy and in restricted intramolecular vibrational energy redistribution on the basis of slater's theory of unimolecular reactions. Tartu, 1997, 150 p.
6. **Uko Maran.** Quantum-mechanical study of potential energy surfaces in different environments. Tartu, 1997, 137 p.
7. **Alar Jänes.** Adsorption of organic compounds on antimony, bismuth and cadmium electrodes. Tartu, 1998, 219 p.
8. **Kaido Tammeveski.** Oxygen electroreduction on thin platinum films and the electrochemical detection of superoxide anion. Tartu, 1998, 139 p.
9. **Ivo Leito.** Studies of Brønsted acid-base equilibria in water and non-aqueous media. Tartu, 1998, 101 p.
10. **Jaan Leis.** Conformational dynamics and equilibria in amides. Tartu, 1998, 131 p.
11. **Toonika Rinken.** The modelling of amperometric biosensors based on oxidoreductases. Tartu, 2000, 108 p.
12. **Dmitri Panov.** Partially solvated Grignard reagents. Tartu, 2000, 64 p.
13. **Kaja Orupõld.** Treatment and analysis of phenolic wastewater with microorganisms. Tartu, 2000, 123 p.
14. **Jüri Ivask.** Ion Chromatographic determination of major anions and cations in polar ice core. Tartu, 2000, 85 p.
15. **Lauri Vares.** Stereoselective Synthesis of Tetrahydrofuran and Tetrahydropyran Derivatives by Use of Asymmetric Horner-Wadsworth-Emmons and Ring Closure Reactions. Tartu, 2000, 184 p.
16. **Martin Lepiku.** Kinetic aspects of dopamine D_2 receptor interactions with specific ligands. Tartu, 2000, 81 p.
17. **Katrin Sak.** Some aspects of ligand specificity of P2Y receptors. Tartu, 2000, 106 p.
18. **Vello Pällin.** The role of solvation in the formation of iotsitch complexes. Tartu, 2001, 95 p.
19. **Katrin Kollist.** Interactions between polycyclic aromatic compounds and humic substances. Tartu, 2001, 93 p.

20. **Ivar Koppel.** Quantum chemical study of acidity of strong and superstrong Brønsted acids. Tartu, 2001, 104 p.
21. **Viljar Pihl.** The study of the substituent and solvent effects on the acidity of OH and CH acids. Tartu, 2001, 132 p.
22. **Natalia Palm.** Specification of the minimum, sufficient and significant set of descriptors for general description of solvent effects. Tartu, 2001, 134 p.
23. **Sulev Sild.** QSPR/QSAR approaches for complex molecular systems. Tartu, 2001, 134 p.
24. **Ruslan Petrukhin.** Industrial applications of the quantitative structure-property relationships. Tartu, 2001, 162 p.
25. **Boris V. Rogovoy.** Synthesis of (benzotriazolyl)carboximidamides and their application in relations with *N*- and *S*-nucleophyles. Tartu, 2002, 84 p.
26. **Koit Herodes.** Solvent effects on UV-vis absorption spectra of some solvatochromic substances in binary solvent mixtures: the preferential solvation model. Tartu, 2002, 102 p.
27. **Anti Perkson.** Synthesis and characterisation of nanostructured carbon. Tartu, 2002, 152 p.
28. **Ivari Kaljurand.** Self-consistent acidity scales of neutral and cationic Brønsted acids in acetonitrile and tetrahydrofuran. Tartu, 2003, 108 p.
29. **Karmen Lust.** Adsorption of anions on bismuth single crystal electrodes. Tartu, 2003, 128 p.
30. **Mare Piirsalu.** Substituent, temperature and solvent effects on the alkaline hydrolysis of substituted phenyl and alkyl esters of benzoic acid. Tartu, 2003, 156 p.
31. **Meeri Sassian.** Reactions of partially solvated Grignard reagents. Tartu, 2003, 78 p.
32. **Tarmo Tamm.** Quantum chemical modelling of polypyrrole. Tartu, 2003. 100 p.
33. **Erik Teinemaa.** The environmental fate of the particulate matter and organic pollutants from an oil shale power plant. Tartu, 2003. 102 p.
34. **Jaana Tammiku-Taul.** Quantum chemical study of the properties of Grignard reagents. Tartu, 2003. 120 p.
35. **Andre Lomaka.** Biomedical applications of predictive computational chemistry. Tartu, 2003. 132 p.
36. **Kostyantyn Kirichenko.** Benzotriazole – Mediated Carbon–Carbon Bond Formation. Tartu, 2003. 132 p.
37. **Gunnar Nurk.** Adsorption kinetics of some organic compounds on bismuth single crystal electrodes. Tartu, 2003, 170 p.
38. **Mati Arulepp.** Electrochemical characteristics of porous carbon materials and electrical double layer capacitors. Tartu, 2003, 196 p.
39. **Dan Cornel Fara.** QSPR modeling of complexation and distribution of organic compounds. Tartu, 2004, 126 p.
40. **Riina Mahlapuu.** Signalling of galanin and amyloid precursor protein through adenylate cyclase. Tartu, 2004, 124 p.

41. **Mihkel Kerikmäe.** Some luminescent materials for dosimetric applications and physical research. Tartu, 2004, 143 p.
42. **Jaanus Kruusma.** Determination of some important trace metal ions in human blood. Tartu, 2004, 115 p.
43. **Urmas Johanson.** Investigations of the electrochemical properties of polypyrrole modified electrodes. Tartu, 2004, 91 p.
44. **Kaido Sillar.** Computational study of the acid sites in zeolite ZSM-5. Tartu, 2004, 80 p.
45. **Aldo Oras.** Kinetic aspects of dATPαS interaction with $P2Y_1$ receptor. Tartu, 2004, 75 p.
46. **Erik Mölder.** Measurement of the oxygen mass transfer through the air-water interface. Tartu, 2005, 73 p.
47. **Thomas Thomberg.** The kinetics of electroreduction of peroxodisulfate anion on cadmium (0001) single crystal electrode. Tartu, 2005, 95 p.
48. **Olavi Loog.** Aspects of condensations of carbonyl compounds and their imine analogues. Tartu, 2005, 83 p.
49. **Siim Salmar.** Effect of ultrasound on ester hydrolysis in aqueous ethanol. Tartu, 2006, 73 p.
50. **Ain Uustare.** Modulation of signal transduction of heptahelical receptors by other receptors and G proteins. Tartu, 2006, 121 p.
51. **Sergei Yurchenko.** Determination of some carcinogenic contaminants in food. Tartu, 2006, 143 p.
52. **Kaido Tämm.** QSPR modeling of some properties of organic compounds. Tartu, 2006, 67 p.
53. **Olga Tšubrik.** New methods in the synthesis of multisubstituted hydrazines. Tartu. 2006, 183 p.
54. **Lilli Sooväli.** Spectrophotometric measurements and their uncertainty in chemical analysis and dissociation constant measurements. Tartu, 2006, 125 p.
55. **Eve Koort.** Uncertainty estimation of potentiometrically measured ph and pK_a values. Tartu, 2006, 139 p.
56. **Sergei Kopanchuk.** Regulation of ligand binding to melanocortin receptor subtypes. Tartu, 2006, 119 p.
57. **Silvar Kallip.** Surface structure of some bismuth and antimony single crystal electrodes. Tartu, 2006, 107 p.
58. **Kristjan Saal.** Surface silanization and its application in biomolecule coupling. Tartu, 2006, 77 p.
59. **Tanel Tätte.** High viscosity $Sn(OBu)_4$ oligomeric concentrates and their applications in technology. Tartu, 2006, 91 p.
60. **Dimitar Atanasov Dobchev**. Robust QSAR methods for the prediction of properties from molecular structure. Tartu, 2006, 118 p.
61. **Hannes Hagu**. Impact of ultrasound on hydrophobic interactions in solutions. Tartu, 2007, 81 p.
62. **Rutha Jäger.** Electroreduction of peroxodisulfate anion on bismuth electrodes. Tartu, 2007, 142 p.

63. **Kaido Viht.** Immobilizable bisubstrate-analogue inhibitors of basophilic protein kinases: development and application in biosensors. Tartu, 2007, 88 p.
64. **Eva-Ingrid Rõõm.** Acid-base equilibria in nonpolar media. Tartu, 2007, 156 p.
65. **Sven Tamp.** DFT study of the cesium cation containing complexes relevant to the cesium cation binding by the humic acids. Tartu, 2007, 102 p.
66. **Jaak Nerut.** Electroreduction of hexacyanoferrate(III) anion on Cadmium (0001) single crystal electrode. Tartu, 2007, 180 p.
67. **Lauri Jalukse.** Measurement uncertainty estimation in amperometric dissolved oxygen concentration measurement. Tartu, 2007, 112 p.
68. **Aime Lust.** Charge state of dopants and ordered clusters formation in CaF_2:Mn and CaF_2:Eu luminophors. Tartu, 2007, 100 p.
69. **Iiris Kahn**. Quantitative Structure-Activity Relationships of environmentally relevant properties. Tartu, 2007, 98 p.
70. **Mari Reinik.** Nitrates, nitrites, N-nitrosamines and polycyclic aromatic hydrocarbons in food: analytical methods, occurrence and dietary intake. Tartu, 2007, 172 p.
71. **Heili Kasuk.** Thermodynamic parameters and adsorption kinetics of organic compounds forming the compact adsorption layer at Bi single crystal electrodes. Tartu, 2007, 212 p.
72. **Erki Enkvist.** Synthesis of adenosine-peptide conjugates for biological applications. Tartu, 2007, 114 p.
73. **Svetoslav Hristov Slavov**. Biomedical applications of the QSAR approach. Tartu, 2007, 146 p.
74. **Eneli Härk.** Electroreduction of complex cations on electrochemically polished Bi(*hkl*) single crystal electrodes. Tartu, 2008, 158 p.
75. **Priit Möller.** Electrochemical characteristics of some cathodes for medium temperature solid oxide fuel cells, synthesized by solid state reaction technique. Tartu, 2008, 90 p.
76. **Signe Viggor.** Impact of biochemical parameters of genetically different pseudomonads at the degradation of phenolic compounds. Tartu, 2008, 122 p.
77. **Ave Sarapuu.** Electrochemical reduction of oxygen on quinone-modified carbon electrodes and on thin films of platinum and gold. Tartu, 2008, 134 p.
78. **Agnes Kütt.** Studies of acid-base equilibria in non-aqueous media. Tartu, 2008, 198 p.
79. **Rouvim Kadis.** Evaluation of measurement uncertainty in analytical chemistry: related concepts and some points of misinterpretation. Tartu, 2008, 118 p.
80. **Valter Reedo.** Elaboration of IVB group metal oxide structures and their possible applications. Tartu, 2008, 98 p.
81. **Aleksei Kuznetsov.** Allosteric effects in reactions catalyzed by the cAMP-dependent protein kinase catalytic subunit. Tartu, 2009, 133 p.

82. **Aleksei Bredihhin.** Use of mono- and polyanions in the synthesis of multisubstituted hydrazine derivatives. Tartu, 2009, 105 p.
83. **Anu Ploom.** Quantitative structure-reactivity analysis in organosilicon chemistry. Tartu, 2009, 99 p.
84. **Argo Vonk.** Determination of adenosine A_{2A}- and dopamine D_1 receptor-specific modulation of adenylate cyclase activity in rat striatum. Tartu, 2009, 129 p.
85. **Indrek Kivi.** Synthesis and electrochemical characterization of porous cathode materials for intermediate temperature solid oxide fuel cells. Tartu, 2009, 177 p.
86. **Jaanus Eskusson.** Synthesis and characterisation of diamond-like carbon thin films prepared by pulsed laser deposition method. Tartu, 2009, 117 p.
87. **Marko Lätt.** Carbide derived microporous carbon and electrical double layer capacitors. Tartu, 2009, 107 p.
88. **Vladimir Stepanov.** Slow conformational changes in dopamine transporter interaction with its ligands. Tartu, 2009, 103 p.
89. **Aleksander Trummal.** Computational Study of Structural and Solvent Effects on Acidities of Some Brønsted Acids. Tartu, 2009, 103 p.
90. **Eerold Vellemäe.** Applications of mischmetal in organic synthesis. Tartu, 2009, 93 p.
91. **Sven Parkel.** Ligand binding to 5-HT_{1A} receptors and its regulation by Mg^{2+} and Mn^{2+}. Tartu, 2010, 99 p.
92. **Signe Vahur.** Expanding the possibilities of ATR-FT-IR spectroscopy in determination of inorganic pigments. Tartu, 2010, 184 p.
93. **Tavo Romann**. Preparation and surface modification of bismuth thin film, porous, and microelectrodes. Tartu, 2010, 155 p.
94. **Nadežda Aleksejeva.** Electrocatalytic reduction of oxygen on carbon nanotube-based nanocomposite materials. Tartu, 2010, 147 p.
95. **Marko Kullapere.** Electrochemical properties of glassy carbon, nickel and gold electrodes modified with aryl groups. Tartu, 2010, 233 p.
96. **Liis Siinor.** Adsorption kinetics of ions at Bi single crystal planes from aqueous electrolyte solutions and room-temperature ionic liquids. Tartu, 2010, 101 p.
97. **Angela Vaasa.** Development of fluorescence-based kinetic and binding assays for characterization of protein kinases and their inhibitors. Tartu 2010, 101 p.
98. **Indrek Tulp.** Multivariate analysis of chemical and biological properties. Tartu 2010, 105 p.
99. **Aare Selberg.** Evaluation of environmental quality in Northern Estonia by the analysis of leachate. Tartu 2010, 117 p.
100. **Darja Lavõgina.** Development of protein kinase inhibitors based on adenosine analogue-oligoarginine conjugates. Tartu 2010, 248 p.
101. **Laura Herm.** Biochemistry of dopamine D_2 receptors and its association with motivated behaviour. Tartu 2010, 156 p.

102. **Terje Raudsepp.** Influence of dopant anions on the electrochemical properties of polypyrrole films. Tartu 2010, 112 p.
103. **Margus Marandi.** Electroformation of Polypyrrole Films: *In-situ* AFM and STM Study. Tartu 2011, 116 p.
104. **Kairi Kivirand.** Diamine oxidase-based biosensors: construction and working principles. Tartu, 2011, 140 p.
105. **Anneli Kruve.** Matrix effects in liquid-chromatography electrospray mass-spectrometry. Tartu, 2011, 156 p.
106. **Gary Urb.** Assessment of environmental impact of oil shale fly ash from PF and CFB combustion. Tartu, 2011, 108 p.
107. **Nikita Oskolkov.** A novel strategy for peptide-mediated cellular delivery and induction of endosomal escape. Tartu, 2011, 106 p.
108. **Dana Martin.** The QSPR/QSAR approach for the prediction of properties of fullerene derivatives. Tartu, 2011, 98 p.
109. **Säde Viirlaid.** Novel glutathione analogues and their antioxidant activity. Tartu, 2011, 106 p.
110. **Ülis Sõukand.** Simultaneous adsorption of Cd^{2+}, Ni^{2+}, and Pb^{2+} on peat. Tartu, 2011, 124 p.
111. **Lauri Lipping.** The acidity of strong and superstrong Brønsted acids, an outreach for the “limits of growth”: a quantum chemical study. Tartu, 2011, 124 p.
112. **Heisi Kurig.** Electrical double-layer capacitors based on ionic liquids as electrolytes. Tartu, 2011, 146 p.
113. **Marje Kasari.** Bisubstrate luminescent probes, optical sensors and affinity adsorbents for measurement of active protein kinases in biological samples. Tartu, 2012, 126 p.
114. **Kalev Takkis.** Virtual screening of chemical databases for bioactive molecules. Tartu, 2012, 122 p.
115. **Ksenija Kisseljova**. Synthesis of aza-β^3-amino acid containing peptides and kinetic study of their phosphorylation by protein kinase A. Tartu, 2012, 104 p.
116. **Riin Rebane.** Advanced method development strategy for derivatization LC/ESI/MS. Tartu, 2012, 184 p.
117. **Vladislav Ivaništšev.** Double layer structure and adsorption kinetics of ions at metal electrodes in room temperature ionic liquids. Tartu, 2012, 128 p.
118. **Irja Helm.** High accuracy gravimetric Winkler method for determination of dissolved oxygen. Tartu, 2012, 139 p.
119. **Karin Kipper.** Fluoroalcohols as Components of LC-ESI-MS Eluents: Usage and Applications. Tartu, 2012, 164 p.
120. **Arno Ratas.** Energy storage and transfer in dosimetric luminescent materials. Tartu, 2012, 163 p.
121. **Reet Reinart-Okugbeni**. Assay systems for characterisation of subtype-selective binding and functional activity of ligands on dopamine receptors. Tartu, 2012, 159 p.

122. **Lauri Sikk.** Computational study of the Sonogashira cross-coupling reaction. Tartu, 2012, 81 p.
123. **Karita Raudkivi.** Neurochemical studies on inter-individual differences in affect-related behaviour of the laboratory rat. Tartu, 2012, 161 p.
124. **Indrek Saar.** Design of GalR2 subtype specific ligands: their role in depression-like behavior and feeding regulation. Tartu, 2013, 126 p.
125. **Ann Laheäär.** Electrochemical characterization of alkali metal salt based non-aqueous electrolytes for supercapacitors. Tartu, 2013, 127 p.
126. **Kerli Tõnurist.** Influence of electrospun separator materials properties on electrochemical performance of electrical double-layer capacitors. Tartu, 2013, 147 p.
127. **Kaija Põhako-Esko.** Novel organic and inorganic ionogels: preparation and characterization. Tartu, 2013, 124 p.
128. **Ivar Kruusenberg.** Electroreduction of oxygen on carbon nanomaterial-based catalysts. Tartu, 2013, 191 p.
129. **Sander Piiskop.** Kinetic effects of ultrasound in aqueous acetonitrile solutions. Tartu, 2013, 95 p.
130. **Ilona Faustova**. Regulatory role of L-type pyruvate kinase N-terminal domain. Tartu, 2013, 109 p.
131. **Kadi Tamm.** Synthesis and characterization of the micro-mesoporous anode materials and testing of the medium temperature solid oxide fuel cell single cells. Tartu, 2013, 138 p.
132. **Iva Bozhidarova Stoyanova-Slavova.** Validation of QSAR/QSPR for regulatory purposes. Tartu, 2013, 109 p.
133. **Vitali Grozovski**. Adsorption of organic molecules at single crystal electrodes studied by *in situ* STM method. Tartu, 2014, 146 p.
134. **Santa Veikšina**. Development of assay systems for characterisation of ligand binding properties to melanocortin 4 receptors. Tartu, 2014, 151 p.
135. **Jüri Liiv.** PVDF (polyvinylidene difluoride) as material for active element of twisting-ball displays. Tartu, 2014, 111 p.
136. **Kersti Vaarmets.** Electrochemical and physical characterization of pristine and activated molybdenum carbide-derived carbon electrodes for the oxygen electroreduction reaction. Tartu, 2014, 131 p.
137. **Lauri Tõntson**. Regulation of G-protein subtypes by receptors, guanine nucleotides and Mn^{2+}. Tartu, 2014, 105 p.
138. **Aiko Adamson.** Properties of amine-boranes and phosphorus analogues in the gas phase. Tartu, 2014, 78 p.
139. **Elo Kibena**. Electrochemical grafting of glassy carbon, gold, highly oriented pyrolytic graphite and chemical vapour deposition-grown graphene electrodes by diazonium reduction method. Tartu, 2014, 184 p.
140. **Teemu Näykki.** Novel Tools for Water Quality Monitoring – From Field to Laboratory. Tartu, 2014, 202 p.
141. **Karl Kaupmees.** Acidity and basicity in non-aqueous media: importance of solvent properties and purity. Tartu, 2014, 128 p.

142. **Oleg Lebedev**. Hydrazine polyanions: different strategies in the synthesis of heterocycles. Tartu, 2015, 118 p.
143. **Geven Piir.** Environmental risk assessment of chemicals using QSAR methods. Tartu, 2015, 123 p.
144. **Olga Mazina.** Development and application of the biosensor assay for measurements of cyclic adenosine monophosphate in studies of G protein-coupled receptor signalinga. Tartu, 2015, 116 p.
145. **Sandip Ashokrao Kadam.** Anion receptors: synthesis and accurate binding measurements. Tartu, 2015, 116 p.
146. **Indrek Tallo.** Synthesis and characterization of new micro-mesoporous carbide derived carbon materials for high energy and power density electrical double layer capacitors. Tartu, 2015, 148 p.
147. **Heiki Erikson.** Electrochemical reduction of oxygen on nanostructured palladium and gold catalysts. Tartu, 2015, 204 p.
148. **Erik Anderson.** *In situ* Scanning Tunnelling Microscopy studies of the interfacial structure between Bi(111) electrode and a room temperature ionic liquid. Tartu, 2015, 118 p.
149. **Girinath G. Pillai.** Computational Modelling of Diverse Chemical, Biochemical and Biomedical Properties. Tartu, 2015, 140 p.
150. **Piret Pikma.** Interfacial structure and adsorption of organic compounds at Cd(0001) and Sb(111) electrodes from ionic liquid and aqueous electrolytes: an *in situ* STM study. Tartu, 2015, 126 p.
151. **Ganesh babu Manoharan.** Combining chemical and genetic approaches for photoluminescence assays of protein kinases. Tartu, 2016, 126 p.
152. **Carolin Siimenson**. Electrochemical characterization of halide ion adsorption from liquid mixtures at Bi(111) and pyrolytic graphite electrode surface. Tartu, 2016, 110 p.
153. **Asko Laaniste.** Comparison and optimisation of novel mass spectrometry ionisation sources. Tartu, 2016, 156 p.
154. **Hanno Evard.** Estimating limit of detection for mass spectrometric analysis methods. Tartu, 2016, 224 p.
155. **Kadri Ligi.** Characterization and application of protein kinase-responsive organic probes with triplet-singlet energy transfer. Tartu, 2016, 122 p.
156. **Margarita Kagan.** Biosensing penicillins' residues in milk flows. Tartu, 2016, 130 p.
157. **Marie Kriisa.** Development of protein kinase-responsive photoluminescent probes and cellular regulators of protein phosphorylation. Tartu, 2016, 106 p.
158. **Mihkel Vestli.** Ultrasonic spray pyrolysis deposited electrolyte layers for intermediate temperature solid oxide fuel cells. Tartu, 2016, 156 p.
159. **Silver Sepp**. Influence of porosity of the carbide-derived carbon on the properties of the composite electrocatalysts and characteristics of polymer electrolyte fuel cells. Tartu, 2016, 137 p.
160. **Kristjan Haav**. Quantitative relative equilibrium constant measurements in supramolecular chemistry. Tartu, 2017, 158 p.

161. **Anu Teearu**. Development of MALDI-FT-ICR-MS methodology for the analysis of resinous materials. Tartu, 2017, 205 p.
162. **Taavi Ivan**. Bifunctional inhibitors and photoluminescent probes for studies on protein complexes. Tartu, 2017, 140 p.
163. **Maarja-Liisa Oldekop**. Characterization of amino acid derivatization reagents for LC-MS analysis. Tartu, 2017, 147 p.
164. **Kristel Jukk**. Electrochemical reduction of oxygen on platinum- and palladium-based nanocatalysts. Tartu, 2017, 250 p.
165. **Siim Kukk**. Kinetic aspects of interaction between dopamine transporter and *N*-substituted nortropane derivatives. Tartu, 2017, 107 p.
166. **Birgit Viira**. Design and modelling in early drug development in targeting HIV-1 reverse transcriptase and Malaria. Tartu, 2017, 172 p.
167. **Rait Kivi**. Allostery in cAMP dependent protein kinase catalytic subunit. Tartu, 2017, 115 p.
168. **Agnes Heering**. Experimental realization and applications of the unified acidity scale. Tartu, 2017, 123 p.
169. **Delia Juronen**. Biosensing system for the rapid multiplex detection of mastitis-causing pathogens in milk. Tartu, 2018, 85 p.
170. **Hedi Rahnel.** ARC-inhibitors: from reliable biochemical assays to regulators of physiology of cells. Tartu, 2018, 176 p.
171. **Anton Ruzanov.** Computational investigation of the electrical double layer at metal–aqueous solution and metal–ionic liquid interfaces. Tartu, 2018, 129 p.
172. **Katrin Kestav.** Crystal Structure-Guided Development of Bisubstrate-Analogue Inhibitors of Mitotic Protein Kinase Haspin. Tartu, 2018, 166 p.
173. **Mihkel Ilisson.** Synthesis of novel heterocyclic hydrazine derivatives and their conjugates. Tartu, 2018, 101 p.
174. **Anni Allikalt.** Development of assay systems for studying ligand binding to dopamine receptors. Tartu, 2018, 160 p.
175. **Ove Oll.** Electrical double layer structure and energy storage characteristics of ionic liquid based capacitors. Tartu, 2018, 187 p.
176. **Rasmus Palm.** Carbon materials for energy storage applications. Tartu, 2018, 114 p.
177. **Jörgen Metsik.** Preparation and stability of poly(3,4-ethylenedioxythiophene) thin films for transparent electrode applications. Tartu, 2018, 111 p.
178. **Sofja Tšepelevitš.** Experimental studies and modeling of solute-solvent interactions. Tartu, 2018, 109 p.
179. **Märt Lõkov.** Basicity of some nitrogen, phosphorus and carbon bases in acetonitrile. Tartu, 2018, 104 p.
180. **Anton Mastitski**. Preparation of α-aza-amino acid precursors and related compounds by novel methods of reductive one-pot alkylation and direct alkylation. Tartu, 2018, 155 p.
181. **Jürgen Vahter**. Development of bisubstrate inhibitors for protein kinase CK2. Tartu, 2019, 186 p.

182. **Piia Liigand.** Expanding and improving methodology and applications of ionization efficiency measurements. Tartu, 2019, 189 p.
183. **Sigrid Selberg.** Synthesis and properties of lipophilic phosphazene-based indicator molecules. Tartu, 2019, 74 p.
184. **Jaanus Liigand.** Standard substance free quantification for LC/ESI/MS analysis based on the predicted ionization efficiencies. Tartu, 2019, 254 p.
185. **Marek Mooste.** Surface and electrochemical characterisation of aryl film and nanocomposite material modified carbon and metal-based electrodes. Tartu, 2019, 304 p.
186. **Mare Oja.** Experimental investigation and modelling of pH profiles for effective membrane permeability of drug substances. Tartu, 2019, 306 p.
187. **Sajid Hussain.** Electrochemical reduction of oxygen on supported Pt catalysts. Tartu, 2019, 220 p.
188. **Ronald Väli.** Glucose-derived hard carbon electrode materials for sodium-ion batteries. Tartu, 2019, 180 p.
189. **Ester Tee.** Analysis and development of selective synthesis methods of hierarchical micro- and mesoporous carbons. Tartu, 2019, 210 p.
190. **Martin Maide.** Influence of the microstructure and chemical composition of the fuel electrode on the electrochemical performance of reversible solid oxide fuel cell. Tartu, 2020, 144 p.
191. **Edith Viirlaid.** Biosensing Pesticides in Water Samples. Tartu, 2020, 102 p.
192. **Maike Käärik.** Nanoporous carbon: the controlled nanostructure, and structure-property relationships. Tartu, 2020, 162 p.
193. **Artur Gornischeff.** Study of ionization efficiencies for derivatized compounds in LC/ESI/MS and their application for targeted analysis. Tartu, 2020, 124 p.
194. **Reet Link.** Ligand binding, allosteric modulation and constitutive activity of melanocortin-4 receptors. Tartu, 2020, 108 p.
195. **Pilleriin Peets.** Development of instrumental methods for the analysis of textile fibres and dyes. Tartu, 2020, 150 p.
196. **Larisa Ivanova.** Design of active compounds against neurodegenerative diseases. Tartu, 2020, 152 p.
197. **Meelis Härmas.** Impact of activated carbon microstructure and porosity on electrochemical performance of electrical double-layer capacitors. Tartu, 2020, 122 p.
198. **Ruta Hecht.** Novel Eluent Additives for LC-MS Based Bioanalytical Methods. Tartu, 2020, 202 p.
199. **Max Hecht.** Advances in the Development of a Point-of-Care Mass Spectrometer Test. Tartu, 2020, 168 p.
200. **Ida Rahu.** Bromine formation in inorganic bromide/nitrate mixtures and its application for oxidative aromatic bromination. Tartu, 2020, 116 p.
201. **Sander Ratso**. Electrocatalysis of oxygen reduction on non-precious metal catalysts. Tartu, 2020, 371 p.
202. **Astrid Darnell.** Computational design of anion receptors and evaluation of host-guest binding. Tartu, 2021, 150 p.

203. **Ove Korjus.** The development of ceramic fuel electrode for solid oxide cells. Tartu, 2021, 150 p.
204. **Merit Oss.** Ionization efficiency in electrospray ionization source and its relations to compounds' physico-chemical properties. Tartu, 2021, 124 p.
205. **Madis Lüsi**. Electroreduction of oxygen on nanostructured palladium catalysts. Tartu, 2021, 180 p.
206. **Eliise Tammekivi.** Derivatization and quantitative gas-chromatographic analysis of oils. Tartu, 2021, 122 p.
207. **Simona Selberg.** Development of Small-Molecule Regulators of Epitranscriptomic Processes. Tartu, 2021, 122 p.
208. **Olivier Etebe Nonga.** Inhibitors and photoluminescent probes for in vitro studies on protein kinases PKA and PIM. Tartu, 2021, 189 p.
209. **Riinu Härmas.** The structure and H2 diffusion in porous carbide-derived carbon particles. Tartu, 2022, 123 p.
210. **Maarja Paalo.** Synthesis and characterization of novel carbon electrodes for high power density electrochemical capacitors. Tartu, 2022, 144 p.
211. **Jinfeng Zhao.** Electrochemical characteristics of Bi(hkl) and micro-mesoporous carbon electrodes in ionic liquid based electrolytes. Tartu, 2022, 134 p.
212. **Alar Heinsaar.** Investigation of oxygen electrode materials for high-temperature solid oxide cells in natural conditions. Tartu, 2022, 120 p.
213. **Jaana Lilloja.** Transition metal and nitrogen doped nanocarbon cathode catalysts for anion exchange membrane fuel cells. Tartu, 2022, 202 p.
214. **Maris-Johanna Tahk.** Novel fluorescence-based methods for illuminating transmembrane signal transduction by G-protein coupled receptors. Tartu, 2022, 200 p.
215. **Eerik Jõgi.** Development and Applications of E. coli Immunosensor. Tartu, 2022, 103 p.
216. **Alo Rüütel.** Design principles of synthetic molecular receptors for anion-selective electrodes. Tartu, 2022, 109 p.
217. **Tanel Sõrmus.** Development of stimuli-responsive and covalent bisubstrate inhibitors of protein kinases. Tartu, 2022, 148 p.
218. **Oleg Artemchuk.** Autotrophic nitrogen removal processes for nutrient removal from sidestream and mainstream wastewater. Tartu, 2022, 115 p.
219. **Andre Leesment.** Quantitative studies of Brønsted acidity in biphasic systems and gas-phase. Tartu, 2023, 83 p.
220. **Meeli Arujõe-Sado.** Structural effects in aza-peptide bond formation reaction. Tartu, 2023, 83 p.
221. **Jonas Mart Linge.** Electrochemical reduction of oxygen on silver-based catalysts. Tartu, 2023, 269 p.
222. **Tõnis Laasfeld.** Integrating Image Analysis and Quantitative Modeling for a Holistic View of GPCR Ligand Binding Dynamics. Tartu, 2023, 226 p.
223. **Ernesto de Jesus Zapata Flores.** Derivatization Reagents used in negative mode electrospray LC-MS. Tartu, 2023, 107 p.

224. **Patrick Teppor.** Obtaining platinum-free oxygen reduction catalysts through biomass valorization: a case study of peat. Tartu, 2023, 161 p.
225. **Peeter Valk.** Methanol Oxidation on Platinum-Rare-Earth Metal Oxide Activated Catalysts. Tartu, 2023, 162 p.
226. **Shidong Chen.** Unravelling prehistoric plant exploitation in eastern Baltic: organic residue analysis of plant-based materials by multi-method approach. Tartu, 2023, 245 p.
227. **Yogesh Kumar.** M-N_4 macrocycle-based catalysts for electrocatalysis of oxygen reduction and oxygen evolution. Tartu, 2023, 224 p.
228. **Kerli Martin.** Recognition of carboxylates by synthetic receptors – from structure-affinity studies to solid-contact anion-selective electrode prototyping. Tartu, 2024, 130 p.
229. **Huy Quí Vinh Nguyen.** Development of Carbon Supported Pt–CeO_2 Catalysts for Proton Exchange Membrane Fuel Cells. Tartu, 2024, 198 p.
230. **Heigo Ers**. Adsorption and Structuring Processes at Single Crystal Electrode – Ionic Liquid Interface – Insights from Simulations and *in situ* Studies. Tartu, 2024, 137 p.
231. **Ritums Cepitis.** Modelling Structural and Geometrical Effects in Carbon Dioxide and Oxygen Electrocatalysis. Tartu, 2024, 99 p.
232. **Kaarel Kisand.** Resorcinol-derived carbon-based catalysts for polymer electrolyte fuel cell cathodes. Tartu, 2024, 205 p.
233. **Akmal Kosimov**. Template-assisted Mechanosynthesis (TAMS) for the production of bifunctional transition metal-based catalysts. Tartu, 2024, 123 p.
234. **Larissa Silva Macieli.** Derivatization-targeted LC-MS analysis of compounds containing amino group. Tartu, 2024, 157 p.
235. **Silvester Jürjo.** Separation of rare earth elements from Estonian phosphorite ore using liquid extraction followed by electrochemical reduction. Tartu, 2024, 99 p.
236. **Jan-Michael C. Cayme.** Organic-inorganic interactions in experimental and archaeological ceramics. Tartu, 2025, 156 p.
237. **Miriam Koppel.** The diffusion of H2 adsorbed in carbide-derived carbons: a quasi-elastic neutron scattering study. Tartu, 2025, 138 p.
238. **Kenneth Tuul.** Evaluating lithium-ion pouch cells and hydrogen storage materials under extreme conditions using advanced techniques. Tartu, 2025, 188 p.
239. **Marta-Lisette Pikma.** Exploring the basicity of phosphanes and related compounds. Tartu, 2025, 100 p.
240. **Indrek Saar.** Development of novel on-site chemical analysis tests – from alternative materials and technologies to functional prototypes. Tartu, 2025, 214 p.
241. **Gulnara Yusibova.** TAL MOF-Derived M-N-C Electrocatalysts for Oxygen Reduction and Evolution Reactions. Tartu, 2025, 120 p.
242. **Karl Marti Toots.** Cheminformatics Approaches for Analyzing and Modeling the Gas-Ionic Liquid Distribution of Organic Solutes. Tartu, 2025, 249 p.